Study of Oscillations and Flows in Solar Magnetic Active Regions

Hope Thackray

Dr Rekha Jain

The University Of Sheffield.

University of Sheffield

School of Mathematics and Statistics

A thesis submitted in partial fulfilment of the requirements for the degree of

Doctor of Philosophy

December 2019

To my cats, Peanut and Abe, who will never be able to read this.

Acknowledgements

It goes without saying that the first of my acknowledgements should be towards my supervisor, Dr Rekha Jain. Through her expertise and assistance, a difficult path was made much easier to traverse, and by taking me under her wing, she helped build the researcher and teacher buried within myself. I would also like to extend thanks towards Dr Kiran Jain and the NSO team in Boulder for the use of GONG data with Ring Diagram Analysis - it was indispensable!

For the past 11 (almost 12!) years of my life, I have been able to depend fully on my partner, Owen. Though I may have made mistakes, acted irrationally, and almost certainly contributed to a few of his grey hairs, he has never failed to stick by my side and prop me up when I felt at my weakest. I hope there comes a time when I can do the same for him — until then, this exists as proof of my sincere love and gratitude.

My ever-loving family were always there to hear about my latest adventures, and though I visited much less frequently than I would have liked, ensured I always knew where I could find home. Their support throughout the years is immeasurable, and for that I am forever indebted.

Without my dearest friends and colleagues, I know that this thesis would not have come to fruition. To Ellie, Jonny and Poppy, I offer thanks for many tears shed both in sadness and joy. Though your influences may have propagated some bad habits, I found myself uplifted by your encouragement and seemingly endless patience. Many an enlightening experience was shared with Callum and Matt, particularly in times when a de-stress was necessary. To you both, I thank you for giving me the space to open my eyes. In the same sense, thanks to everyone I've played Dungeons and Dragons with — you allowed me to sit outside my head and remove myself from real life temporarily. Ben, Mihai; though I missed you in the last year or so of my PhD, your presence was indispensable. Thank you for the times past and for the times ahead. My oldest friends Ella and Sophie deserve the sincerest thanks for their continued friendship — here's to another 15 tumultuous years! I'm grateful to the hodgepodge that is the M9s for always permitting Scooter and Cascada full blast in times of peril. My good friends and bandmates, Jack and Jacob;

Havelocke has allowed me to keep my sanity in times where I thought it was impossible and gave me an outlet for my frustrations when life seemed dark.

To those of you not mentioned here, I haven't forgotten you! Anyone who has shared in my good times and bad, please know that this thesis is yours as much as it is mine.

Declaration of Authorship

I hereby declare that except where specific reference is made to the work of others, the contents of this dissertation are original and have not been submitted in whole or in part for consideration for any other degree or qualification in this, or any other university. This dissertation is my own work and contains nothing which is the outcome of work done in collaboration with others, except as specified in the text and Acknowledgements. This dissertation contains fewer than 80,000 words including appendices, bibliography, footnotes, tables and equations.

Hope Thackray
December 2019

Abstract

The use of waves as a diagnostic tool for determining unknown parameters has been indispensable in the research of the Sun. Since the discovery of the mystery of solar coronal heating in the 1940s, solar structures have been studied using seismology, particularly in the corona, in hope of finding the root cause of magnetic energy release. In this thesis, waves, flows, and oscillations associated with solar coronal loop structures and their origins beneath the surface are examined, since the dissipation of waves is believed to contribute to the bulk heating of the corona.

First, a waveguide in Cartesian coordinates is studied, modelling a coronal loop arcade with curved magnetic field lines embedded in plasma with density decreasing exponentially in height. Investigating a small perturbation around the equilibrium, the fast and Alfvén modes are decoupled. Depending on the ratio between the gas and magnetic pressure scale heights, the fast modes were shown to either be decaying or growing in height. In the presence of a Gaussian perturbation at the loop apex, the power in the Alfvén mode, and for a special case of the fast mode, could be calculated for each eigenfrequency. It was shown that the power was highest for small eigenfrequencies in both cases, with the largest frequencies contributing the least.

Since we see coronal loops as brighter than their surroundings, a "two-shell" (and later "three-shell") density profile of a magnetic field lines in a model in cylindrical coordinates is introduced. The coronal loops are considered to sit at the interface, and for the line-tying condition resultant eigenfrequencies are investigated. We investigate the resulting eigenfunctions for a "two-shell" (and later "three-shell") density profile model that introduces sharp density contrast. we find that waves are elliptically polarised, but the eigenmodes can differ significantly when considering small changes

to density profile. Hence, we conclude that the choice of density structure for use with observational data must be made with caution so that mode identification can be made more accurately.

Finally, by using the local helioseismological technique known as "Ring Diagram Analysis" with Doppler velocity shift data of the solar surface, the subsurface flows of flaring active regions from the rising phase of Solar Cycle 24 are examined. Consideration of morphological features, including X-class flare size, magnetic activity index, coronal mass ejection production and sunspot area, indicate that subsurface flow information should be used in tandem with the active regions morphology to ascertain the capability of large-scale flare production.

List of Publications

This thesis is based on the following publications:

- Thackray, H., Jain, R. (2017); Fast magnetohydrodynamic waves in a solar coronal arcade, *Astron. Astrophys.*, Volume 608, A108
- Thackray, H., Jain, R., Jain, K., Tripathy, S. C., Hill, F.; Subsurface flows of active regions associated with eruptive and confined flares in Solar Cycle 24, *Astron. Astrophys.*, recommended for publication pending revisions (Dec 2019)

Contents

List of Figures

CHAPTER 1
Introduction

"See that ball of fire in the sky? That's the sun.
It goes by many names: Apollo's lantern, day moon, old blazy.
The important thing is, never to touch it."
- Homer Simpson

1.1 The Sun

The importance of the Sun in life on Earth has been understood since, possibly, the dawn of time, fundamental to the production of food sources and warmth. This cardinal object has provoked such mystery, with its physical distance from the Earth a substantial 149.6 million km, making for a rich field of research. From solar eclipses to solar flares, one cannot deny the fascination the Sun brings for all people. However, despite our closest star residing far from our small planet, there are many aspects of the Sun's existence which are well established, such as the processes by which it continues to thrive.

The Sun is comprised, predominantly, of hydrogen and helium, with the former providing fuel for the mechanism by which it continues to exist, by fusing the abundant hydrogen, forming helium in its place (see, for example, Priest (2013)). The presence of these elements in the Sun date back almost 4.6 billion years. At this point in time, the collapse of a molecular cloud (consisting of large quantities of hydrogen and helium) was triggered by a supernova-related shock wave (Cameron (1962); Williams (2010)). The resultant compression caused sections of the cloud to break down under intense gravitational forces, until rotation and heating from augmented pressure occurred. With gravity drawing matter into the centre of the rotating, rapidly heating mass, fusion began and a planetary disk formed around what was to become the Sun — and thus began our solar system (Nakano (1970); Montmerle *et al.* (2006)).

This giant (measuring approximately 6.95×10^5 km) is around 100 times the size of the Earth.

We start by describing the structure of the Sun, from the hot core, to its surface, and out into the atmosphere. For a more extensive review of the Sun's composition, see Priest (2013).

1.2 Structure

The Sun is fundamentally structured based on plasma of differing properties, with some of the most distinct layers detailed in Figure 1.1. In this thesis, we concentrate our studies mainly in the shallow region below the Sun's surface, or *photosphere*, and in the outer atmosphere, or *corona* (discussed in more detail in Sections 1.2.1 and 1.2.2). However, here we investigate some of the key features of the solar interior and the solar atmosphere, and how they differ.

1.2.1 The interior

The *core* lying at the very centre of the Sun is maintained through the balance of thermal pressure pushing outward, and pressure due to massive gravitational forces acting inwardly (Priest (2013)). At the hottest point, the temperature of the core is estimated to be around 15 million K, which falls to around 6000K at the Sun's surface. Despite the core's radius being around 20% that of the Sun itself, 50% of the Sun's mass is contained there. It is estimated that around 5×10^6 tonnes of hydrogen is fused each second, in a process known as nucleosynthesis (Hoyle (1946)), of which less than 1% is transformed into energy. Fusion of four protons from hydrogen into helium produces this energy, as two γ-rays and two electron neutrinos are released. These particles then easily pass through the core, radiating through the Sun.

Residing above the solar core is the *radiative zone*. The photons produced during fusion in the core proceed on a lengthy journey across this region. They are continually absorbed and exuded, before reaching the next layer, at a radius approximately 70% of the Sun, and a temperature around 10^6 K. This process may take years, resulting in transportation through the *convection zone*. The radiative and convective zones are separated by layer of strong shear, known as the *tachocline*, triggered by differential rotation. Energy is then transferred into plasma bundles in the form of thermal energy, causing them to rise convectively towards the Sun's surface, or *photosphere*, where the solar atmosphere begins. In doing so, heat is lost in the surroundings, and the

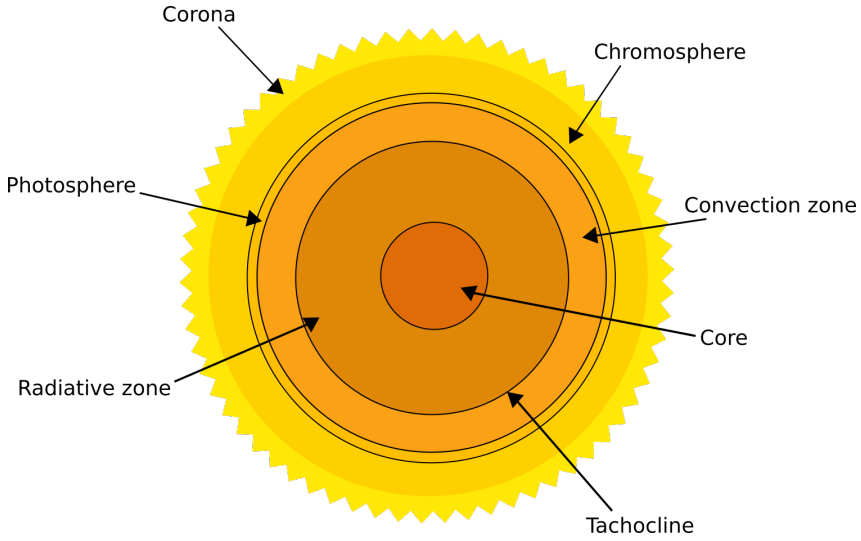

Figure 1.1: A diagram detailing the layers of the Sun.

bundles cools down before falling back to the bottom of the convective layer, continuing the process in a cyclic manner.

1.2.2 The atmosphere

The convective motion is seen at the surface in two forms: granulation and supergranulation. The former is more distinct, since the convective motions beneath the surface drive plasma upward through the centre of the granules, before the cooled plasma falls between the adjacent granules. These cooler paths forming the granulation are known as *intergranular lanes*. Such structures may reach scales of around $1Mm$. Supergranulation is a weaker form of convective motion, covering a much larger scale, up to $70Mm$.

The largest scale flows exhibited at the solar surface are *differential rotation* and *meridional flow*. The main feature of differential rotation is that the equator appears to rotate much faster than regions of higher (or, indeed, lower) latitude. Meridional flow, related to differential rotation, is exhibited as poleward motion at the surface, away from the equator in each hemisphere. A shallow region of such flows below the solar surface may be probed by seismological methods, which will be covered briefly in Section 1.4.2, and more substantially in Section 4.2.

In the context of this thesis, features of major interest in the photosphere are magnetic *active regions*. Whilst granules appear as bright, hot patches, surrounded by darker, cooler lanes, active regions appear as clusters of intensely dark *sunspots*. These relatively cold regions are manifestations of the

points where intense bundles of magnetic field lines intersect the surface. Typically, an active region consists of a "preceding" sunspot group and a "follower" sunspot group, and can usually be divided into two groups of opposite polarity. However, more active regions with more complex polarity do exist. Their evolution usually occurs over the course of around one rotation of the Sun (around 25 days). Close to the edges of active regions, we see small bright flecks known as "faculae". These phenomena present themselves in white light since their plasma density is lower than the surrounding plasma.

The number of active regions, or indeed the number of sunspots, on the Sun's surface varies in an apparent 11-year cycle, known as the *solar cycle*. In periods of minimum activity, the Sun may go weeks without a single sunspot blemishing the surface, and the rising phase of the cycle tends to be shorter than the waning phase. In any case, the sunspots tracked in each hemisphere form a "butterfly diagram" from minimum to maximum (see Figure 1.2), indicating a bulk movement towards the equator as the Sun proceeds through the cycle. Additionally, the minimum phases of two adjacent solar cycles overlap, indicated by a cross-over between active regions belonging to different solar cycles at equatorial latitudes and latitudes closer to the poles.

Sunspots themselves cover areas around $15Mm$, but one active region may host tens or even hundreds of sunspots. Though the photosphere itself has an approximate temperature of 6000 K, sunspots may be as much as 1900 K cooler. The sunspot can be dissected into two distinct features: the *umbra* and the *penumbra*. The umbra is the dark centre of the sunspot, host to magnetic field lines penetrating the surface almost perpendicularly, whilst the lighter edge of a sunspot forms the penumbra. Groups of sunspots themselves are more likely to be of one polarity (known as an α-type group), but more complex groups of bipolar sunspots (known as β or γ-type), or sunspots with umbral polarity opposite that of the penumbra (known as δ spots) are not uncommon. Observations indicate that sunspots traverse the Sun much quicker than their host plasma, since they are probably rooted much deeper in the Sun's interior.

During periods of high magnetic activity, active regions may produce *solar flares*. These are sudden bursts of X-ray particles due to the quick release of energy, following the supposed interaction of magnetic field lines below the photosphere. Such events manifest as bright flashes in the *chromosphere* and lower corona, due to their interactions with the plasma. We cover flares in more detail in Section 4.1.

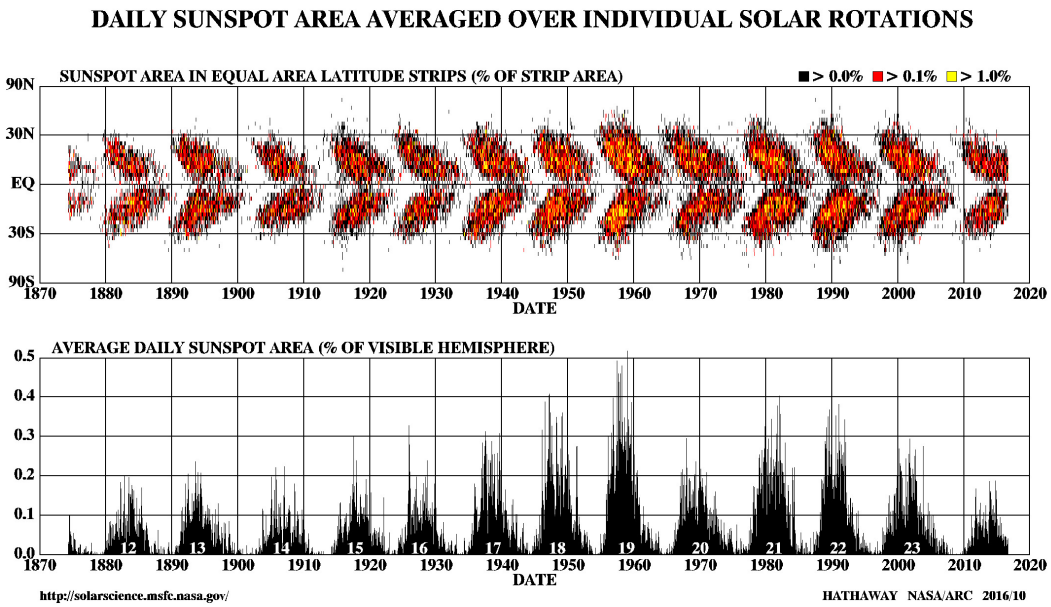

Figure 1.2: The sunspot cycle represented in a butterfly diagram, showing the location of sunspots (top) and the average area as a function of dates (bottom). Credit: NASA Marshall Space Flight Center.

Often related to solar flares are *coronal mass ejections* (CMEs), where hot, magnetically charged blobs of plasma are expelled explosively from the Sun. Once again, magnetic reconnection through the interplay of magnetic field lines is thought to be the trigger here. Usually, they are seen in observations as gargantuan "bubbles" bursting from a localised region of the Sun. Occasionally, this cloud of magnetic plasma may swell much larger than the Sun itself and be seen on all sides as a *halo* CME. The combination of Earth-ward flaring and CME production is a highly researched area of space-weather, following their propensity to cause geomagnetic events through the interaction of particles and plasma with the Earth's magnetosphere. Though rare, such eruptive events can damage satellites, cause interruptions to communications related to space and air travel, and in the most extreme cases may disrupt transformers in power stations.

Sunspots within active regions may be linked by tall, overlying arching magnetic field lines, known as *coronal loops*. Most often, these structures lie in bundles or "arcades" that are observed as bright, dense loops of hot plasma. During the eruption of a nearby solar flare, blast waves directed toward the loops cause them to oscillate, much like the "pluck" of a guitar string. It is the transfer of energy through the dissipation of the loop oscillations to the surrounding plasma which is thought to be one of the contributors to coro-

nal heating: it is known that the temperature rises as one traverses upwards through the corona. This is counter-intuitive — it is expected that as you travel further from a source of thermal energy, the temperature should decrease. Hence, there must be some mechanism by which transfer of energy causes heating in the corona.

The theoretical study of these mechanisms behind coronal heating is generally investigated in the framework of *magnetohydrodynamics*, in the context of wave theory. In the next Section, we discuss the basics of magnetohydrodynamics, with the assumptions made throughout this thesis.

1.3 Magnetohydrodynamics

Since the Sun is comprised, to reduce it to its simplest description, of plasma and magnetic fields, it follows that many features of the Sun are best described using *magnetohydrodynamics* (MHD). The derivation of the equations governing magnetohydrodynamic structures is given in the following section.

1.3.1 Governing equations

To derive the MHD equations, some assumptions must be made: we assume that the corona is host to an electrically neutral plasma, so that the resident electric field strength is not too large. Additionally, the length and time scales must both be long in comparison to the ion gyroradius and ion gyration time, respectively, so that the plasma may be treated as a continuum and does not evolve too quickly.

We must begin with Maxwell's equations, describing the electric and magnetic fields. Firstly, we give the solenoidal constraint, which ensures the absence of magnetic monopoles in the field:

$$\nabla \cdot \mathbf{B} = 0. \tag{1.1}$$

The vector $\mathbf{B}$ describes magnetic induction (i.e. the magnetic field). Next, assume that there is conservation of electric charge: this produces Gauss' law, given by

$$\nabla \cdot \mathbf{E} = \frac{1}{\epsilon_0}\rho^*, \tag{1.2}$$

where $\mathbf{E}$ is the electric field, ϵ_0 is the permittivity of free space and ρ^* is the charge density.

At this point, we may introduce Faraday's law, whereby an electric field varying in space gives rise to magnetic induction:

$$\nabla \times \mathbf{E} = -\frac{\partial \mathbf{B}}{\partial t}. \tag{1.3}$$

Finally, the set of equations is completed, with the introduction of Ampere's law, such that electric currents are invoked by gradients in the magnetic field:

$$\nabla \times \mathbf{B} = \mu_0 \mathbf{J} + \frac{1}{c^2}\frac{\partial \mathbf{E}}{\partial t}. \tag{1.4}$$

Here, $\mathbf{J}$ is the current density, and μ_0 and c are the is the magnetic permeability and the speed of light in a vacuum, respectively.

Now, we take the MHD assumption that plasma velocities are significantly smaller than c, and the second term in Equation (1.4) becomes negligible. Hence, this may be re-written as

$$\nabla \times \mathbf{B} = \mu_0 \mathbf{J}. \tag{1.5}$$

In a similar manner, the governing electric fields of the structure are assumed to be dominantly generated by the evolution of the magnetic field in time, so that the right hand side of Equation (1.2) assumed to be zero.

Ohm's law may be introduced here, where current density can be described using the total electric field and the induced current generated due to fluid flow through a magnetic environment ($\mathbf{v} \times \mathbf{B}$):

$$\mathbf{J} = \sigma(\mathbf{E} + \mathbf{v} \times \mathbf{B}). \tag{1.6}$$

Combining Equations (1.5) and (1.6), we obtain

$$\eta \nabla \times \mathbf{B} = (\mathbf{E} + \mathbf{v} \times \mathbf{B}), \tag{1.7}$$

where $\eta = \frac{1}{\mu_0 \sigma}$ is the magnetic diffusivity, and taking the curl of both sides yields

$$\nabla \times \eta(\nabla \times \mathbf{B}) = \nabla \times (\mathbf{E} + \mathbf{v} \times \mathbf{B}). \tag{1.8}$$

The *induction equation* may then be obtained by using a vector identity, and the re-introduction of Equations (1.1) and (1.3), and is described by

$$\frac{\partial \mathbf{B}}{\partial t} = \nabla \times (\mathbf{v} \times \mathbf{B}) + \eta \nabla^2 \mathbf{B}, \tag{1.9}$$

for a uniform η. The equation gives information about how the magnetic field changes in time.

As MHD concerns the interactions of plasma in the presence of a magnetic field, it follows that Navier-Stokes equation may be used to describe the flow of the fluid, which has the form

$$\rho\left(\frac{\partial \mathbf{v}}{\partial t} + (\mathbf{v}\cdot\nabla)\mathbf{v}\right) = -\nabla p + \rho\nu\nabla^2\mathbf{v} + \rho_c\mathbf{E} + \mathbf{J}\times\mathbf{B} + \mathbf{F}. \tag{1.10}$$

Here, ρ, p and ν give the plasma density, gas pressure and viscosity respectively. In this context, ρ_c is the unit volume electrical charge, which may be neglected due to electrical neutrality, and the term $\mathbf{J}\times\mathbf{B}$ is called the *Lorentz force*. The vector F contains information about any other forces which may be affecting the system, such as gravitational forces, $\rho\mathbf{g}$.

Finally, we introduce the continuity equation, which ensures conservation of matter, and the energy equation:

$$\frac{\partial \rho}{\partial t} + \nabla\cdot(\rho\mathbf{v}) = 0, \tag{1.11}$$

$$\frac{\partial p}{\partial t} + \mathbf{v}\cdot\nabla p + \gamma p\nabla\cdot\mathbf{v} = 0. \tag{1.12}$$

The parameter γ is the ratio of specific heats, and, in the context of this thesis, the plasma is assumed to be adiabatic.

Hence, the MHD equations for an inviscid fluid may be summarised by the following:

$$\rho\left(\frac{\partial \mathbf{v}}{\partial t} + (\mathbf{v}\cdot\nabla)\mathbf{v}\right) = -\nabla p + \mathbf{J}\times\mathbf{B} + \rho\mathbf{g}, \tag{1.13}$$

$$\frac{\partial \rho}{\partial t} + \nabla\cdot(\rho\mathbf{v}) = 0, \tag{1.14}$$

$$\frac{\partial p}{\partial t} + \mathbf{v}\cdot\nabla p + \gamma p\nabla\cdot\mathbf{v} = 0, \tag{1.15}$$

$$\frac{\partial \mathbf{B}}{\partial t} = \nabla\times(\mathbf{v}\times\mathbf{B}) + \eta\nabla^2\mathbf{B}, \tag{1.16}$$

along with the additional constraint of

$$\nabla\cdot\mathbf{B} = 0. \tag{1.17}$$

In the context of this thesis, magnetic diffusivity is small and may be ignored. Thus, the induction equation in (1.16) can be reduced to

$$\frac{\partial \mathbf{B}}{\partial t} = \nabla\times(\mathbf{v}\times\mathbf{B}). \tag{1.18}$$

This form of MHD is known as "ideal MHD", and will be used throughout this thesis.

MHD is considered useful for modelling wave-like behaviour in the context of the Sun, and in particular the solar corona. In the next Section, we discuss the different types of magnetohydrodynamic waves which may be studied in coronal structures.

1.3.2 Magnetohydrodynamic waves

As mentioned in Section 1.2.2, structures in the solar corona may be prone to oscillatory behaviour, following eruptive events. More broadly speaking, waves are omnipresent in solar structures, not limited to the corona.

In this section, we develop the basics of MHD waves, by considering small perturbations around an equilibrium. To do so, let the parameters of the MHD equations in (1.13)-(1.16) be written in terms of an equilibrium (denoted by subscript "0") and a perturbed (denoted by subscript "1") quantity:

$$\mathbf{B} = \mathbf{B_0}\left(\mathbf{r}\right) + \mathbf{B_1}\left(\mathbf{r}, t\right), \tag{1.19}$$

$$\mathbf{v} = \mathbf{v_0}\left(\mathbf{r}\right) + \mathbf{v_1}\left(\mathbf{r}, t\right), \tag{1.20}$$

$$\rho = \rho_0\left(\mathbf{r}\right) + \rho_1\left(\mathbf{r}, t\right), \tag{1.21}$$

$$p = p_0\left(\mathbf{r}\right) + p_1\left(\mathbf{r}, t\right). \tag{1.22}$$

In addition, the equilibrium state is assumed to be static,

$$\nabla p_0 = \mathbf{J_0} \times \mathbf{B_0} + \rho_0 \mathbf{g}, \tag{1.23}$$

and $\mathbf{v_0} = 0$. As perturbations are assumed to be small, any products of perturbed quantities can be ignored. Hence, the ideal MHD equations and solenoidal constraint may be linearised, yielding

$$\rho_0 \frac{\partial \mathbf{v_1}}{\partial t} = -\nabla p_1 + \frac{1}{\mu_0}\left[\left(\nabla \times \mathbf{B_0}\right) \times \mathbf{B_1} + \left(\nabla \times \mathbf{B_1}\right) \times \mathbf{B_0}\right] + \rho_1 \mathbf{g}, \tag{1.24}$$

$$\frac{\partial \rho_1}{\partial t} + \nabla \cdot \left(\rho_0 \mathbf{v_1}\right) = 0, \tag{1.25}$$

$$\frac{\partial p_1}{\partial t} + \mathbf{v_1} \cdot \nabla p_0 + \gamma p_0 \nabla \cdot \mathbf{v_1} = 0, \tag{1.26}$$

$$\frac{\partial \mathbf{B_1}}{\partial t} = \nabla \times \left(\mathbf{v_1} \times \mathbf{B_0}\right), \tag{1.27}$$

$$\nabla \cdot \mathbf{B_1} = 0. \tag{1.28}$$

In the solar corona, our region of interest, we assume that gravity has little effect on the magnetic field, and that the magnetic forces dominate (so that gas pressure gradients are negligible). This is known as the *zero-β approximation*, where β is defined by the ratio of gas pressure to magnetic pressure.

To demonstrate the types of waves produced in a purely magnetic background, we assume a very simple set-up: let there be a uniform equilibrium magnetic field, i.e. $\mathbf{B_0} = B_0\hat{\mathbf{B}}_\mathbf{0}$, where $\hat{\mathbf{B}}_\mathbf{0}$ is the unit vector in the direction of the magnetic field lines. To find wave solutions, we Fourier-analyse in space and time, as

$$\mathbf{v_1}(\mathbf{r}, t) = (v_x, v_y, v_z)e^{i(\mathbf{k}\cdot\mathbf{r}-\omega t)}, \tag{1.29}$$

where v_x, v_y and v_z are constant, so that for a general vector field $\mathbf{u}$

$$\nabla \cdot \mathbf{u} = i\mathbf{k}\cdot\mathbf{u}, \quad \nabla \times \mathbf{u} = i\mathbf{k}\times\mathbf{u}, \quad \frac{\partial \mathbf{u}}{\partial t} = i\omega\mathbf{u}. \tag{1.30}$$

Hence, Equations (1.24)-(1.28) may be re-written in terms of the Fourier components, as

$$\omega^2\rho_0\mathbf{v_1} = \frac{1}{\mu_0}[\mathbf{k}\times\{\mathbf{k}\times(\mathbf{v_1}\times\mathbf{B_0})\}]\times\mathbf{B_0}, \tag{1.31}$$

$$-i\omega\rho_1 + i\mathbf{k}\cdot\mathbf{v_1} = 0, \tag{1.32}$$

$$-i\omega\mathbf{B_1} = i\mathbf{k}\times(\mathbf{v_1}\times\mathbf{B_0}), \tag{1.33}$$

$$i\mathbf{k}\cdot\mathbf{B_1} = 0. \tag{1.34}$$

Taking the dot product of Equation (1.31) with $\mathbf{B_0}$, we see that $\mathbf{v_1}\cdot\mathbf{B_0} = 0$, and so the fluid motion occurs perpendicular to the background magnetic field lines. Additionally, manipulating the right hand side of (1.31) using vector identities gives

$$\omega^2\rho_0\mathbf{v_1} = \frac{1}{\mu_0}[(\mathbf{k}\cdot\mathbf{B_0})^2\mathbf{v_1} - (\mathbf{k}\cdot\mathbf{v_1})(\mathbf{k}\cdot\mathbf{B_0})\mathbf{B_0} + \{(\mathbf{k}\cdot\mathbf{B_0})(\mathbf{B_0}\cdot\mathbf{v_1})\}\mathbf{k}]. \tag{1.35}$$

Furthermore, we may introduce the quantity

$$v_A = \frac{B_0}{\sqrt{\mu_0\rho_0}}, \tag{1.36}$$

known as the *Alfvén speed*, to reduce Equation (1.35) to

$$\omega^2\mathbf{v_1} = v_A^2[(\mathbf{k}\cdot\hat{\mathbf{B}}_\mathbf{0})^2\mathbf{v_1} - (\mathbf{k}\cdot\mathbf{v_1})(\mathbf{k}\cdot\hat{\mathbf{B}}_\mathbf{0})\hat{\mathbf{B}}_\mathbf{0} + \{(\mathbf{k}\cdot\hat{\mathbf{B}}_\mathbf{0})(\hat{\mathbf{B}}_\mathbf{0}\cdot\mathbf{v_1})\}\mathbf{k}]. \tag{1.37}$$

By taking the dot product of (1.37) with $\mathbf{k}$, we finally arrive at the equation

$$(\omega^2 - v_A^2k^2)(\mathbf{k}\cdot\mathbf{v_1}) = 0. \tag{1.38}$$

There are two distinct solutions to the above equation, which yield different values for parameter ω, i.e. either

$$\omega = \pm v_A k \quad \text{or} \quad \mathbf{k}\cdot\mathbf{v_1} = 0. \tag{1.39}$$

We first consider the second solution: this is analogous to an incompressible perturbation, that is $\nabla \cdot \mathbf{v_1} = 0$. In this case, ω can be found from Equation (1.37). Setting $\mathbf{k} \cdot \mathbf{v_1} = 0$ yields

$$\omega = (\mathbf{k} \cdot \hat{\mathbf{B}}_\mathbf{0}) v_A. \tag{1.40}$$

Waves corresponding to this ω are known as *Alfvén waves*, propagating anisotropically to the equilibrium magnetic field, and transversely to the velocity perturbation. The phase speed of such solutions depends on the angle between the propagation vector and the magnetic field lines, reaching a maximum when waves are propagating in the same direction as the magnetic field. The first solution ($\omega = kv_A$) gives wave solutions known as *compressional Alfvén waves*, most commonly referred to as *fast modes*. Unlike the standard Alfvén wave, the angle of propagation does not affect the phase speed, which is constant. In the case where β differs from zero, the inclusion of gas pressure gives rise to the existence of a *slow mode*, whose phase velocity is influenced negatively by the interaction of the Alfvén speed and sound speed.

Though the wave solutions discussed in this section provide an elementary insight into the type of oscillations found in magnetic structures on the Sun, possible development of seismological techniques using robust models can enable us to infer unknown properties of the Sun and its structuring. Hence, we next discuss the use of seismology in the context of solar physics.

1.4 Seismology and the Sun

The use of waves in the understanding of plasma structures in the Sun has been vastly exploited in the past 40 years. Such studies are referred to as coronal seismology, in the context of structures in the corona, and helioseismology in the context of the Sun's interior. Here, we give a brief overview of the goals and results in both of these fields: for a more substantial overview of coronal seismology, see De Moortel (2005) and Nakariakov *et al.* (2016). Similarly, see Basu (2016), Thompson (2004) and Gizon and Birch (2005) for a comprehensive overview of both global and local helioseismology.

1.4.1 Coronal seismology: coronal loop structures

The coronal heating problem has been widely researched since its formulation in the mid-1900s (Alfvén and Lindblad (1947)). Its basis forms under the mystery that the corona is hot despite being further away from the Sun's heat

producing core. Hence, there must be some processes transferring magnetic or kinetic energy into thermal energy within the solar corona. There may not be one specific mechanism for the heating in the corona; it is more likely that a mixture of different processes could be contributing to the overall effect. One such process is suggested to be the transfer of energy from oscillating coronal loops to the background plasma by dissipation of oscillations (Ionson (1978); Heyvaerts and Priest (1983); Nakariakov (1999)).

Roberts *et al.* (1984) introduced the notion of seismology as a diagnostic tool for the solar corona, suggesting estimation of Alfvén speeds, and thus proving useful for determining physical properties of the cavities in which the wave reside. However, high-resolution observational data did not become available until the mid-90s with the launch of the Solar and Heliospheric Observatory (SOHO) and the Transition Region and Coronal Explorer (TRACE). This satellite allowed for unprecedented resolution imaging of the Sun, particularly in the EUV spectrum. In this range of wavelengths, the corona may be seen, with loops most visible at 171Å. However, variety in loop temperatures mean multi-wavelength analysis for coronal loops is important (see Section 3.1).

Most notably, in the context of this thesis, the observational analyses of Aschwanden *et al.* (1999) and Nakariakov (1999) uncovered the existence of spatial oscillations in coronal loops, and highlighted their importance in determining information about the magnetic field lying within the coronal structures. Additionally, such data could be used in conjunction with flaring events to investigate associated timescales and velocities, in the context of flare prediction. Later, Nakariakov and Ofman (2001) used observations from TRACE to determine the magnetic field strength from estimations of the density contrast in images of loop oscillations. Since this capability, the Solar Dynamics Observatory (SDO) was launched, with much higher-resolution imaging, bolstering the idea of coronal seismology.

More recently, seismology in the context of coronal loops has shown that variation of the magnetic field plays an important part in density stratification estimations (Verth and Erdélyi (2008)). By modelling the magnetic field lines using flux tube expansion, it was shown that even small changes to the ratio of the loop apex and footpoint radii gave rise to changes in oscillations. Since the cross-sectional area of the flux tube varies inversely to the strength of the magnetic field, density profile estimations must be made with this in mind. Further to this, statistical methods have been especially popular in the use of coronal seismology. Arregui and Asensio Ramos (2011) used Bayesian inversion

techniques in conjunction with synthetic data to determine density contrasts given only small amounts of information concerning pertaining to the densities, inhomogeneities and internal Alfvén speeds of the loop. Much more recently, investigation of damped modes in observational data by Pascoe *et al.* (2016) unearthed estimates of density contrast, leading to estimations of Alfvén speeds within the plasma, and thus much more accurate calculations concerning the magnetic field profile, through the addition of a profile describing the damping of the kink mode. The benefit of this was that the density contrast could be directly inferred, to some degree of error.

With the push for higher-resolution data, such as with the advent of the ground-based Daniel K. Inouye Solar Telescope (DKIST) in the near future, such seismological techniques will be adapted even further, to provide us with unrivalled estimates to unknown parameters in coronal structures.

1.4.2 Helioseismology

Whilst coronal seismology uses directly observed waves to infer physical parameters, helioseismology deals with oscillations of the solar interior, buried deep beneath the surface. The Sun's surface pulses like the beating of a giant heart — pressure modes, or p-modes are reflected off the photosphere, causing the surface to throb as they ricochet through the inner cavities of the Sun. These modes feed off the convective flows of the convection layer, and rely on pressure forces (giving them their moniker) to ensure their propagation. These modes bouncing away from the surface are slowed down by pressure gradients in the flow, causing them to slow down and change direction, before exciting them back towards the surface, where the process repeats (see Deubner and Gough (1984)).

Examination of these flows may be inferred from Dopplergrams — these are images of the solar surface which indicate flow of material towards or away from the observer. If flows beneath the surface are "quiet", that is, if there are no large gradients within the wavelength of the p-mode i.e no abnormal convective motions occur due to magnetic activity, the p-modes will oscillate without disturbance, tracing out a familiar pattern on a Dopplergram image. However, in the presence of magnetically active regions these flows beneath the surface may become drastically altered, causing the usual cavities to become distorted (Christensen-Dalsgaard (2002)). The paths through which the p-modes traverse will thus change, with uncertainty in where they may now hit the surface interior. Hence, there will be shifts in the frequencies at the

oscillations, presented as Doppler shifts at the surface, which, are then used to give information about the changes to the cavities below (Campbell and Roberts (1989); Goldreich *et al.* (1991); Jain and Roberts (1993)).

There are a few methods through which one may try to estimate these changes to flows beneath the surface: in this thesis, we cover the method of *Ring Diagram Analysis* (RDA) in detail (see Section 4.3), and will focus on findings using this method. Introduced in 1988 (Hill (1988)), RDA is employed in the context of *local helioseismology*, rather than the wide-spread global helioseismological research on features such as granulation. Information about the *horizontal* flows beneath the surface i.e. those which are parallel to the equator (*zonal* flows) and those which are poleward (*meridional* flows), are inferred by inverting Doppler shift information from Dopplergrams (covered in more detail in Section 4.3). Vertical flows, i.e. those in a direction normal to the solar surface, may be deduced using the solar model as described in Christensen-Dalsgaard *et al.* (1996), but rely on assumptions to the vertical flow velocity at the surface, and may therefore be unreliable.

The range of research covered using RDA is vast, and a good summary of recent advances may be found in the review by Baldner *et al.* (2013). However, many studies focus on the evolution of the zonal and meridional flows across the solar cycle (Hernandez (2008); Komm *et al.* (2014); Komm *et al.* (2015); Komm *et al.* (2017)), changes to flows beneath active regions during flaring events (Komm *et al.* (2005); Reinard *et al.* (2010); Jain, Tripathy and Hill (2015); Jain *et al.* (2017)), and effects of the Sun's torsional oscillations, which present themselves as strips of rotation occurring at faster or slower rates than expected, migrating from the equator and towards the poles as the Sun varies in magnetic activity (Howe *et al.* (2006); Bogart *et al.* (2015); Lekshmi *et al.* (2018)).

1.5 Outline

The main focus of this thesis concerns investigating the observed oscillations in the corona during flaring events and their possible triggering mechanisms. Since observations may be used with coronal loop models to estimate unobservable parameters, developing a robust theoretical model for arcades remains an important issue (further discussed in Chapter 3). As for the triggering mechanisms, we need to consider perturbations that affect the visible loop directly or

their footpoint motions below the surface. We examine both of these (Chapters 2 and 4). The aim is to tie together the changes undergone beneath the solar surface with the observed effects in the corona.

We begin with the introduction of a Cartesian model for coronal loop structures in Chapter 2. Curvature in coronal arcade models is discussed, as well as some results from preliminary examination of loop structures using straight cylindrical and slab models. Next, we assume the density in the structure to be varying vertically, and the underlying magnetic field to be curved. Here, resultant Alfvén and fast modes are shown to be de-coupled and investigated, before examining the power spectra excited following an initial perturbation. The bulk of the investigation is demonstrated for arbitrary parameters, but we show that there are limitations to this for the geometries given. By introduction of a sharp density interface at a certain height, we demonstrate the effects of density profile choice on resultant eigenfrequencies.

Next, in Chapter 3, a coronal loop model in cylindrical coordinates is introduced, by considering semi-circular field lines anchored in the photosphere. Observational evidence for loop structures as bands of differing density to their environments is discussed, highlighting the necessity for a discontinuous density structure. The loops are first considered as lying at the interface of a sharp density discontinuity, and then considered with the addition of a second interface. Once again, the changes to eigenfrequencies are discussed, and the validity of the geometry considered with respect to the physical properties of the coronal loop structure. We show the necessity of modelling a coronal arcade in three dimensions and the elliptical polarisation of the waves emphasised.

The waves found in coronal loop structures are only half the story of a solar eruptive event. Chapter 4 sees the use of observational data in the context of active regions where the loops show oscillations, and thus an investigation of subsurface flow pattern. Ring diagram analysis is used to investigate the flows beneath 10 flaring and 2 non-flaring active regions. Different approaches to analysis are discussed, signatures in the flow analysed, and the restrictions and implications of the ring diagram analysis explored.

CHAPTER 2

A solar coronal arcade in Cartesian coordinates

2.1 Introduction

Coronal loops are known to oscillate, often in response to nearby eruptive events, such as solar flares. The footpoints of the loops penetrating the photosphere, they are most often found to be between sunspots, high above solar active regions (Priest (2013)). For the sake of simplifying the physical characteristics of coronal loops in the context of mathematical modelling, one of the most common geometries used is that of a straight magnetic flux tube (for example, Edwin and Roberts (1983)), as illustrated in Figure 2.1.

The inaugural case of this model in the context of coronal loops (Edwin and Roberts (1983)) demonstrates that, for loops with a density higher than the background density, fast modes exist in the form of *sausage* and *kink* modes (see Figures 2.2 and 2.3). Kink modes occur when the oscillation perturbs the cylinder axis, and sausage modes when they do not. Since Edwin and Roberts (1983) also consider the effects of a pressure gradient on the possible modes, there is also the existence of a *slow* mode (indicated in Figure 2.2), which occurs due to the interplay between magnetic forces and gas pressure.

Another, slightly less common, form of model for coronal loop structures is the magnetic slab (see Terradas *et al.* (2005); Gruszecki *et al.* (2007); Arregui *et al.* (2007); De Groof *et al.* (2002)), first introduced in Roberts (1981), where the slab resides in non-magnetic background, and then again in Edwin and Roberts (1982), where the background is magnetised. The geometry is demonstrated in Figure 2.4. In the same way that sausage and kink modes are produced in a cylinder, sausage and kink modes are produced in slab geometry, where sausage indicates the slab interfaces moving out of phase with each other, and kink indicates the slab interfaces moving in phase with each other.

The distinct property of the two models discussed above is that both are modelling coronal loops as straight entities — in reality, these structures are

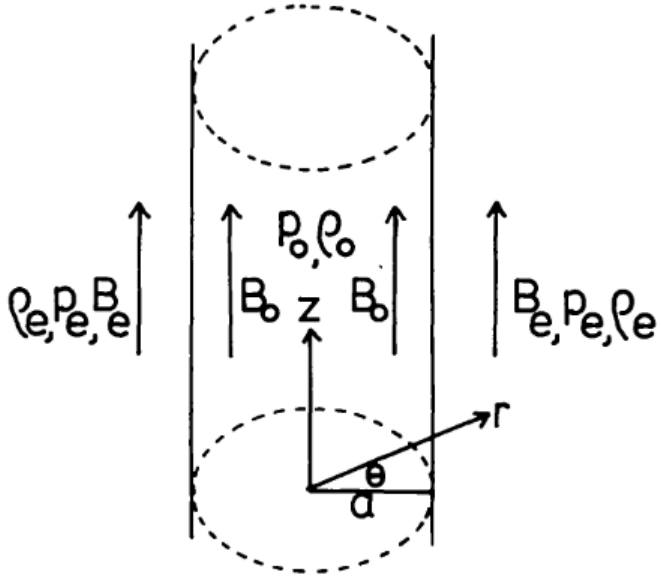

Figure 2.1: A magnetic cylinder as depicted in Edwin and Roberts (1983). Here, subscript "e" indicates quantities outside the tube, and subscript "0" indicates quantities inside the tube.

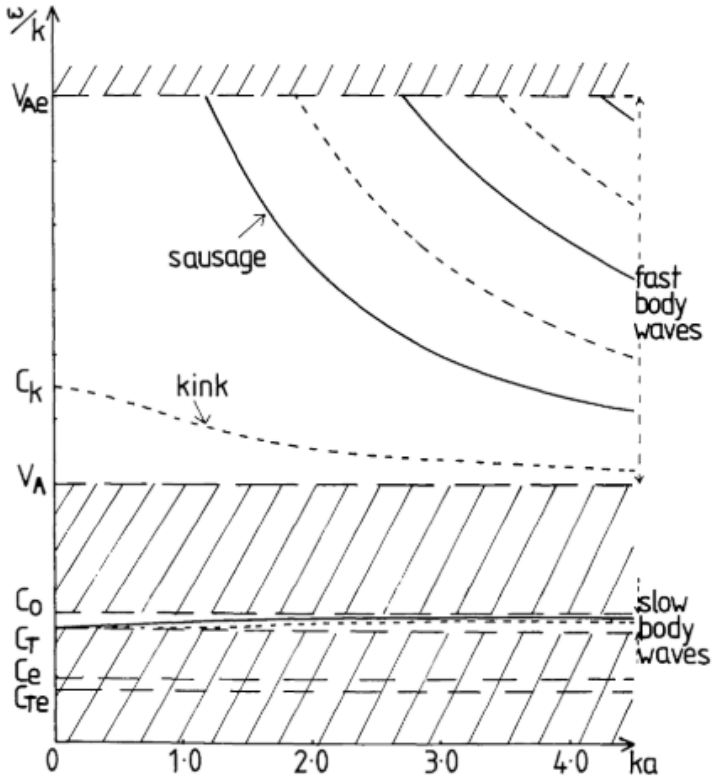

Figure 2.2: The wave solutions for the magnetic cylinder in Figure 2.1, in the limit for coronal loops. Courtesy of Edwin and Roberts (1983).

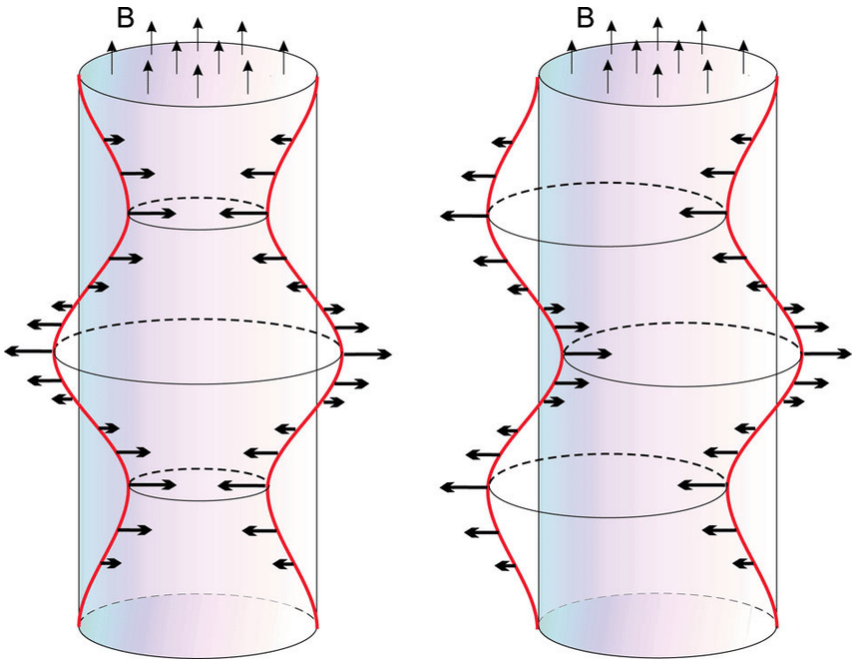

Figure 2.3: Sausage (left) and kink (right) modes in a magnetic cylinder. Credit: Solar Wave Theory Group.

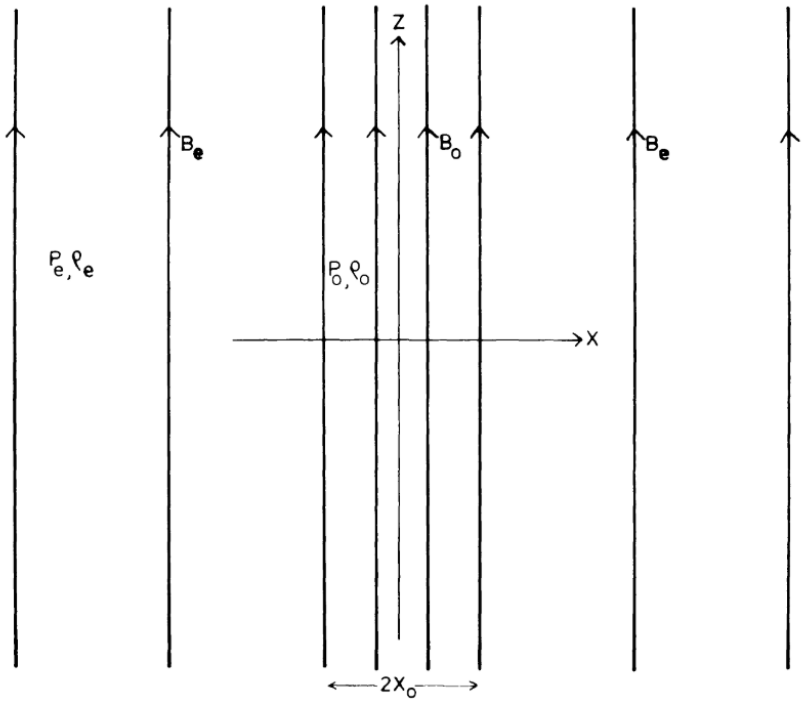

Figure 2.4: A magnetic slab as depicted in Edwin and Roberts (1982). Here, subscript "e" indicates quantities outside the slab, and subscript "0" indicates quantities inside the slab.

curved, and the effects of curvature in coronal loop geometries on the existence of wave modes was examined in detail by Van Doorsselaere *et al.* (2009). There the curved nature of the waveguide yields both vertically and horizontally polarised waves. As pointed out by Hindman and Jain (2018), the simplification of coronal loop structures to straight cylinders or slabs results in the reduction of the propagating wave solutions to one dimension in most cases and hence, the true 3D waveguide is not examined for the propagation of MHD waves in the context of coronal loops. It is also worth noting that in many of the models, the background is assumed to be constant. Hence, we limit our studies to coronal loop geometries involving curvature, in a magnetised background.

Here, we investigate Alfvén and fast modes of curved coronal loop structure modelled in Cartesian coordinates, following Oliver *et al.* (1993). Once solutions are found, the excitation of both modes following an initial perturbation may be investigated, as in Tarr (2017). Finally, by introduction of a small region provoking a density contrast, we show that the effects on frequencies may be drastic.

2.2 Geometrical set up

First, we describe the model set-up, followed by the derivation of the governing equations. The geometry is proposed as follows: we assume loop-like structures exist in the corona, close to the photosphere. There, a magnetohydrostatic equilibrium may be described, where Lorentz force, gradient of the equilibrium plasma pressure and the force due to gravity are balanced:

$$\mathbf{J_0} \times \mathbf{B_0} - \nabla p_0 + \rho_0 \mathbf{g} = 0. \tag{2.1}$$

Projecting this along the magnetic field lines yields the relation

$$\frac{\partial p_0}{\partial s} + \rho_0 g \cos(\theta) = 0 \tag{2.2}$$

$$\implies \frac{\partial p_0}{\partial z} + \rho_0 g = 0 \tag{2.3}$$

where θ is the angle between the field line and the z-axis (see Priest (2013)), and pressure and density are both functions of height z. Here, the parameter s is the distance measured along any field line.

Hence, assuming that the corona follows the ideal gas law, the density may be written in terms of the pressure as

$$\rho_0 = \frac{p_0 m}{k_B T}, \tag{2.4}$$

where T is a constant temperature, k_B is the Boltzmann constant and m is the mean particle mass. Substituting for p_0 from Equation (2.4) into (2.3), and using the method of separation of variables, we can find the density as a function of z, which, in terms of the pressure scale height, H, is:

$$p_0(z) = p_0 e^{-z\frac{mg}{k_B T}} = p_0 e^{-\frac{z}{H}}, \tag{2.5}$$

for some constant p_0. It follows that the density, $\rho_0(z)$ can be written in a similar fashion, with ρ_0 constant:

$$\rho_0(z) = \rho_0 e^{-\frac{z}{H}}. \tag{2.6}$$

Approximating the corona as a zero-β plasma, and considering a negligible effect from gravity (i.e. across distances much lower than the pressure scale height), the Lorentz force $\mathbf{J_0} \times \mathbf{B_0} = 0$. Consequently, the magnetic field may be modelled as a potential field, that is $\nabla \times \mathbf{B_0} = 0$ (however, generally we may take any field satisfying the condition that $\mathbf{J_0} = \alpha \mathbf{B_0}$). In addition, this implies that the magnetic pressure scale height is very small in comparison to the gas pressure scale height. We will, however, include the case where the magnetic scale height comparatively large in our analysis, for completion.

Now, assume the field takes the form of a magnetic surface, invariant in the $\hat{\mathbf{y}}$-direction. The solenoidal condition (Equation (1.1) yields the background magnetic field:

$$\mathbf{B_0} = \nabla A(x, z) \times \hat{\mathbf{y}}. \tag{2.7}$$

Thus, $A(x, z)$ is a solution of Laplace's equation, i.e.

$$\nabla^2 A = 0, \tag{2.8}$$

which can be solved separably by imposing the boundary conditions of the coronal loop structure, that is, the potential field is not divergent at infinity and that the vertical component of the magnetic field is zero at the centre of the arcade. For symmetry, it is convenient to consider the structure centred on the y-axis, so that the magnetic field disappears at $x = 0$, as in Figure 2.5.

Assuming a solution of the form $A(x, z) = X(x)Z(z)$, Equation (2.8) has non-trivial solutions prescribed by the boundary conditions when

$$\frac{X''}{X} = -\frac{Z''}{Z} = -\alpha^2, \tag{2.9}$$

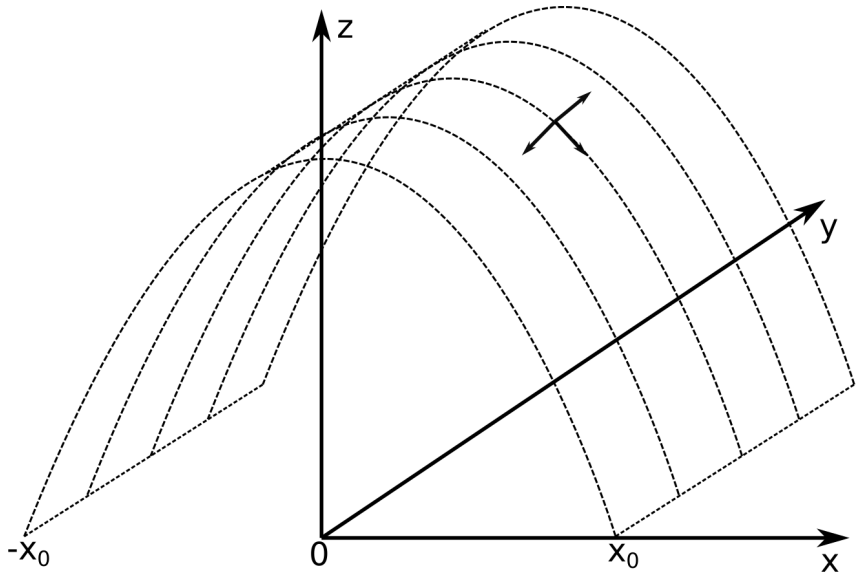

Figure 2.5: A diagram showing a possible configuration of a magnetic surface within the coronal arcade. The curved dashed lines indicate the magnetic field lines, and the orthogonal vectors associated with the structure are denoted by three arrows in the centre of the arcade. The structure is considered to be symmetric about the y-axis.

where α is a real constant. Here, $'$ denotes differentiation with respect to each of the arguments of the function. The function X therefore has a solution of the form

$$X(x) = A_0 \cos(\alpha x) + B_0 \sin(\alpha x), \tag{2.10}$$

for some constant coefficients A_0 and B_0.

If the arcade is assumed to have line-tied footpoints intersecting the $x - y$ plane, and a width of $2l$, then Equation (2.10) reduces to

$$X(x) = A_0 \cos\left(\frac{\pi x}{2l}\right), \tag{2.11}$$

so that boundary conditions at $x = \pm l$ yield an even function in x for the magnetic field.

Here, Equation (2.11) may be written more succinctly as

$$X(x) = A_0 \cos\left(\frac{x}{H_B}\right), \tag{2.12}$$

where $H_B = \frac{2l}{\pi}$ is known as the magnetic scale height. Solving in a similar way for Z, and only allowing solutions convergent as height increases, the solution may be written

$$A(x, z) = B_0 H_B \cos\left(\frac{x}{H_B}\right) e^{-\frac{z}{H_B}}. \tag{2.13}$$

The constant coefficient has been chosen such that the background magnetic field is $B = B_0$ at $z = 0$. Equation (2.13) then dictates the magnetic field profile:

$$\mathbf{B} = \left(B_0 \cos\left(\frac{x}{H_B}\right) e^{-\frac{z}{H_B}}, 0, -B_0 \sin\left(\frac{x}{H_B}\right) e^{-\frac{z}{H_B}} \right). \tag{2.14}$$

Figure 2.5 depicts a particular arrangement of one such magnetic surface, centred on $x = 0$, with arbitrary footpoints crossing the x-y plane at $x = \pm x_0$.

2.3 Linearised momentum equation

Considering small perturbations in the equilibrium state, the linearised momentum equation in the ideal limit (i.e. where the fluid can be modelled as perfectly conducting), for a zero-β plasma is

$$\rho_0(z)\frac{\partial \mathbf{v_1}}{\partial t} = \mathbf{J_1} \times \mathbf{B_0}, \tag{2.15}$$

following a similar procedure to Section 1.3.2. We assume that the gas pressure variation and variation due to gravity is small in comparison to the effects of the magnetic field, as in the coronal approximation.

Since $\mathbf{J_1} = \frac{1}{\mu_0}(\nabla \times \mathbf{B_1})$, we can rewrite (2.15), to give

$$\rho_0(z)\frac{\partial \mathbf{v_1}}{\partial t} = \frac{1}{\mu_0}[(\nabla \times \mathbf{B_1}) \times \mathbf{B_0}]. \tag{2.16}$$

Taking the derivative of (2.16) with respect to time yields

$$\rho_0(z)\frac{\partial^2 \mathbf{v_1}}{\partial t^2} = \frac{1}{\mu_0}\left[\left(\nabla \times \frac{\partial \mathbf{B_1}}{\partial t}\right) \times \mathbf{B_0}\right], \tag{2.17}$$

where we can use the linearised induction equation in the first term to obtain

$$\rho_0(z)\frac{\partial^2 \mathbf{v_1}}{\partial t^2} = \frac{1}{\mu_0}[\nabla \times \{\nabla \times (\mathbf{v_1} \times \mathbf{B_0})\}] \times \mathbf{B_0}, \tag{2.18}$$

where $\mu_0 = 1$ can be taken for convenience (see Chapter 1 for the derivation). Here, $\mathbf{v_1}$ is the perturbed velocity. We can consider the velocity field in terms of the orthogonal basis composed of a vector parallel to the magnetic field, $\frac{\mathbf{B_0}}{|\mathbf{B_0}|}$, a vector perpendicular to the field lines, $\hat{\mathbf{y}}$, and a vector normal to the surface, $\frac{\nabla A}{|\nabla A|}$.

First, the right hand side of Equation (2.18) can be written in terms of the cross product in Equation (2.7):

$$[\nabla \times \{\nabla \times (\mathbf{v_1} \times \mathbf{B_0})\}] \times \mathbf{B_0} = [\nabla \times \{\nabla \times (\mathbf{v_1} \times \mathbf{B_0})\}] \times (\nabla A \times \hat{\mathbf{y}}). \tag{2.19}$$

By vector identities,

$$\nabla \times (\mathbf{v_1} \times \mathbf{B_0}) = \nabla \times (v_y \nabla A - (\mathbf{v_1} \cdot \nabla)\hat{\mathbf{y}}) \tag{2.20}$$

$$= (\nabla v_y \times \nabla A) - \nabla(\mathbf{v_1} \cdot \nabla A) \times \hat{\mathbf{y}}, \tag{2.21}$$

so that, using translation invariance in y, we may write

$$\nabla \times \{\nabla \times (\mathbf{v_1} \times \mathbf{B_0})\} = \nabla \times (\mathbf{B_0} \cdot \nabla v_y) - \nabla \times (\nabla(\mathbf{v_1} \cdot \nabla A) \times \hat{\mathbf{y}}) \tag{2.22}$$

$$= \nabla \times (\mathbf{B_0} \cdot \nabla v_y) + \hat{\mathbf{y}}(\nabla^2(\mathbf{v_1} \cdot \nabla A)) \tag{2.23}$$

$$= -\frac{\partial}{\partial z}[(\mathbf{B_0} \cdot \nabla)v_y]\hat{\mathbf{x}} + \frac{\partial}{\partial x}[(\mathbf{B_0} \cdot \nabla)v_y]\hat{\mathbf{z}} + \hat{\mathbf{y}}\left[\nabla^2(\mathbf{v_1} \cdot \nabla A)\right]. \tag{2.24}$$

Thus, taking the cross product of Equation (2.24), the right-hand side of Equation (2.18) may be expressed in terms of ∇A and $\hat{\mathbf{y}}$:

$$\rho_0(z)\frac{\partial^2 \mathbf{v_1}}{\partial t^2} = \left[\nabla^2(\mathbf{v_1} \cdot \nabla A)\right]\frac{\partial A}{\partial x}\hat{\mathbf{x}} + \left[\frac{\partial A}{\partial x}\left(-\frac{\partial}{\partial z}\left[(\mathbf{B_0} \cdot \nabla)v_y\right]\right) + \frac{\partial A}{\partial z}\left(\frac{\partial}{\partial x}\left[(\mathbf{B_0} \cdot \nabla)v_y\right]\right)\right]\hat{\mathbf{y}} + (\nabla^2(\mathbf{v_1} \cdot \nabla A))\frac{\partial A}{\partial z}\hat{\mathbf{z}} \tag{2.25}$$

$$= (\nabla^2(\mathbf{v_1} \cdot \nabla A))\nabla A + \left[(\mathbf{B_0} \cdot \nabla)^2 v_y\right]\hat{\mathbf{y}}. \tag{2.26}$$

Finally, Fourier-decomposition of the velocities in time as in $e^{i\omega t}$ yields

$$-\omega^2 \rho_0(z)\mathbf{v_1} = (\nabla^2(\mathbf{v_1} \cdot \nabla A))\nabla A + \left[(\mathbf{B_0} \cdot \nabla)^2 v_y\right]\hat{\mathbf{y}}. \tag{2.27}$$

Describing the governing equation in this way allows the deconstruction of perturbations into the fast mode (those in the ∇A direction), and the Alfvén mode (those in the $\hat{\mathbf{y}}$ direction).

2.4 Perpendicular perturbations: the Alfvén mode

Let us first examine the modes produced perpendicular to field lines, in the $\hat{\mathbf{y}}$ direction, known as the Alfvén modes. The governing equation for such modes has the form

$$-\omega^2 \rho_0 v_y = (\mathbf{B_0} \cdot \nabla)^2 v_y. \tag{2.28}$$

The magnetic field lines form magnetic surfaces where $A(x, z)$ is constant-valued, meaning that the potential field described by A may be written solely

in terms of either x or z. Subsequently, the potential may be evaluated at the footpoint of any field line, denoted generally as the point $(x, z) = (x_0, 0)$:

$$B_0 H_B \cos\left(\frac{x_0}{H_B}\right) = B_0 H_B \cos\left(\frac{x}{H_B}\right) e^{-\frac{z}{H_B}} \tag{2.29}$$

$$\implies \qquad z = H_B \ln\left(\frac{\cos\left(\frac{x}{H_B}\right)}{\cos\left(\frac{x_0}{H_B}\right)}\right). \tag{2.30}$$

Doing so allows for $\mathbf{B_0} \cdot \nabla$ to be written as a directional derivative in x, reducing Equation (2.28) to an ordinary differential equation. Taking the partial derivative of Equation (2.30) with respect to x gives

$$\frac{\partial z}{\partial x} = -\frac{\sin\left(\frac{x}{H_B}\right)}{\cos\left(\frac{x}{H_B}\right)} \tag{2.31}$$

$$= \frac{B_z}{B_x}, \tag{2.32}$$

by Equation (2.14). Hence,

$$\mathbf{B_0} \cdot \nabla = B_x \frac{\partial}{\partial x} + B_z \frac{\partial}{\partial z} \tag{2.33}$$

$$= B_x \frac{\mathrm{d}}{\mathrm{d}x} \tag{2.34}$$

$$= \frac{A}{H_B} \frac{\mathrm{d}}{\mathrm{d}x}. \tag{2.35}$$

Since the potential A is constant on these surfaces, we can take $A = A(x_0, 0)$, so that

$$\mathbf{B_0} \cdot \nabla = \frac{A(x_0, 0)}{H_B} \frac{\mathrm{d}}{\mathrm{d}x} \tag{2.36}$$

$$= B_0 \cos\left(\frac{x_0}{H_B}\right) \frac{\mathrm{d}}{\mathrm{d}x}. \tag{2.37}$$

Therefore, Equation (2.28) may be expressed solely in terms of x. Firstly, taking A as a constant along the field lines yields

$$-\omega^2 \rho_0(z) v_y = \left[\left(\frac{A}{H_B} \frac{\mathrm{d}}{\mathrm{d}x}\right)^2 v_y\right] \tag{2.38}$$

$$\implies \qquad -\omega^2 \rho_0(z) v_y = B_0^2 \cos^2\left(\frac{x_0}{H_B}\right) \frac{\mathrm{d}^2 v_y}{\mathrm{d}x^2}. \tag{2.39}$$

Next, note that the Alfvén speed $v_A(z) = \sqrt{\frac{B_0^2(z)e^{\frac{z}{H}}}{\rho_0}}$, $B_0^2(z) = B_x^2 + B_z^2 = B_0^2 e^{-\frac{2z}{H_B}}$, and $\delta = \frac{H_B}{H}$, and we may write

$$v_A(z) = \sqrt{\frac{B_0^2 e^{-\frac{2z}{H_B}} e^{\frac{z}{H}}}{\rho_0}} \tag{2.40}$$

$$= \sqrt{\frac{B_0^2 e^{-\frac{2z}{H_B}} e^{\frac{\delta z}{H_B}}}{\rho_0}} \tag{2.41}$$

$$= \sqrt{\frac{B_0^2 e^{-\frac{(2-\delta)z}{H_B}}}{\rho_0}}. \tag{2.42}$$

Depending on the value of δ, background equilibrium with different stratification may be investigated.

Denote the Alfvén speed at the bottom of the arcade (i.e. when $z = 0$) by v_0, so that $v_0 = \sqrt{\frac{B_0^2}{\rho_0}}$. Equation (2.39) may then be written fully in terms of x:

$$-\frac{\omega^2 \rho_0(z)}{B_0^2} \cos^{-2}\left(\frac{x_0}{H_B}\right) v_y = \frac{\mathrm{d}^2 v_y}{\mathrm{d}x^2} \tag{2.43}$$

$$\implies \quad \frac{\mathrm{d}^2 v_y}{\mathrm{d}x^2} + \frac{\omega^2}{v_0^2} \frac{\cos^{(\delta-2)}\left(\frac{x_0}{H_B}\right)}{\cos^{\delta}\left(\frac{x}{H_B}\right)} v_y = 0. \tag{2.44}$$

Depending on the value of δ, the solutions to Equation (2.44) differ in complexity. When $\delta = 0$, it may be solved analytically, resulting in a class of solutions dependent on the value of ω. Though a class of solutions may also be found for $\delta \neq 0$, Equation (2.44) must be solved numerically.

2.4.1 Gravity independent case

Let us first examine the case where the pressure scale height becomes extremely large. Gravity has no effect, meaning gas pressure and density do not vary in height, and the plasma can be considered to be zero-β. Such a limit reduces Equation (2.44) to a second order differential equation with constant coefficients:

$$\frac{\mathrm{d}^2 v_y}{\mathrm{d}x^2} + \frac{\omega^2}{v_0^2} \cos^{-2}\left(\frac{x_0}{H_B}\right) v_y = 0 \tag{2.45}$$

$$\implies \quad \frac{\mathrm{d}^2 v_y}{\mathrm{d}x^2} + k_x^2 v_y = 0, \quad \text{where} \quad k_x^2 = \frac{\omega^2}{v_0^2} \cos^{-2}\left(\frac{x_0}{H_B}\right). \tag{2.46}$$

We will henceforth refer to k_x as the wavenumber, and ω the eigenfrequency for the system. By writing the coefficient of v_y in such a way, the solutions are expressed succinctly in terms of cosine and sine functions as

$$v_y(x) = \begin{cases} A\cos(k_x x) \\ B\sin(k_x x) \end{cases}, \tag{2.47}$$

where the choice of solution depends on the necessity of an odd or an even perturbation, $v_y(x)$. Later, we choose an initial perturbation as an even function, so our analysis is limited to the even solution of Equation (2.47).

Now, assume the following boundary conditions: the footpoints of any magnetic surface are line-tied. That is, the perturbations v_y are zero at $x = \pm x_0$, for arbitrary footpoint locations $\pm x_0$. This allows for the eigenfrequencies $\omega^{(n)}$ to be defined for all Alfvén modes of the system:

$$k_x^{(n)} = \frac{(n+\frac{1}{2})\pi}{x_0}, \quad \text{for} \quad v_y = A\cos(k_x x), \quad n = 0, 1, 2, ... \tag{2.48}$$

$$k_x^{(m)} = \frac{m\pi}{x_0}, \quad \text{for} \quad v_y = A\sin(k_x x), \quad m = 1, 2, 3, ... \tag{2.49}$$

Thus, the eigenfunction solutions at each n are summed to give the perturbation function

$$v_y(x) = \sum_{n=0}^{\infty} A_n v_y^{(n)}(x). \tag{2.50}$$

Here, we take the same parameter values as in Tarr (2017), for comparison in the case of $\delta = 0$, and later $\delta \neq 0$. Figure 2.6 shows the first three even solutions to Equation (2.46). The line-tying condition means that all three modes are fixed at $v_y = 0$ for $x = \pm x_0$, with spatially symmetric amplitude oscillations occurring either side of $x = 0$. All three modes have amplitudes which are at a maximum magnitude at $x = 0$.

2.4.2 Magnetic pressure greater than gas pressure

When the parameter $\delta = 2$, the magnetic pressure and gas pressure decay at the same rate. Hence, when the value of $\delta = 0$, or if it sits between 0 and 2, the gas pressure decays more slowly than magnetic pressure (which is proportional to B^2). These sort of conditions are typical for the corona, where the magnetic pressure vastly outweighs that of gas pressure and the value of plasma-β may be considered to be 0.

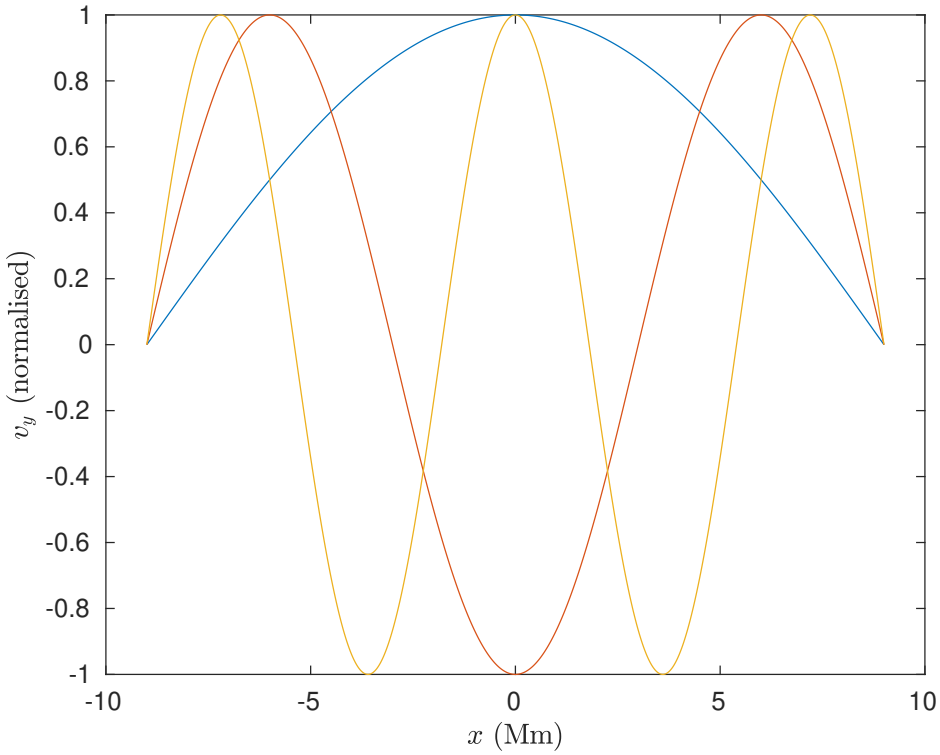

Figure 2.6: The first three even perturbations perpendicular to the field lines, normalised v_y, against x in Mm, for $\delta = 0$. The footpoints have been taken to be at $l = \pm 18Mm$, leading to an arcade width of $2l$. The magnetic scale height is $H_B = 11.66Mm$. The Alfvén speed at the footpoints is $v_0 = 1Mm$. Here, $n = 0$ is indicated by the blue line, the $n = 1$ by the red, and $n = 2$ by the yellow.

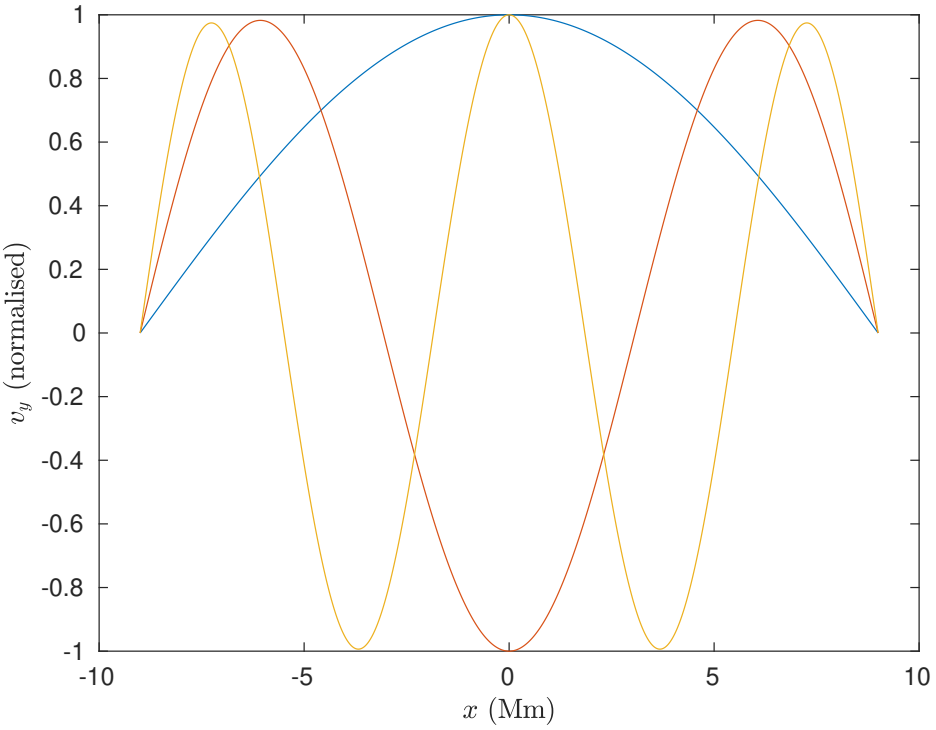

Figure 2.7: The first three even perturbations perpendicular to the field lines, v_y, against x in Mm, for $\delta = 0.5$, depicting the same modes, and for the same parameters as Figure 2.6.

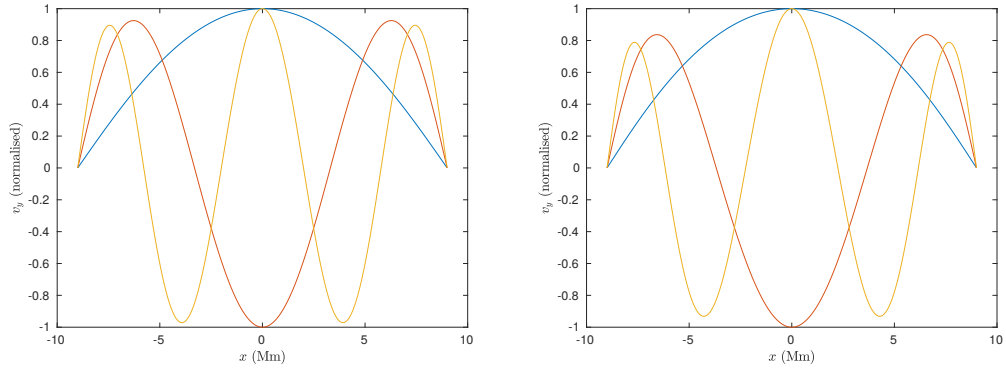

Figure 2.8: The first three even perturbations perpendicular to the field lines, v_y, against x in Mm, for $\delta = 2$ (left) and $\delta = 4$ (right), depicting the same modes, and for the same parameters as Figure 2.6.

Once again, the even perturbation v_y for the first three modes is plotted against x in Mm, shown in Figure 2.7. As in Figure 2.6, the maximum magnitude perturbation occurs at $x = 0$. However, either side of $x = 0$, the envelope of the modes has changed shape, tracing the outline of two curves above and below $v_y = 0$. This is not clear in the first mode, but is clear in the second and third modes, where lower peaks and troughs either side of $x = 0$ are clearly demonstrated.

2.4.3 Magnetic pressure less than or equal to gas pressure

Depending on the size or height of the coronal loop structure, it may be prudent to examine the model when $\delta > 2$, or when the magnetic scale height decreases more slowly than the pressure scale height. Increasing the value of δ changes the behaviour of perturbations either side of $x = 0$: this is illustrated in Figure 2.8, when the magnetic pressure and gas pressure have the same scale height $\delta = 2$ (left), and for $\delta = 4$ (right), respectively. As the value of δ increases, it is clear that the envelope of v_y either side of $x = 0$ is lower in comparison to those in the $\delta = 0$ case (Figure 2.6), and the $\delta = 0.5$ case (Figure 2.7). As the value of δ increases, the higher order modes become noticeably more dampened either side of $x = 0$.

2.4.4 Excitation of Alfvén modes

Further to the examination of Equation (2.44) in the case where $\delta = 0$, Tarr (2017) investigated an initial Gaussian perturbation on the Alfvén modes,

situated at the apex of the loops. For some small width w, an (even) function of the form

$$v_y(x) = \frac{1}{\sqrt{2\pi}w} e^{-\frac{x^2}{2w^2}} \tag{2.51}$$

is projected onto the even perturbations v_y, as in Equation (2.50). The power of each value of ω_n (for general δ) may then be calculated by

$$|A_n|^2 = \left| \int v_y(x) v_y^{(n)} r(x) \, \mathrm{d}x \right|^2, \tag{2.52}$$

where $r(x)$ is the *weight function*. This weight function is selected so that two solutions $v_y^{(n)}$ and $v_y^{(m)}$ with $m \neq n$ satisfy the orthogonality condition,

$$\left\langle v_y^{(n)}, v_y^{(m)} \right\rangle = \int_{-x_0}^{x_0} v_y^{(n)}(x) v_y^{(m)} r(x) \, \mathrm{d}x = 0. \tag{2.53}$$

Exploitation of such a result allows us to find the coefficients A_n of the series given in Equation (2.50), when the overall perturbation $v_y(x)$ is a known function.

The weight function can be found by re-writing the governing equation in (2.44) in Sturm-Liouville form:

$$\left(v_y'\right)' + \omega^2 r(x) v_y = 0, \tag{2.54}$$

where

$$r(x) = \frac{1}{v_0^2} \frac{\left[\cos\left(\frac{x_0}{H_B}\right)\right]^{(\delta-2)}}{\left[\cos\left(\frac{x}{H_B}\right)\right]^{\delta}}. \tag{2.55}$$

Hence, for any δ, the coefficients A_n may be found.

The normalised power against the frequencies ω_n as defined in Equation (2.52) for $\delta = 0$ (blue), $\delta = 0.5$ (red) and $\delta = 2$ (yellow), and the same parameter values as in Figure 2.6 is illustrated in Figure 2.9. The power for $\delta = 0$ is highest for infinitesimal frequencies, becoming close to zero for frequencies $4Hz$ and larger. Since the eigenfrequencies are defined by

$$\omega_n = k_x^{(n)} v_0 \cos\left(\frac{x_0}{H_B}\right), \tag{2.56}$$

the smaller the wavenumber $k_x^{(n)}$, the smaller the frequency ω_n, in turn.

As the value of δ increases, it is clear that the power is augmented for higher frequencies, compared to those for $\delta = 0$, especially when $\delta = 2$ where the power only becomes close to zero as the frequency reaches around $6Hz$. Once again, the maximum power is found for infinitesimally small frequencies.

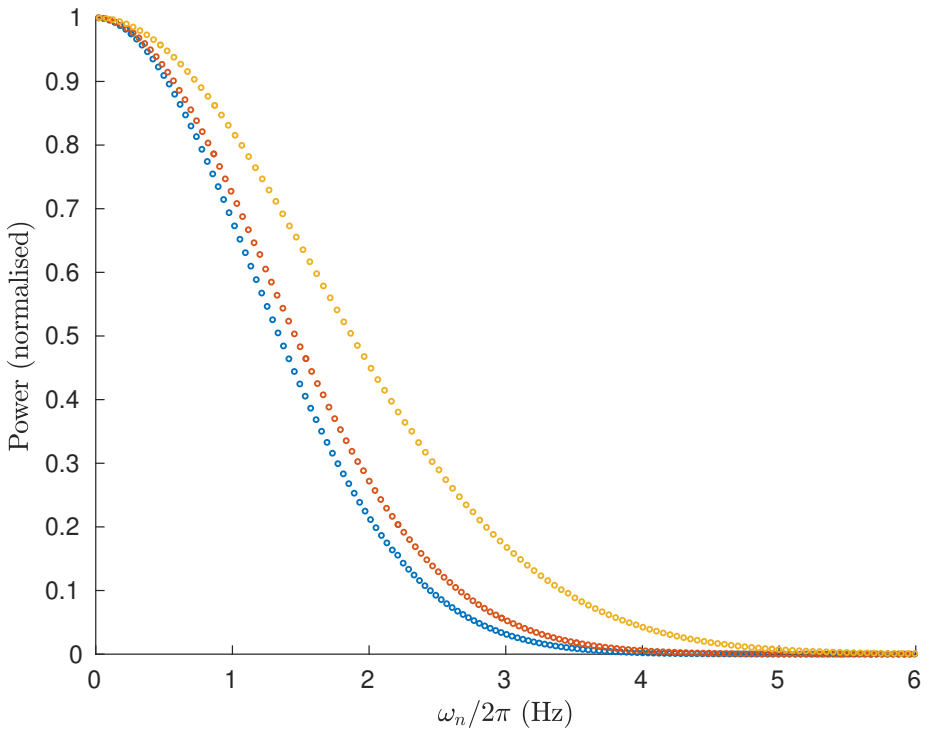

Figure 2.9: The normalised power plotted against eigenfrequencies ω_n in Hz, for $\delta = 0$ (blue), $\delta = 0.5$ (red) and $\delta = 2$ (yellow). Other parameters are the same as in Figure 2.6.

2.5 Normal perturbations: the fast mode

In Section 2.3, the governing equation for perturbation vector $\mathbf{v_1}$ was derived, yielding components perpendicular to field lines (in the $\hat{\mathbf{y}}$ direction), and normal to the magnetic surface prescribed in the ∇A direction, where A is shown in Equation (2.13). The perturbations normal to the surface are denoted by the projection $\mathbf{v_1} \cdot \nabla A$. Taking the scalar product of Equation (2.3) with ∇A, and taking $\mu_0 = 1$ as before,

$$-\omega^2 \rho_0(z) \left(\mathbf{v_1} \cdot \nabla A\right) = \left[\nabla^2 \left(\mathbf{v_1} \cdot \nabla\right)\right] \nabla A \cdot \nabla A \tag{2.57}$$

$$\implies \quad -\omega^2 \rho_0(z) \left(\mathbf{v_1} \cdot \nabla A\right) = \left[\nabla^2 \left(\mathbf{v_1} \cdot \nabla\right)\right] B_0^2(z). \tag{2.58}$$

Finding a solution for $\mathbf{v_1} \cdot \nabla A$, in the case where we have a low plasma-β value (such as in the corona), gives a fast mode. Such a solution may be found using separation of variables, i.e.

$$\mathbf{v_1} \cdot \nabla A = \tilde{X}(x)\tilde{Z}(z). \tag{2.59}$$

Substituting the expression in (2.59) into Equation (2.58),

$$-\rho_0(z)\omega^2 \tilde{X}(x)\tilde{Z}(z) = B_0^2(z)\nabla^2 \left(\tilde{X}(x)\tilde{Z}(z)\right) \tag{2.60}$$

$$\implies \quad -\rho_0(z)\omega^2 \tilde{X}(x)\tilde{Z}(z) = B_0^2(z) \left(\tilde{X}''(x)\tilde{Z}(z) + \tilde{X}(x)\tilde{Z}''(z)\right) \tag{2.61}$$

$$\implies \quad -\frac{\rho_0(z)\omega^2}{B_0^2(z)} = \frac{\tilde{X}''}{\tilde{X}} + \frac{\tilde{Z}''}{\tilde{Z}} \tag{2.62}$$

$$\implies \quad \frac{\tilde{X}''}{\tilde{X}} = -\frac{\rho_0(z)\omega^2}{B_0^2(z)} - \frac{\tilde{Z}''}{\tilde{Z}} = -k_x^2, \tag{2.63}$$

so that the choice of k_x^2 (a real constant) satisfies the following boundary conditions: assume that the perturbation goes to zero at the edges of the arcade i.e. for $x = \pm l$, where l is the half-width of the arcade, for some height of the arcade $z = h$, and at the footpoints of the arcade $z = 0$, so that the line-tying condition is satisfied.

Thus, the left hand side of Equation (2.63) may be rearranged to give the second order ordinary differential equation

$$\tilde{X}'' + k_x^2 \tilde{X} = 0, \tag{2.64}$$

with the solution

$$\tilde{X}(x) = \begin{cases} A\cos(k_x x) \\ B\sin(k_x x) \end{cases}, \tag{2.65}$$

with the choice of either solution once again dependent on the choice of an odd or even function. We restrict our analysis to only the even eigenfunctions, as in the Alfvén mode case, so that we may once again investigate an initial perturbation.

Applying the boundary conditions at each of the arbitrary footpoints gives the value of k_x:

$$k_x^{(n)} = \frac{(n+\frac{1}{2})\pi}{x_0}, \quad \text{for} \quad v_y = A\cos(k_x x), \quad n = 0, 1, 2, ... \tag{2.66}$$

$$k_x^{(m)} = \frac{m\pi}{x_0}, \quad \text{for} \quad v_y = A\sin(k_x x), \quad m = 1, 2, 3, ... \tag{2.67}$$

Equation (2.63) also provides the differential equation in z:

$$\tilde{Z}'' + \left[\frac{\omega^2\rho_0(z)}{B_0^2(z)} - k_x^2\right]\tilde{Z} = 0 \tag{2.68}$$

$$\implies \tilde{Z}'' + \left[\frac{\omega^2\rho_0(z)}{B_0^2} e^{\frac{2z}{H_B}} - k_x^2\right]\tilde{Z} = 0 \tag{2.69}$$

$$\implies \tilde{Z}'' + \left[\frac{\omega^2\rho_0}{B_0^2} e^{-\left(\frac{z}{H} - \frac{2z}{H_B}\right)} - k_x^2\right]\tilde{Z} = 0 \tag{2.70}$$

$$\implies \tilde{Z}'' + \left[\frac{\omega^2}{v_0^2} e^{-(\delta-2)\frac{z}{H_B}} - k_x^2\right]\tilde{Z} = 0. \tag{2.71}$$

If $\delta = 2$, the equation is reduced to a second order ordinary differential equation with constant coefficients, which may be solved dependent on some wavenumber $k_z = \sqrt{\frac{\omega^2}{v_0^2} - k_x^2}$:

$$\tilde{Z}'' + k_z^2\tilde{Z} = 0. \tag{2.72}$$

Hence, adhering to the line-tying boundary conditions (i.e. $\tilde{Z}(0) = 0$) and allowing the perturbation to vanish at some arcade height h (i.e. $\tilde{Z}(h) = 0$), a sinusoidal solution is obtained:

$$\tilde{Z}(z) = K\sin(k_z z), \tag{2.73}$$

where

$$k_z^{(\tilde{n})} = \frac{\tilde{n}\pi}{h}, \quad \tilde{n} = 1, 2, 3, ... \tag{2.74}$$

More generally, when $\delta \neq 2$, the equation is best solved with a change of

variable: Let $\xi(z) = \frac{2H_B\omega}{|\delta-2|v_0}e^{-(\delta-2)\frac{z}{2H_B}}$. By the chain rule,

$$\frac{\mathrm{d}^2\tilde{Z}}{\mathrm{d}z^2} = \frac{\mathrm{d}}{\mathrm{d}z}\left(\frac{\mathrm{d}\tilde{Z}}{\mathrm{d}\xi}\frac{\mathrm{d}\xi}{\mathrm{d}z}\right) \tag{2.75}$$

$$= \left[\frac{\mathrm{d}}{\mathrm{d}z}\left(\frac{\mathrm{d}\tilde{Z}}{\mathrm{d}\xi}\right)\frac{\mathrm{d}\xi}{\mathrm{d}z} + \frac{\mathrm{d}\tilde{Z}}{\mathrm{d}\xi}\frac{\mathrm{d}^2\xi}{\mathrm{d}z^2}\right] \tag{2.76}$$

$$= -\frac{(\delta-2)^2}{4H_B^2}\xi^2\frac{\mathrm{d}^2\tilde{Z}}{\mathrm{d}\xi^2} + \frac{(\delta-2)^2}{4H_B^2}\xi\frac{\mathrm{d}\tilde{Z}}{\mathrm{d}\xi}. \tag{2.77}$$

The governing equation in (2.71) may then be written in terms of $\xi(z)$:

$$-\frac{(\delta-2)^2}{4H_B^2}\xi^2\frac{\mathrm{d}^2\tilde{Z}}{\mathrm{d}\xi^2} + \frac{(\delta-2)^2}{4H_B^2}\xi\frac{\mathrm{d}\tilde{Z}}{\mathrm{d}\xi} + \left[\frac{(\delta-2)^2}{4H_B^2}\xi^2 - k_x^2\right]\tilde{Z} = 0 \tag{2.78}$$

$$\implies \xi^2\frac{\mathrm{d}^2\tilde{Z}}{\mathrm{d}\xi^2} + \xi\frac{\mathrm{d}\tilde{Z}}{\mathrm{d}\xi} + \left[\xi^2 - \frac{4k_x^2H_B^2}{(\delta-2)^2}\right]\tilde{Z} = 0 \tag{2.79}$$

$$\implies \xi\frac{\mathrm{d}}{\mathrm{d}\xi}\left(\xi\frac{\mathrm{d}\tilde{Z}}{\mathrm{d}\xi}\right) + \left[\xi^2 - \lambda^2\right]\tilde{Z} = 0, \tag{2.80}$$

where $\lambda = \frac{2k_xH_B}{|\delta-2|}$. Hence, the equation has been transformed into the Bessel equation of order λ, with solutions of the form

$$\tilde{Z}(\xi) = \alpha J_\lambda(\xi) + \beta Y_\lambda(\xi) \tag{2.81}$$

for $\delta \neq 2$, where J and Y are Bessel functions of the first and second kind, respectively.

The boundary conditions for $\tilde{Z}(z)$ must also be rewritten in terms of the new variable, ξ. When $z = 0$, i.e. at the bottom of the arcade, $\xi = \xi_0 = \frac{2H_B\omega}{|\delta-2|v_0}$. At the top of the arcade, $z = h$ and $\xi = \xi_h = \frac{2H_B\omega}{|\delta-2|v_0}e^{-(\delta-2)\frac{h}{2H_B}}$. Thus, if δ is sufficiently large, the value of ξ_h gets close to zero, and the solution in (2.81) cannot be evaluated.

These conditions mean that the coefficients may be written in terms of each other in a system of two equations, and a dispersion relation between k_x and ω may be formed as:

$$J_\lambda(\xi_0)Y_\lambda(\xi_h) = J_\lambda(\xi_h)Y_\lambda(\xi_0). \tag{2.82}$$

Finally, the general solution of Equation (2.58) may be written in terms of an even perturbation in x and Bessel functions in z:

$$\mathbf{v_1}\cdot\nabla A(x,z) = \sum_{n=0}^{\infty}\sum_{m=0}^{\infty} A_n\cos(k_x^{(n)}x)\left[J_{\lambda_n}(\xi_m) - \frac{J_{\lambda_n}(\xi_0^{(m)})}{Y_{\lambda_n}(\xi_0^{(m)})}Y_{\lambda_n}(\xi_m)\right], \tag{2.83}$$

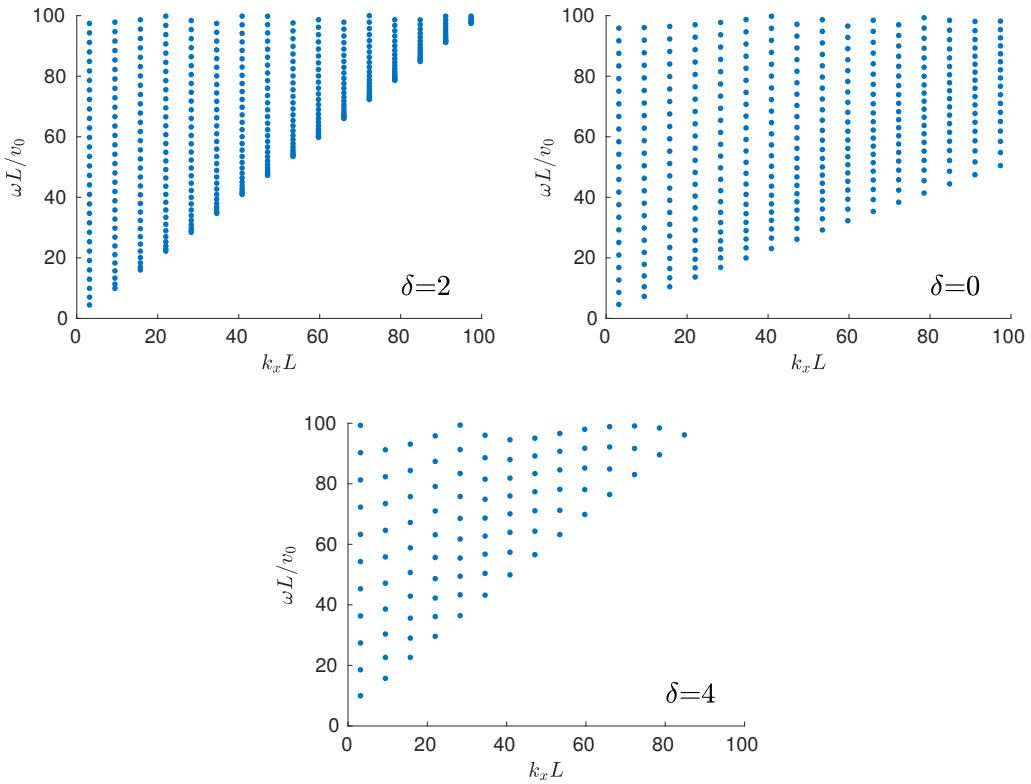

Figure 2.10: Propagation diagrams of normalised eigenfrequencies $\frac{\omega L}{v_0}$ against normalised wavenumbers $k_x L$, for $\delta = 0$ (left), 2 (middle) and 4 (right). The magnetic scale height is, as before, $H_B = 11.66Mm$, and the Alfvén speed at the footpoints is $v_0 = 1Mm$. The height of the loop apex is assumed to be equal to l.

where

$$\xi_m(z) = \frac{2H_B\omega_m}{|\delta-2|v_0}e^{-(\delta-2)\frac{z}{2H_B}}, \quad \xi_0^{(m)} = \frac{2H_B\omega_m}{|\delta-2|v_0} \quad \text{and} \quad \lambda_n = \frac{2k_x^{(n)}H_B}{|\delta-2|}. \tag{2.84}$$

Using the dispersion relation given in Equation (2.82), we may find the resultant propagation diagrams, and hence fast mode solutions, given specific parameters such as arcade width, height and footpoint Alfvén speed. This is accomplished in the next section.

2.5.1 Propagation diagrams and eigenfunctions

The propagation diagrams of normalised eigenfrequency $\frac{\omega L}{v_0}$ against normalised wavenumber $k_x L$ for each δ may be computed, as shown in Figure 2.10, for the same arcade parameters as in Section 2.4. We plot for $\delta = 0$ (top left), $\delta = 2$ (top right), and $\delta = 4$ (bottom). In the case where $\delta = 2$, the relation

$k_z = \sqrt{\frac{\omega^2}{v_0^2} - k_x^2}$ can be employed, and the definitions of the wavenumbers in Equations (2.66) and (2.74) to find each eigenfrequency ω_m. When $\delta \neq 2$, we rely on the dispersion relation given in Equation (2.82).

It is clear that as δ is increased, the number of eigenfrequencies and wavenumbers allowed by the solution first increases (up to $\delta = 2$), and thereafter decreases. The points appear to follow a more linear trend for the $\delta = 0$ case, for low eigenfrequencies, whilst for $\delta = 2$ and 4, the points appear to follow curved trajectories as the wavenumber is increased from 0. In all three cases, the point trajectories become more curved for higher eigenfrequencies. From the propagation diagrams, the first three normalised eigensolutions $\mathbf{v} \cdot \nabla A$ for the first three wavenumbers are plotted against spatial components x and z for the δ values as in Figure 2.10, and the same parameter values (see Figures 2.11, 2.12 and 2.13).

As previously discussed, the corona is perhaps best approximated for $\delta = 0$, which is shown in Figure 2.11. The top panel shows the first wavenumber k_x, the middle the second, and the bottom the third. The columns then represent the first (left), second (middle) and third (right) eigenfunctions for each wavenumber. It is clear each of the velocities becomes negligible for $z \to 0$ (i.e. close to the photosphere). As the wavenumber k_x is increased, the eigenfunctions become oscillatory in nature as z grows larger, but the magnitude of the velocity in each case dampens. In the x-direction, eigenfunction is increased, the number of peaks and troughs increases, but the magnitudes of these do not increase or decrease. Hence, we have spatial oscillations occurring both in height and across the width of the arcade.

When the scale heights match (i.e. $\delta = 2$), the velocity becomes purely oscillatory in both the x and z directions (i.e. both in height and width), with the maximum amplitude of the perturbations remaining the same in the x and z directions (Figure 2.12). Finally, increasing the ratio δ to 4 yields velocity perturbations which appear to diverge as z increases in height (Figure 2.13). However, since we assumed that the perturbations tend to zero for some arcade height, the energy density in the system remains finite. If the height of the arcade tended to infinity, the oscillation amplitude would also increase to infinity.

2.5.2 Effect of a density discontinuity

Even within the many layers of the Sun, variation in density occurs at finite scales, with drastic implications on the wave modes present. To illustrate this,

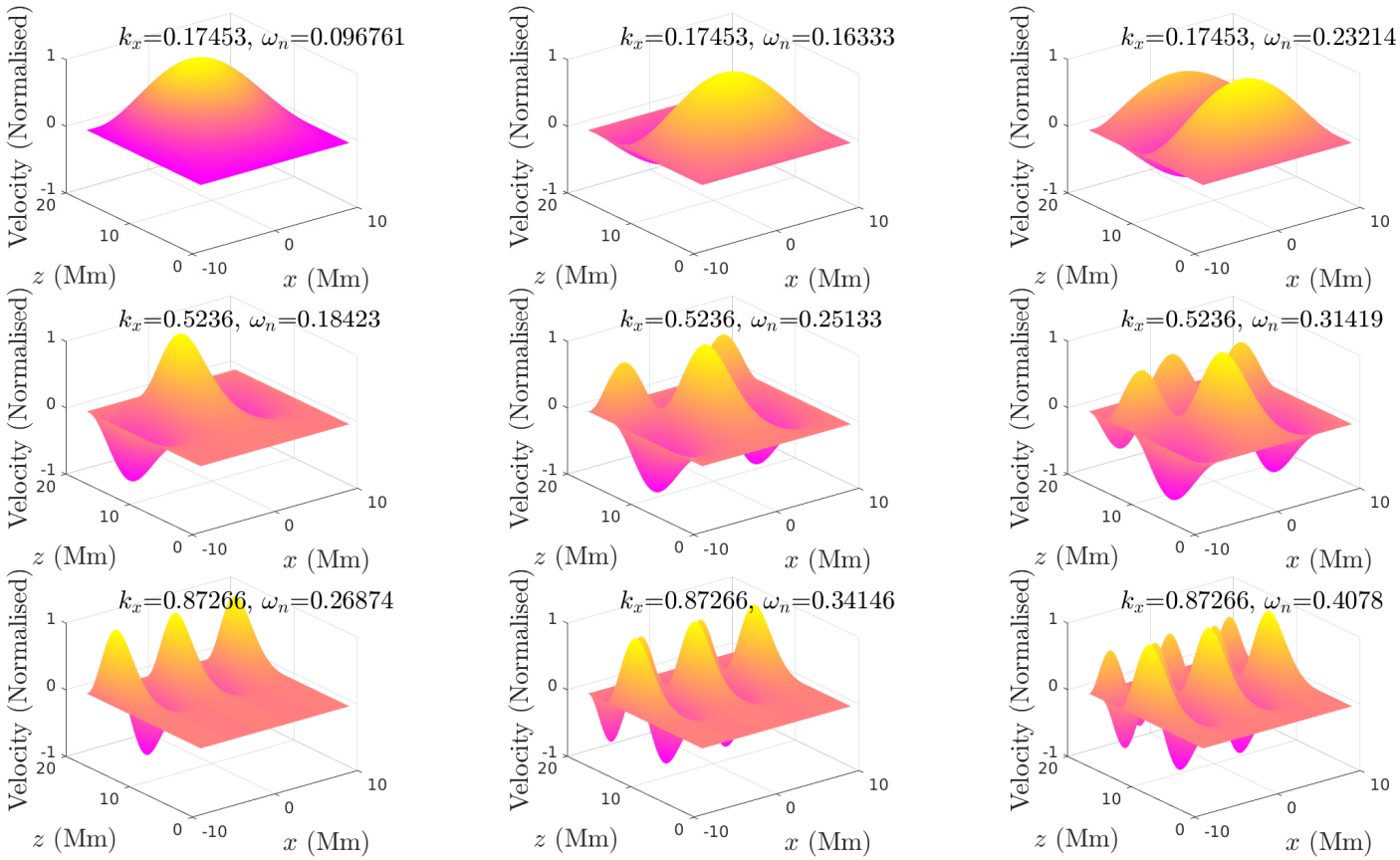

Figure 2.11: The first three normalised velocity eigenfunctions $\mathbf{v} \cdot \nabla A$, normal to the magnetic surfaces, plotted against the x and z spatial components, for the first wavenumber k_x, and for $\delta = 0$. The magnetic scale height, arcade width, and Alfvén speed are the same as in Figure 2.10.

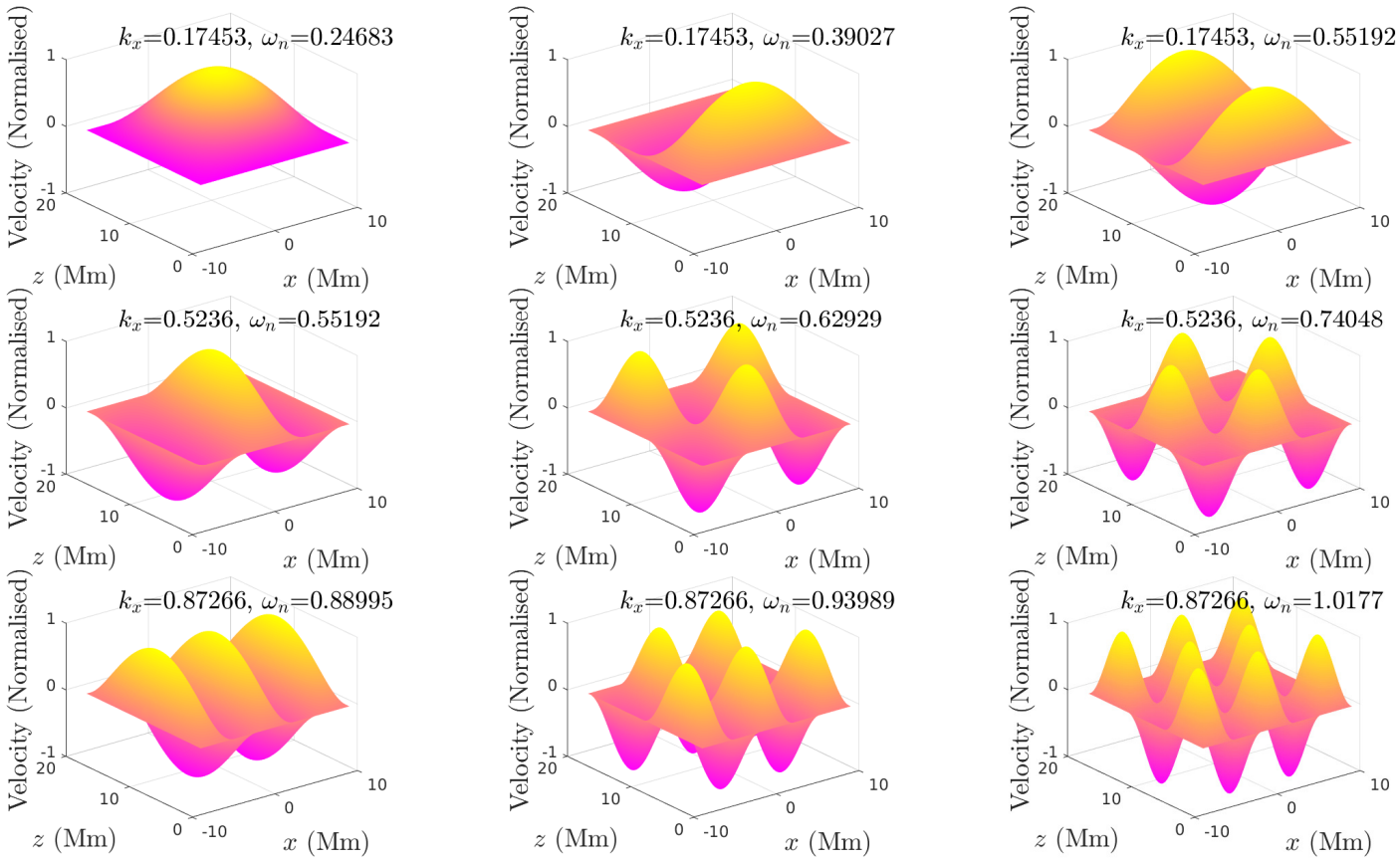

Figure 2.12: The first three normalised velocity eigenfunctions $\mathbf{v} \cdot \nabla A$, as in Figure 2.11, for $\delta = 2$.

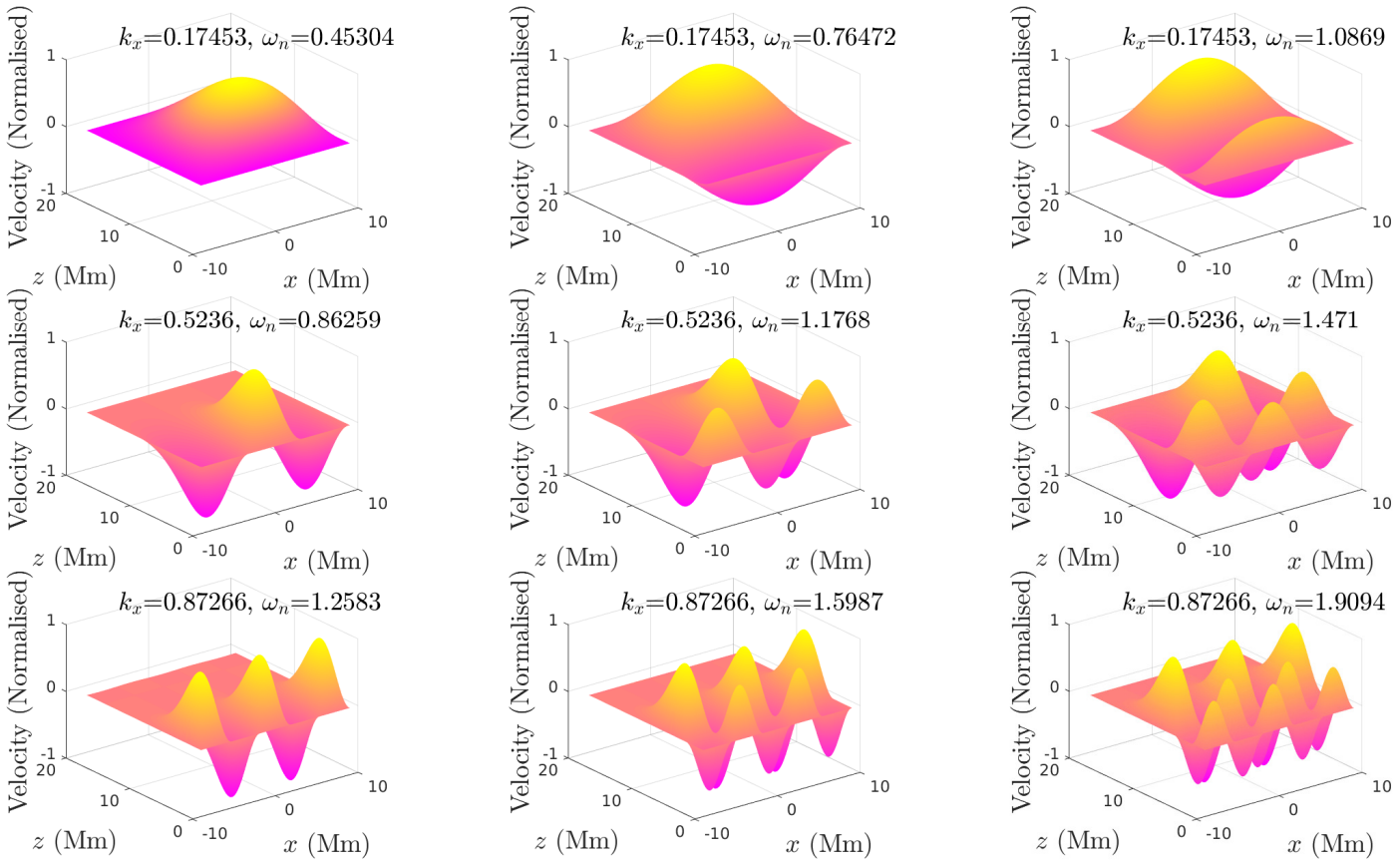

Figure 2.13: The first three normalised velocity eigenfunctions $\mathbf{v} \cdot \nabla A$, as in Figure 2.11, for $\delta = 4$.

a contrast in density is proposed, to model the effect of changes to density structure on the resultant eigenfunctions. Recall that the Alfvén speed is assumed to be of the form

$$v_A(z) = \sqrt{\frac{B_0^2 e^{-\frac{(2-\delta)z}{H_B}}}{\rho_0}} \tag{2.85}$$

$$= v_0 e^{-\frac{(2-\delta)z}{2H_B}}, \tag{2.86}$$

where v_0 is then the Alfvén speed at the footpoints of the coronal loop structure ($z = 0$). Now, assume that the Alfvén speed may be modelled with respect to height as follows:

$$v_A(z) = \begin{cases} v_0 e^{-\frac{(2-\delta)z}{2H_B}} & \text{if } z < z_0 \\ v_1 e^{-\frac{(2-\delta)z}{2H_B}} & \text{if } z > z_0, \end{cases} \tag{2.87}$$

where v_1 may be chosen as $v_1 \neq v_0$. Keeping the magnetic field profile the same as in Equation (2.14), a contrast in density is formed at $z = z_0$ whenever v_1 and v_0 differ. We examine two cases: where the density contrast is formed close to the footpoints, and when the density contrast further into the arcade.

The top panel of Figure 2.14 shows the first three normalised normal velocities $\mathbf{v_1} \cdot \nabla A$ in the case where the Alfvén speed matches at an interface located at $2Mm$ (which gives the same result as the first row in Figure 2.11). This can be compared to the top and middle panels of Figure 2.14, where the Alfvén speed ratios $\frac{v_1}{v_0}$ at the interface are 0.5 and 0.9, respectively, and for $\delta = 0$.

Though the modes look very similar in all three panels of Figure 2.14, the stark difference is in the eigenfrequencies. Most notably, the eigenfrequencies of the bottom panel of Figure 2.14 (i.e. where the Alfvén speeds match) are around double those in the top panel, that is when $\frac{v_1}{v_0} = 0.5$. Even for a small ratio contrast of 0.9, as in the middle panel of Figure 2.14, the eigenfrequencies are lower than those in the case without a density contrast.

Similarly, we investigate the effect of a discontinuity further from the photosphere. Figure 2.15 show the first three eigenfunctions for the first wavenumber, when the interface is located at $z = 10Mm$, for Alfvén speed contrasts $\frac{v_1}{v_0} = 0.5$ (top) and 0.9 (middle), respectively, where the bottom panels shows the case where there is no contrast, for comparison. Once again, it is clear that a small change to the density contrast, such as in the case $\frac{v_1}{v_0} = 0.9$, can lead to changes in eigenfrequency, and thus leading to uncertainty in parameter prediction when such eigenfunctions are used in conjunction with observational data.

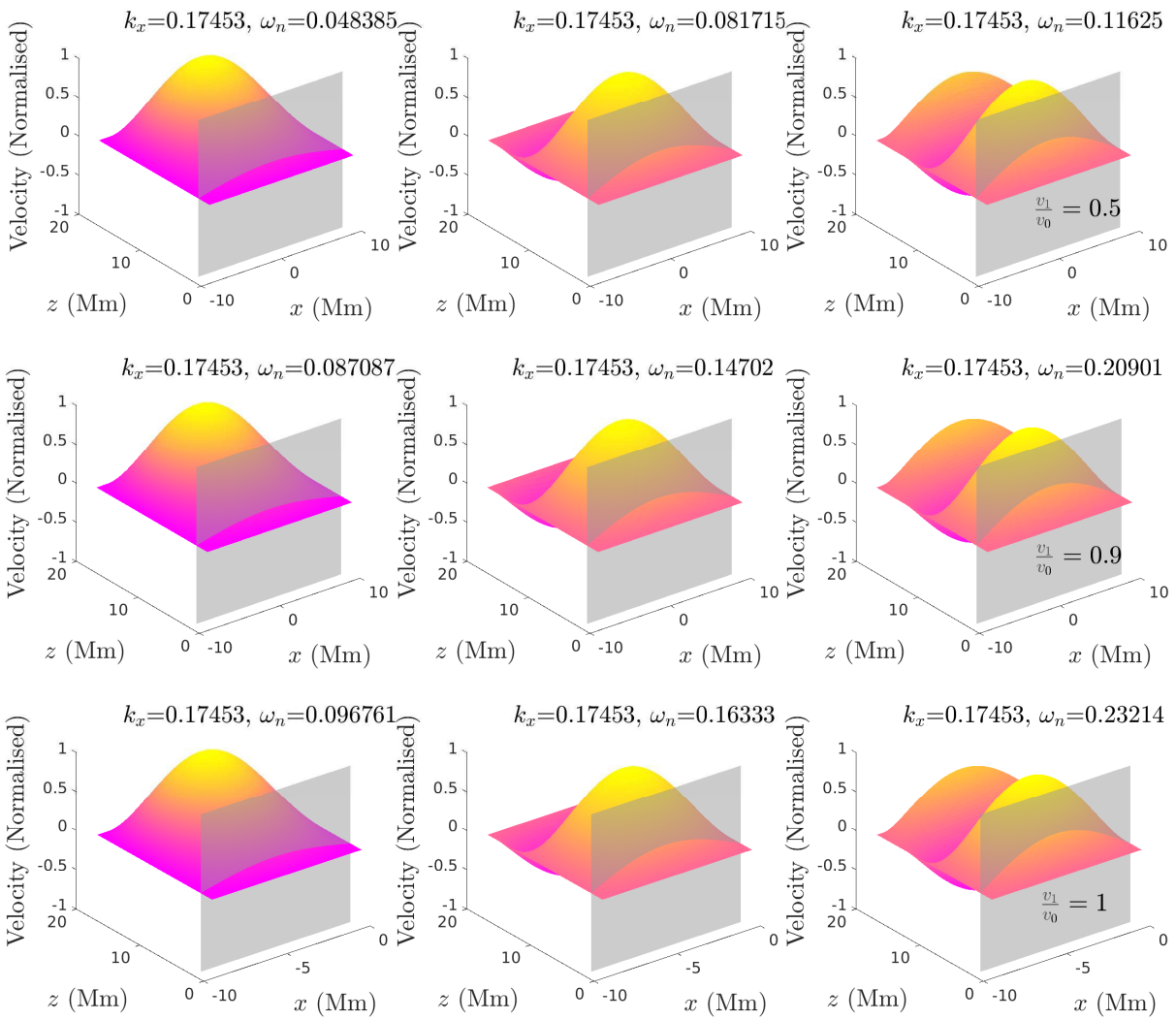

Figure 2.14: The first three normalised velocities $\mathbf{v_1} \cdot \nabla A$ plotted against the width x and height z, both in Mm, for the first wavenumber k_x, in the case where the Alfvén speed at the interface, located at height $z = 2Mm$, is such that their ratio $\frac{v_1}{v_0} = 0.5$ (top), 0.9 (middle), and 1 (bottom). All other parameters match as in Figure 2.11.

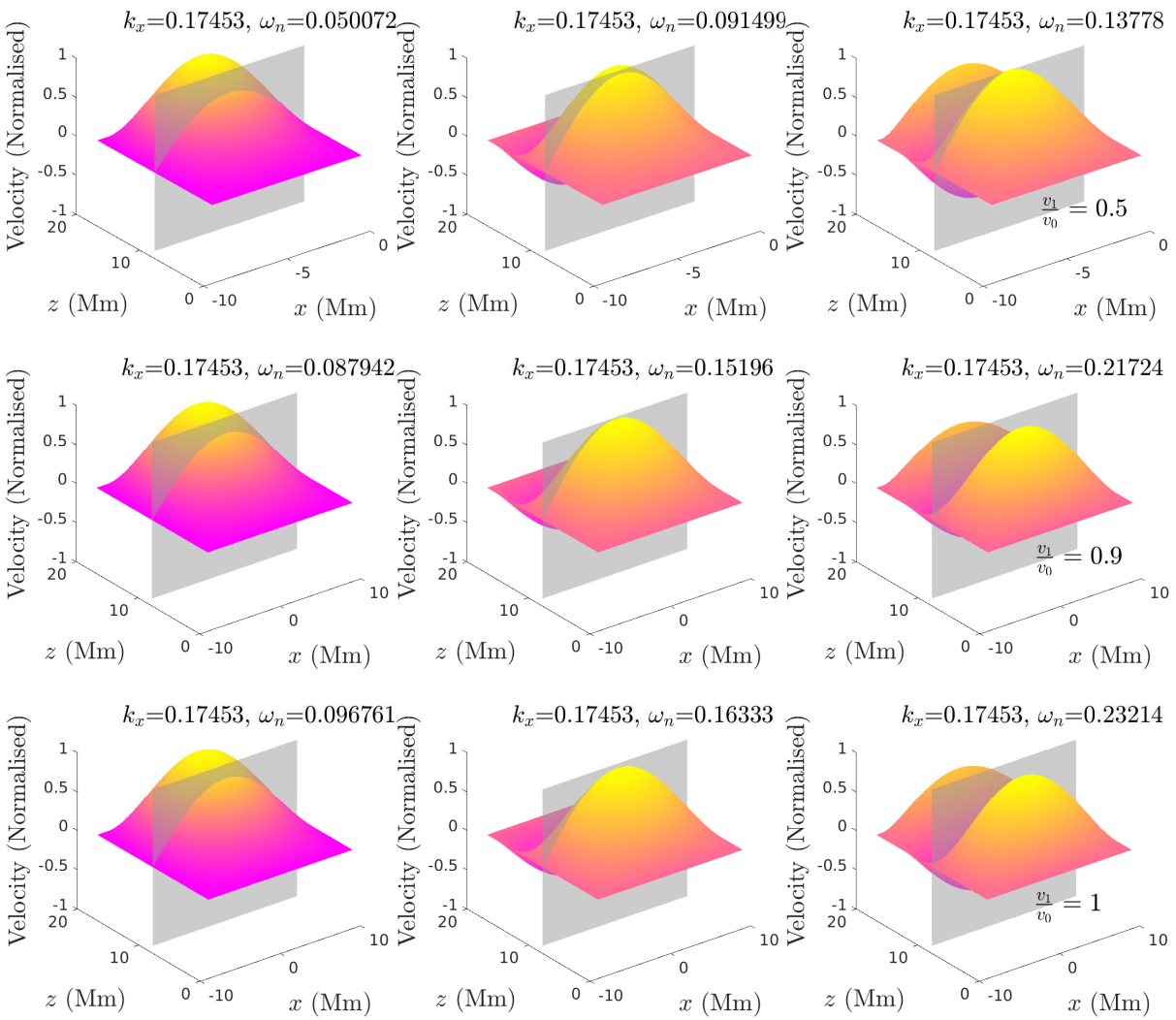

Figure 2.15: The first three normalised velocities $\mathbf{v_1} \cdot \nabla A$ plotted against the width x and height z, both in Mm, for the first wavenumber k_x, in the case where the Alfvén speed at the interface, located at height $z = 10Mm$, is such that their ratio $\frac{v_1}{v_0} = 0.5$ (top), 0.9 (middle), and 1 (bottom). All other parameters match as in Figure 2.11.

This effect has significant observational implications — waves can be used diagnostically to determine parameters which cannot be directly observed, such as information pertaining to the magnetic field structures and densities of surrounding plasma. Hence, depending on the choice of Alfvén speed profile (and hence density profile), observations of certain frequencies in two different oscillating coronal loop structures may indicate the presence of vastly different modes. Subsequently, there may be an unreliable diagnosis, through inversions using the same reference model, of the structures residing in the observations (see Jain and Hindman (2012)).

2.5.3 Excitation of fast modes

Much as in Section 2.4.4, the existence of modes in the presence of a perturbation may be investigated. Here, a Gaussian excitation as a function of x and z, such that the perturbation is concentrated at the centre of the loops of height $z = h$, is projected onto the fast mode solution as in Equation (2.5), such that

$$e^{-\frac{x^2+(z-h)^2}{2w^2}} \propto \sum_{n=0}^{\infty}\sum_{m=0}^{\infty} A_{n,m}\cos(k_x^{(n)}x)\left[J_{\lambda_n}(\xi_m) - \frac{J_{\lambda_n}(\xi_0^{(m)})}{Y_{\lambda_n}(\xi_0^{(m)})}Y_{\lambda_n}(\xi_m)\right], \quad (2.88)$$

where w is some characteristic length, and $\xi_m(z)$, $\xi_0^{(m)}$ and λ_n defined as before in Section 2.5: where $\xi_m(z) = \frac{2H_B\omega_m}{|\delta-2|v_0}e^{-(\delta-2)\frac{z}{2H_B}}$, $\xi_0^{(m)} = \frac{2H_B\omega_m}{|\delta-2|v_0}$ and $\lambda_n = \frac{2k_x^{(n)}H_B}{|\delta-2|}$. The coefficients $A_{n,m}$ may then be extracted from the summation using orthogonality. However, an analytically (or, indeed, numerically) orthogonal function corresponding to the right hand side may only be found for $\delta = 2$. This value of δ reduces the eigenfunction as in Equation (2.73), such that

$$A_{n,m} \propto \int\int e^{-\frac{x^2+(z-h)^2}{2w^2}}\cos(k_x^{(n)}x)\sin\left(\sqrt{k_x^{(n)} - \omega_m^2}z\right)\,\mathrm{d}x\mathrm{d}z. \quad (2.89)$$

The normalised power spectrum and the corresponding eigenfrequencies are plotted in Figure 2.16, for the same parameters as in Figure 2.9.

As in the Alfvén mode case, the normalised power spectrum exhibits a maximum for infinitesimally small frequencies. The amplitudes of these spectra decrease for increasing ω_m, with an almost linear trend between $1-2.5Hz$. The rate of change in amplitude slows beyond this point, with frequencies higher than around $5 - 5.5Hz$ contributing very minimally to the power in the fast wave solutions.

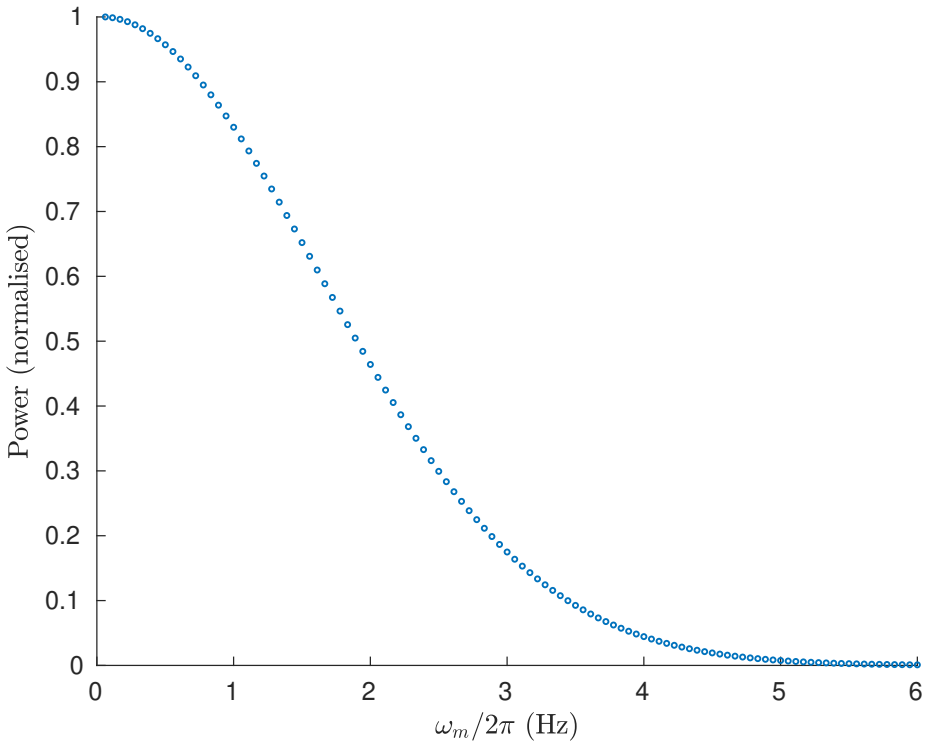

Figure 2.16: The normalised power plotted against eigenfrequencies ω_m in Hz for $\delta = 0$. Once again, the footpoints are situated at $l = \pm 18Mm$. The magnetic scale height is, as before, $H_B = 11.66Mm$, and the Alfvén speed at the footpoints is $v_0 = 1Mm$. The height of the loop apex is assumed to be equal to l.

2.6 Summary

A solar coronal arcade model in Cartesian coordinates was introduced following Oliver *et al.* (1993), and subsequently Alfvén and fast mode solutions obtained (Sections 2.2 and 2.3). For the same model, Tarr (2017) extended the Alfvén mode case under the assumption that the gas pressure scale height far exceeds the magnetic pressure scale height i.e. that gravity has little influence. For this value of $\delta = 0$, a parameter describing the ratio of the magnetic pressure scale height to the gas pressure scale height, the governing equation for the Alfvén wave solutions could be solved analytically (Section 2.4). We have extended Tarr (2017) to general δ, requiring the governing equation for Alfvén modes to be solved numerically (Sections 2.4.2 and 2.4.3). From these solutions, the existence of modes for several values of δ were examined, and the power as a function of frequency for a given initial perturbation as in Tarr (2017) calculated (Section 2.4.4). Similarly, eigensolutions for the fast mode were obtained using numerical methods for general δ (Section 2.5), and also in the presence of density interface close to the footpoints. Finally, power spectra given a slightly modified excitation (Section 2.5.3) were studied for large pressure scale height.

Section 2.5.1 revealed that approximations in the corona may lead to the choice of small δ, since magnetic pressure is thought to dominate over the gas pressure of the environment. However, even for values of δ between 0 and 2, small changes to this parameter affect the amplitudes of Alfvén oscillations away from the apex of the loop arcade (see Figures 2.7 and 2.8). This was further iterated in Section 2.9, where amplitudes of power spectra given a push from an initial perturbation are calculated, shown in Figure 2.9. As the value of δ is increased from 0 to 2, the amplitudes become diminished as the frequency increases. All δ values have infinitesimally small powers for higher frequencies.

By investigating the fast mode (or normal) perturbations, Section 2.5 saw the governing equation solved numerically for different values of δ. There, small changes to the value of δ shifted the corresponding eigenfrequencies, causing the resulting eigenfunctions to change drastically. The same effect was produced when considering a region of differing density at two different heights in the loop arcade: though the effect was not as pronounced, even small changes to the density structure offered different eigenfrequencies. Imposing an excitation at the loop tops gave rise to power spectral data, but this could only be

calculated (numerically, or otherwise) for one value: $\delta = 2$, that is, where the magnetic pressure scale height and the gas pressure scale heights were equal. It is, perhaps, necessary here to discuss the fast modes in comparison with those in models previously covered in literature. In Section 2.1, it was noted that Van Doorsselaere *et al.* (2009) investigated the effects of curvature on the resulting modes. For a constant Alfvén frequency, the oscillation polarisation varied, and could be either vertically or horizontally polarised (to be determined observationally), though did not affect the fast mode beyond this. However, for other (non-constant) Alfvén frequencies, the curvature introduced leakage in the waves. A more in-depth analysis of curvature using a 2D semi-cylindrical model was conducted by Díaz *et al.* (2006). There, the fast and Alfvén modes were be decoupled, and only the fast mode examined. The fast mode solution was determined to be leaky in certain limits of the arcade width, echoing that of the straight slab in Edwin and Roberts (1982), whilst becoming trapped for others. However, the curvature of the arcade brought differences in the density perturbations produced, allowing the apex of the curved slab to move upwards more quickly than the footpoints. Though this cannot be directly compared to the model in this Chapter, it must be noted that for values δ approximating the solar corona (i.e. for δ values between 0 and 2), the fast mode amplitudes decrease exponentially away from the arcade.

Note that Hindman and Jain (2014) studied the excitation of fast MHD waves in two-dimensional waveguides for similar magnetic field profiles in a Cartesian coordinate system for the $\delta = 0$ case. They considered two different excitation signals: one a strong localised source, and the other a continuous, stochastic source with and without a Gaussian profile in wavenumbers. They found that waves triggered by flaring events and oscillations known as "decayless" were likely associated with fast MHD modes, and their existence was dependent on the type of excitation. It is interesting that in Hindman and Jain (2014), in duality with the power spectrum results of this Chapter, the lowest eigenfrequencies were dominant, with higher frequencies contributing very little to the overall velocity perturbations. Furthermore, they discussed the necessity of a waveguide that was at least two-dimensional, with modes trapped radially, but also propagating down the arcade axis, across field lines in a perpendicular motion. We cover one such waveguide in the next Chapter.

In both the Alfvén and fast mode cases, changes to the parameter δ caused the resultant eigenfunctions to change shape, and often resulted in significantly different behaviour. Additionally, changes to the density profile in the fast

mode case altered eigenfrequencies. Since wave properties may be used to deduce other plasma and magnetic field parameters (Aschwanden *et al.* (1999); Nakariakov (1999)), this may have large effects on estimations of the solar coronal structure. This is particularly true for Section 2.5.2, as the plasma density will rarely be stratified in such a manner that the density will increase smoothly from the photosphere outwards. In fact, it may be that there are many different density interfaces as the loops stretch upwards, causing complex cavities for the waves to traverse. Hence, careful determination of parameters in the model is a necessity, particularly if the analysis is to be used in the context of coronal heating. This will be explored in more detail in the next Chapter.

CHAPTER 3

A solar coronal arcade in cylindrical coordinates

3.1 Introduction

The solar corona is believed to have decreasing plasma density with height (Melrose (1980)). However, at finer scales brighter structures stand out against their background, which may be due to temperature or density differences. Historically, determining the density structures in the solar corona has proved to be difficult. More specifically, though it is generally believed that loops are denser than their surroundings, observations in particular EUV wavelengths have shown cooler loops as darker in comparison to the background, and loops which are apparently brighter may be lower in density than expected. Thus, it is important to perform analysis in multiple wavelengths, to ascertain a more accurate estimate to the density or temperature distribution (Aschwanden (2005)).

Observations prove an extremely useful tool for indirectly deriving parameters such as the magnetic field strength or density, as discussed in Section 1.4.1, in conjunction with mathematical modelling. However, in Section 2.1, we saw that most models of coronal loop structures may be reduced to seeking oscillations in 1D wave cavities. However, extending this to 3D models has become increasingly more common, with such an MHD model implemented in Ofman *et al.* (2015), to better explain vertically polarised transverse waves. Additionally, observations have shown oscillations in multiple loops in the same arcade at the same time (see Jain, Maurya and Hindman (2015); Li *et al.* (2017)).

This chapter is based on the following refereed journal article:

- Thackray, H., Jain, R. (2017); Fast magnetohydrodynamic waves in a solar coronal arcade, *Astron. Astrophys.*, Volume 608, A108

Hindman and Jain (2014) (see also Hindman and Jain (2015)) discussed the necessity for 2D or 3D modelling of coronal loop arcade. There, they showed that the strongly magnetised low plasma-β environment mean that eruptive events (such as flares) stimulate the field lines easily, transmitting fast MHD modes. Waves propagating down the waveguide interfere with one another, creating a rich power spectrum, and supplying information about feasible wavenumbers and periodicities. Thus, properties pertaining to the magnetic field, density and waveguide may be estimated. Furthermore, they highlighted the importance and interaction between both magnetic tension and magnetic pressure, rather than just the magnetic tension in 1D wave problems.

More specifically, in Hindman and Jain (2015), by construction of a 3D wave cavity in cylindrical coordinates, propagation of fast MHD waves was investigated. A two-shell model was proposed, with a sharp density increase at an interface. Holding the axial direction of the magnetic field invariant, trapped waves in both the azimuthal and radial directions can exist. As a result, coupled radial and axial modes were accredited to observations of loop oscillations in differing lines-of-sight, producing both horizonally and vertically polarised waves, and demonstrating the variation of elliptically polarised modes in loop height. However, the introduction of the sharp density interface, resident to the oscillations in the system, when replaced with a smooth and continuous density structure promotes the existence of quasi modes (see Goossens *et al.* (2002)); Ruderman and Roberts (2002)), damping kink mode oscillations due to resonance. However, the discussion of such modes is beyond the scope of this thesis, and instead we limit ourselves to a discontinuous density contrast and study the effects of this on fast eigenfunctions.

In this Chapter, we follow the method of the two-shell model of Hindman and Jain (2015), and solve the governing equations to find eigenfunctions, radial and axial velocities. This model is then extended to a three-shell model, so that the effect of a small inhomogeneous density structure, in addition to a sharp discontinuous density structure, may be investigated, and the resultant fast mode solutions produced are compared with that of the two-shell model. The intermediate shell here illustrates the region where a loop of higher or lower density than the background may reside, and therefore the cavity where oscillation have maximum amplitude. In the same manner as Hindman and Jain (2015), a dispersion relation for the wavenumbers and eigenfrequencies is found, and then solved for differing Alfvén speed profiles, to find eigensolutions, velocities, and thus wave polarisation.

It is worth noting here that Chapter 2 also considered a 3D wave model, though the density structure only varied vertically. In this Chapter, the density is assumed to be varying radially, and therefore more closely resembling the inhomogeneity observed in the solar corona in such coronal loop structures, particularly as the density of loops does not necessarily decrease as we traverse from footpoint to loop apex. Additionally, to ensure the trapping of modes in the radial direction, we will see that it is necessary to choose a discontinuous Alfvén speed profile, with speeds linearly increasing in r on either side of the interface, as in Verwichte *et al.* (2006).

3.2 Geometry of loop arcade

3.2.1 Vector potential, magnetic pressure and magnetic tension

To model the magnetic field in cylindrical coordinates (r, θ, y), we assume that the field lines form semi-circles, with their footpoints penetrating the photosphere, centred on the y-axis. For simplicity, the magnetic field is taken as potential and force-free, in the form

$$\mathbf{B_0} = (0, B(r), 0) = \left(0, \frac{B_0}{r}, 0\right), \tag{3.1}$$

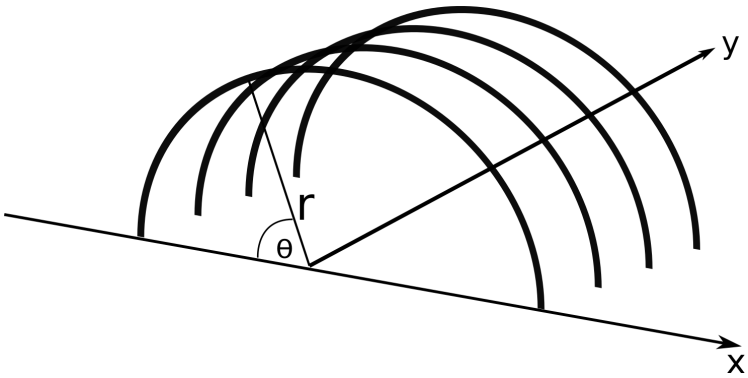

Figure 3.1: The geometry of the field lines in the proposed model, in cylindrical coordinates.

so that the current density, with $\mu_0 = 1$ as the permeability in a vacuum, is

$$\begin{aligned}\mathbf{J_0} &= \nabla \times \mathbf{B_0} && (3.2)\\ &= \nabla \times \left(0, \frac{B_0}{r}, 0\right) && (3.3)\\ &= \frac{1}{r}\frac{\partial}{\partial r}\left(r \cdot \frac{B_0}{r}\right)\hat{\mathbf{y}} && (3.4)\\ &= 0. && (3.5)\end{aligned}$$

Hence, the magnetic field is such that the field strength decreases in the radial direction.

We assume that the equilibrium state is static, such that $\mathbf{v_0} = 0$, and since we also assume that there is no pressure variation or gravity, and that there is time-independence, the momentum equation in the equilibrium has the form

$$\mathbf{J_0} \times \mathbf{B_0} = \mathbf{0}. \tag{3.6}$$

In this way, the effects of a zero-β plasma atmosphere is considered, which models the solar corona suitably.

Following the derivation as in Section 2.3, the governing equation in terms of the perturbed velocity $\mathbf{v_1}$ and the background magnetic field $\mathbf{B_0}$ is

$$\rho_0(r)\frac{\partial^2 \mathbf{v_1}}{\partial t^2} = (\nabla \times (\nabla \times (\mathbf{v_1} \times \mathbf{B_0}))) \times \mathbf{B_0}. \tag{3.7}$$

3.2.2 Introduction of velocity field

Since we assume the plasma to be zero-β, the Lorentz force acts transversely, and thus the perturbations may be assumed to be completely transverse. Hence, we now take a perturbed velocity field of the form

$$\mathbf{v_1} = (v_r, 0, v_y). \tag{3.8}$$

Using (3.1) and (3.8), we can write the $\hat{\mathbf{r}}$ and $\hat{\mathbf{y}}$ components of the momentum Equation (3.7) as

$$\rho_0(r)\frac{\partial^2 v_r}{\partial t^2} = \frac{B_0^2}{r^4}v_r + \frac{B_0^2}{r^2}\frac{\partial^2 v_y}{\partial y \partial r} - \frac{B_0^2}{r^3}\frac{\partial v_r}{\partial r} + \frac{B_0^2}{r^2}\frac{\partial^2 v_r}{\partial r^2} + \frac{B_0^2}{r^4}\frac{\partial^2 v_r}{\partial \theta^2} \tag{3.9}$$

$$\rho_0(r)\frac{\partial^2 v_y}{\partial t^2} = \left(\frac{B_0^2}{r^4}\frac{\partial^2}{\partial \theta^2} + \frac{B_0^2}{r^2}\frac{\partial^2}{\partial y^2}\right)v_y + \left(-\frac{B_0^2}{r^3}\frac{\partial}{\partial y} + \frac{B_0^2}{r^2}\frac{\partial^2}{\partial y \partial r}\right)v_r. \tag{3.10}$$

Introducing the Alfvén speed

$$v_A(r) = \frac{B(r)}{\sqrt{\rho_0(r)}} = \frac{B_0}{r\sqrt{\rho_0(r)}}, \tag{3.11}$$

and fourier-expanding each component $v_{r,y}$ as $u_{r,y}(r)\exp(iky)\sin(m\theta)\exp(-i\omega t)$, Equations (3.9) and (3.10) can be written as

$$-\omega^2 u_r = \frac{(1-m^2)v_A^2}{r^2}u_r + ikv_A^2\frac{\mathrm{d}u_y}{\mathrm{d}r} - \frac{v_A^2}{r}\frac{\mathrm{d}u_r}{\mathrm{d}r} + v_A^2\frac{\mathrm{d}^2u_r}{\mathrm{d}r^2} \tag{3.12}$$

$$-\omega^2 u_y = \left(-\frac{m^2v_A^2}{r^2} - k^2v_A^2\right)u_y + \left(-\frac{ikv_A^2}{r} + ikv_A^2\frac{\mathrm{d}}{\mathrm{d}r}\right)u_r, \tag{3.13}$$

where m is the azimuthal order, k is the axial wavenumber.

3.2.3 Analytic solution

The linearised induction equation is

$$\frac{\partial \mathbf{B_1}}{\partial t} = \nabla \times (\mathbf{v_1} \times \mathbf{B_0}). \tag{3.14}$$

Thus, the $\hat{\boldsymbol{\theta}}$ component is given by

$$\left(\frac{\partial \mathbf{B_1}}{\partial t}\right)_\theta = \frac{\partial(\mathbf{v_1}\times\mathbf{B_0})_r}{\partial y} - \frac{\partial(\mathbf{v_1}\times\mathbf{B_0})_y}{\partial r} \tag{3.15}$$

$$= -\frac{B_0}{r}\frac{\partial v_y}{\partial y} - \frac{B_0}{r}\frac{\partial v_r}{\partial r} + \frac{B_0}{r}\frac{v_r}{r} \tag{3.16}$$

$$= \frac{B_0}{r}\left(-\left(\frac{\partial v_r}{\partial r} + \frac{\partial v_y}{\partial y}\right) + \frac{v_r}{r}\right) \tag{3.17}$$

$$= B(r)\Phi, \tag{3.18}$$

where

$$\Phi = -\left(\frac{\partial v_r}{\partial r} + \frac{\partial v_y}{\partial y}\right) + \frac{v_r}{r}, \tag{3.19}$$

where Φ can be Fourier-analysed as $\phi(r)\exp(iky)\sin(m\theta)\exp(-i\omega t)$.

Taking the derivative of (3.19) with respect to r yields

$$\frac{\partial \Phi}{\partial r} = -\frac{\partial^2 v_r}{\partial r^2} - \frac{\partial^2 v_y}{\partial r \partial y} + \frac{1}{r}\frac{\partial v_r}{\partial r} - \frac{v_r}{r^2}. \tag{3.20}$$

Using (3.20), we can easily see that (3.9) becomes

$$\rho_0(r)\frac{\partial^2 v_r}{\partial t^2} = \frac{B_0^2}{r^4}\frac{\partial^2 v_r}{\partial \theta^2} - \frac{B_0^2}{r^2}\frac{\partial \Phi}{\partial r}. \tag{3.21}$$

Similarly, the derivative of (3.19) with respect to y is

$$\frac{\partial \Phi}{\partial y} = -\frac{\partial^2 v_r}{\partial r \partial y} - \frac{\partial^2 v_y}{\partial y^2} + \frac{1}{r}\frac{\partial v_r}{\partial y}, \tag{3.22}$$

which, with (3.10), yields

$$\rho_0(r)\frac{\partial^2 v_y}{\partial t^2} = \frac{B_0^2}{r^4}\frac{\partial^2 v_y}{\partial \theta^2} + \frac{B_0^2}{r^2}\frac{\partial \Phi}{\partial y}. \tag{3.23}$$

Now, since, as before, we are Fourier-analysing, Equations (3.21) and (3.23) yield

$$-\rho_0(r)\omega^2 u_r = -\frac{m^2 B_0^2}{r^4}u_r - \frac{B_0^2}{r^2}\frac{\mathrm{d}\phi}{\mathrm{d}r} \tag{3.24}$$

$$-\rho_0(r)\omega^2 u_y = -\frac{m^2 B_0^2}{r^4}u_y - \frac{ikB_0^2}{r^2}\phi. \tag{3.25}$$

Using the defition of Alfvén speed in Equation (3.11), coupled with (3.24) and (3.25) gives the equations

$$-\omega^2 u_r = -\frac{m^2 v_A^2}{r^2}u_r - v_A^2\frac{\mathrm{d}\phi}{\mathrm{d}r} \tag{3.26}$$

$$\implies \left(\omega^2 - \frac{m^2 v_A^2}{r^2}\right)u_r = v_A^2\frac{\mathrm{d}\phi}{\mathrm{d}r} \tag{3.27}$$

along with

$$-\omega^2 u_y = -\frac{m^2 v_A^2}{r^2}u_y - ikv_A^2\phi \tag{3.28}$$

$$\implies \left(\omega^2 - \frac{m^2 v_A^2}{r^2}\right)u_y = ikv_A^2\phi. \tag{3.29}$$

We write (3.27) and (3.29) more concisely using vector notation:

$$\left(\omega^2 - \frac{m^2 v_A^2}{r^2}\right)(u_r\hat{\mathbf{r}} + u_y\hat{\mathbf{y}}) = v_A^2\left(\frac{\mathrm{d}\phi}{\mathrm{d}r}\hat{\mathbf{r}} + ik\phi\hat{\mathbf{y}}\right) \tag{3.30}$$

$$\implies (u_r\hat{\mathbf{r}} + u_y\hat{\mathbf{y}}) = \frac{1}{\frac{\omega^2}{v_A^2} - \frac{m^2}{r^2}}\left(\frac{\mathrm{d}\phi}{\mathrm{d}r}\hat{\mathbf{r}} + ik\phi\hat{\mathbf{y}}\right), \tag{3.31}$$

$$\implies \mathbf{v_1} = \frac{1}{\frac{\omega^2}{v_A^2} - \frac{m^2}{r^2}}\left(\frac{\partial \Phi}{\partial r}\hat{\mathbf{r}} + \frac{\partial \Phi}{\partial y}\hat{\mathbf{y}}\right). \tag{3.32}$$

Now, taking the divergence of (3.32), we obtain

$$\nabla\cdot\mathbf{v_1} = \frac{1}{r}\cdot\frac{1}{\Omega^2}\frac{\partial\Phi}{\partial r} - \frac{1}{\Omega^4}\frac{\mathrm{d}(\Omega^2)}{\mathrm{d}r}\frac{\partial\Phi}{\partial r} + \frac{1}{\Omega^2}\frac{\partial^2\Phi}{\partial y^2} + \frac{1}{\Omega^2}\frac{\partial^2\Phi}{\partial r^2}, \tag{3.33}$$

$$\implies \frac{\mathrm{d}u_r}{\mathrm{d}r} + iku_y + \frac{u_r}{r} = \frac{1}{r}\cdot\frac{1}{\Omega^2}\phi' - \frac{1}{\Omega^4}\frac{\mathrm{d}(\Omega^2)}{\mathrm{d}r}\phi' - \frac{k^2}{\Omega^2}\phi + \frac{1}{\Omega^2}\phi'' \tag{3.34}$$

where $\Omega^2 = \frac{\omega^2}{v_A^2} - \frac{m^2}{r^2}$.

However, by (3.19),

$$\Phi = -\left(\nabla \cdot \mathbf{v_1} - \frac{2v_r}{r}\right), \tag{3.35}$$

$$\implies \nabla \cdot \mathbf{v_1} = -\left(\Phi - \frac{2v_r}{r}\right), \tag{3.36}$$

$$\implies \frac{\mathrm{d}u_r}{\mathrm{d}r} + iku_y + \frac{u_r}{r} = -\left(\phi - \frac{2u_r}{r}\right), \tag{3.37}$$

so we can rewrite (3.34) as

$$\phi = -\frac{1}{r}\cdot\frac{1}{\Omega^2}\phi' + \frac{1}{\Omega^4}\frac{\mathrm{d}(\Omega^2)}{\mathrm{d}r}\phi' + \frac{k^2}{\Omega^2}\phi - \frac{1}{\Omega^2}\phi'' + \frac{2}{r}\cdot\frac{1}{\Omega^2}\phi' \tag{3.38}$$

$$\implies \phi'' - \left[\frac{1}{r} + \frac{1}{\Omega^2}\frac{\mathrm{d}(\Omega^2)}{\mathrm{d}r}\right]\phi' + (\Omega^2 - k^2)\phi = 0. \tag{3.39}$$

Thus, solution of Equation (3.39) yields the eigenmodes of the system.

3.2.4 Two-shell model

Recall that the Alfvén speed v_A is a function of r. Thus, any suitable functional form of v_A with r can be chosen to solve Equation (3.39). We choose

$$v_A(r) = \begin{cases} \dfrac{v_0 r}{r_0} & \text{if } r < r_0 \\ \dfrac{v_1 r}{r_0} & \text{if } r > r_0. \end{cases} \tag{3.40}$$

We demonstrate the Alfvén speed profile plotted against r in Figure 3.2.

The density profile for the interface at $r = r_0$ is given by

$$\rho_0(r) = \begin{cases} \dfrac{B_0^2(r)}{v_A^2(r)} = \dfrac{B_0^2 r_0^2}{r^4 v_0^2} & r < r_0 \\ \\ = \dfrac{B_0^2 r_0^2}{r^4 v_1^2} & r > r_0. \end{cases} \tag{3.41}$$

We note that if $v_1 < v_0$, the density of the inner layer is less than that of the outer layer, and that there is a discontinuity. Considering pressure balance above and below the interface, it must be the case that the temperature drops sharply at the radius $r = r_0$, for increasing r.

For $r < r_0$ (and later following a similar procedure for $r > r_0$), we see that

$$\phi'' + \frac{1}{r}\phi' - \left(\frac{\nu_0^2}{r^2} + k^2\right)\phi = 0, \tag{3.42}$$

where

$$\nu_0^2 = m^2 - \frac{\omega^2 r_0^2}{v_0^2}. \tag{3.43}$$

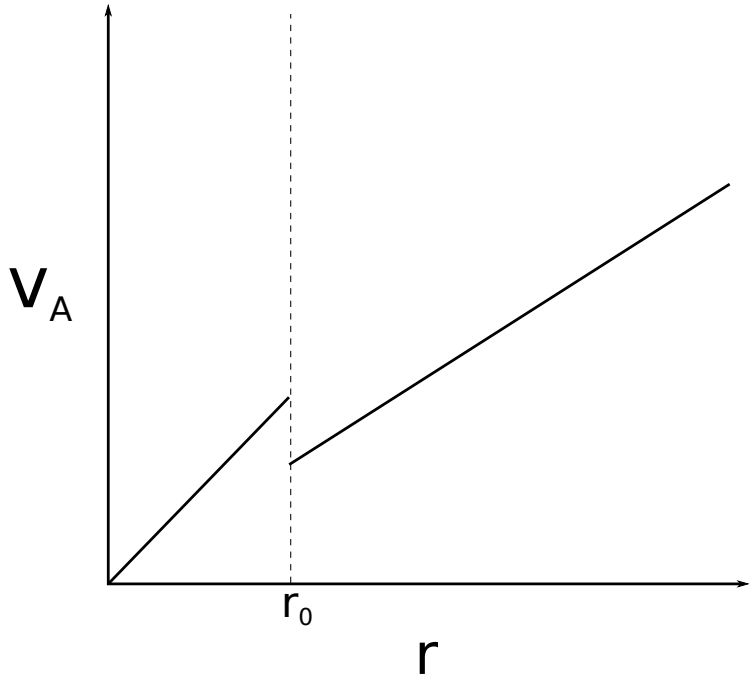

Figure 3.2: An arbitrary two-shell Alfvén speed profile $v_A(r)$, for the case where $v_1 < v_0$, plotted against radius r.

Therefore, Equation (3.42) has solutions

$$\phi = \begin{cases} A_1 I_{\nu_0}(kr) + B_1 K_{\nu_0}(kr) & r < r_0 \\ A_2 I_{\nu_1}(kr) + B_2 K_{\nu_1}(kr) & r > r_0, \end{cases} \tag{3.44}$$

where $\nu_1^2 = m^2 - \frac{\omega^2 r_0^2}{v_1^2}$, I and K are the first and second kind of modified Bessel function, respectively. The constants A_1, A_2, B_1 and B_2 can be obtained with appropriate boundary conditions. However, there are limiting values of r, and conditions on ν_0 and ν_1 for which these solutions become unbounded (and therefore unphysical). Firstly, we note that for $r \to 0$, we must have ν_0 real, otherwise I_{ν_0} becomes recessive. Additionally, we must have $B_1 = 0$ since K_{ν_0} is unbounded for both ν_0 being real and imaginary, as $r \to 0$. Similarly, for ν_1 real, $I_{\nu_1} \to \infty$ as $r \to \infty$, and for ν_1 imaginary, I_{ν_1} is complex and $|I_{\nu_1}|$ tends to ∞. Thus, $A_2 = 0$, and since K_{ν_1} is bounded and real for both ν_1 real and imaginary as $r \to \infty$, (3.44) reduces to

$$\phi_1 = A_1 I_{\nu_0}(kr) \quad r < r_0 \tag{3.45}$$

$$\phi_2 = B_2 K_{\nu_1}(kr) \quad r > r_0, \tag{3.46}$$

the eigenfunctions for the system. We form the dispersion relation based on the continuity of the above equations, to find the eigenmodes for the system and thus investigate oscillatory behaviour.

3.2.5 Dispersion relation

The magnetic pressure must be continuous. Thus, the dispersion relation obtained by imposing the continuity of ϕ and $\Omega^2 u_r$ $(= \phi')$ is

$$\frac{\nu_0^2}{\nu_1^2}\frac{K'_{\nu_1}(kr_0)}{I'_{\nu_0}(kr_0)} = \frac{K_{\nu_1}(kr_0)}{I_{\nu_0}(kr_0)}. \tag{3.47}$$

Using $\phi = r^{-\frac{1}{2}}w(r)$, Equation (3.42) can also be written as

$$w'' + \left[\left(\frac{1}{4} - \nu_0^2\right) r^{-2} - k^2\right] w = 0. \tag{3.48}$$

Repeating the same calculations for $r > r_0$ yields a similar equation:

$$w'' + \left[\left(\frac{1}{4} - \nu_1^2\right) r^{-2} - k^2\right] w = 0. \tag{3.49}$$

The coefficient of $w(r)$ in this equation describes the propagating and evanescent nature of the waves. Firstly, we must non-dimensionalise (3.49). Let

$$w = \frac{U}{\tau} \quad \text{and} \quad r = RL, \tag{3.50}$$

where τ is the typical scale length for w and L is the typical scale length for r.

Substituting these (3.49) yields

$$\frac{\mathrm{d}^2U}{\mathrm{d}R^2} \cdot \frac{1}{\tau L^2} + \frac{1}{\tau L} U \cdot F(R) = 0 \tag{3.51}$$

$$\implies \frac{\mathrm{d}^2U}{\mathrm{d}R^2} + UF(R) \cdot L = 0. \tag{3.52}$$

In order to plot the behaviour of the waves, we set this non-dimensionalised coefficient of (3.52) to 0 to give

$$L\left[\frac{\left(\frac{1}{4} - m^2 + \frac{\omega^2 r_0^2}{v_1^2}\right)}{r^2} - k^2\right] = 0 \tag{3.53}$$

$$\implies \left(\frac{1}{4} - m^2 + \frac{\omega^2 r_0^2}{v_1^2}\right) - k^2 R^2 L^2 = 0 \tag{3.54}$$

$$\implies \left(\frac{1}{4} - m^2 + \frac{\omega^2 r_0^2}{v_1^2}\right) - k^2 r_0^2 = 0, \tag{3.55}$$

since we can choose L so that r_0 satisfies this.

Rearranging (3.55) yields the equation

$$\frac{\omega^2 r_0^2}{v_1^2} = m^2 + k^2 r_0^2 - \frac{1}{4}. \tag{3.56}$$

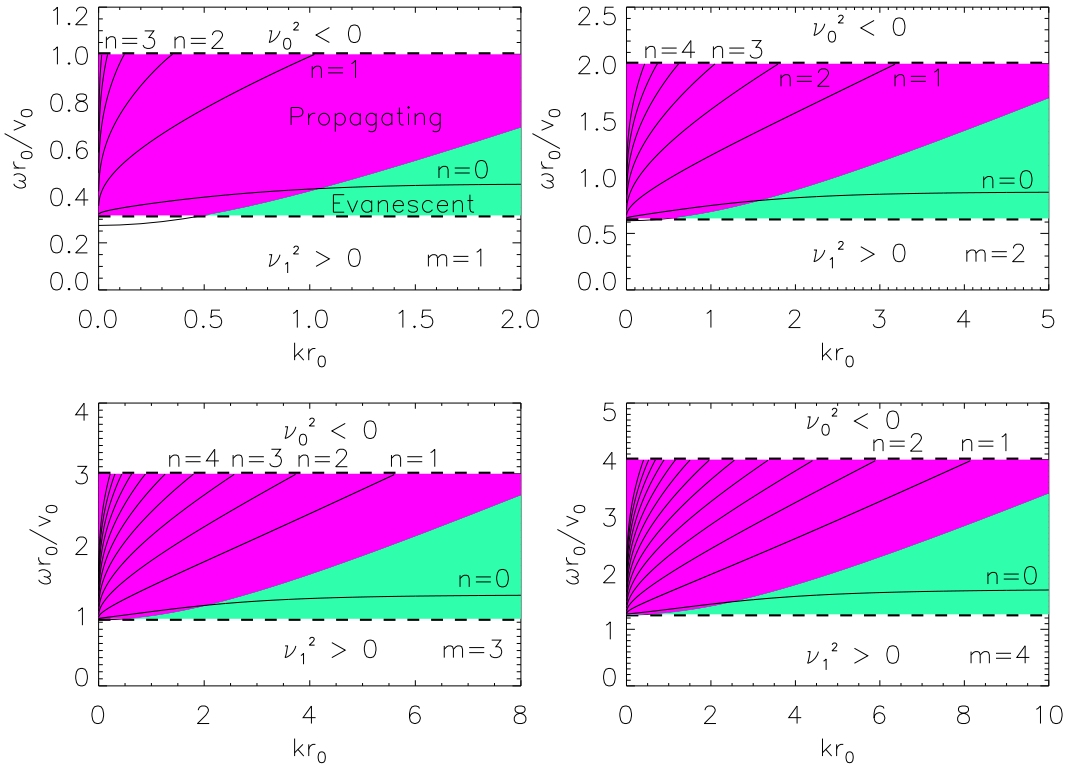

Figure 3.3: Plots of $\frac{\omega r_0}{v_0}$ against kr_0 for $m = 1, 2, 3, 4$, $\frac{v_1^2}{v_0^2} = 0.1$.

The relation in Equation (3.56) gives the critical eigenfrequency $\frac{\omega r_0}{v_0}$ in terms of wavenumber kr_0, above which modes are propagating, and below are evanescent.

In Figure 3.3, we plot $\frac{\omega r_0}{v_0}$ as a function of kr_0 for $m = 1, 2, 3$ and 4. We assume $\frac{v_1^2}{v_0^2} = 0.1$, and in doing so we see that the density of the loop increases across the interface, by (3.41), and the Alfvén speed decreases, by (3.40).

3.2.6 Plots of the two-shell model

3.2.6.1 Case I: $\frac{v_1^2}{v_0^2} = 0.1$

The magenta section in Figure 3.3 shows the area where waves are propagating and the green section shows the area where waves are evanescent. The dashed lines indicate the boundaries for which waves exist. The top boundary, i.e. where $\nu_0^2 < 0$, exists because I must be real. Since this happens only when ν_0 is pure imaginary, any ν_0 such that $\nu_0^2 < 0$ is excluded. Similarly, we have the condition that $\nu_1^2 < 0$, since if we have $\nu_1^2 > 0$, then the parity of each side of (3.47) does not match. Hence, the region shown above the dashed line of $\nu_1^2 < 0$ is the only possible region for solutions to exist.

Each of the curves represents the angular frequencies and corresponding wave-numbers for which (3.47) is satisfied, and the order of n represents the number of nodes in the radial direction in the corresponding eigenfunction. As m increases, the slope of the curves become less steep, and so a higher number of propagating modes exist.

We now choose two values of kr_0 (0.2 and 1) and plot the eigenfunction ϕ, the non-dimensionalised radial velocity $\frac{u_r}{V_0}$, the non-dimensionalised axial velocity $\frac{u_y}{V_0}$, and the polarisation fraction, f as a function of r, shown in Figure 3.4 and Figure 3.5. The polarisation fraction f is defined by

$$f = \frac{|u_y|^2}{|u_r|^2 + |u_y|^2}. \tag{3.57}$$

These are scaled for each value of n so that the amplitudes of each eigenfunction lie between -1 and 1.

As we can see in the top left plot of Figure 3.4, the curves are continuous, with each coloured curve displaying the number of nodes given by n. The curve for $n = 0$ decays quickly for $kr > kr_0 = 0.2$, with the curves for $n = 1$ and $n = 2$ also decaying soon after. The eigenfunction does not exist for $n = 3, 4, ...$, as expected from in Figure 3.3. Similarly, for the top right plot, the eigenfunction does not exist for $n = 2, 3, ...$

Since $\frac{u_r}{V_0}$ and $\frac{u_y}{V_0}$ are functions of ϕ (see Equation (3.19)), they exist for the same values of n. The curves in Figure 3.5 for $\frac{u_y}{V_0}$ are discontinuous at kr_0 in each case. The final two plots of Figure 3.5 are of the polarisation fraction, f.

From this, we can easily see that where f gets close to 1, the dominating term is u_y, and so the velocity is mainly axial. Similarly, where f goes to 0, the dominating term is u_r, and the velocity is mainly radial.

3.2.6.2 Case II: $\frac{v_1^2}{v_0^2} = 0.01$

In addition to density contrast, the Alfvén velocity constrasts can also change the nature of the wavemodes. We examine a case of $v_1^2 \ll v_0^2$, as follows. Consider the case where $\frac{v_1^2}{v_0^2}$, such that we only get lower frequency waves. An example where you would obtain high frequency waves is the case $\frac{v_1^2}{v_0^2} = 0.01$. Figure 3.6 shows that all curves $n \geq 0$ are now propagating. The number of modes has also drastically increased — for $kr_0 = 0.2$, there are now curves for $n = 0$ up to $n = 11$. Since the quantity $\frac{v_1^2}{v_0^2} = 0.01$ has decreased from 0.1, it follows that the lower boundary for which solutions are permitted has also decreased, due to the constraint ${\nu_1}^2 > 0$.

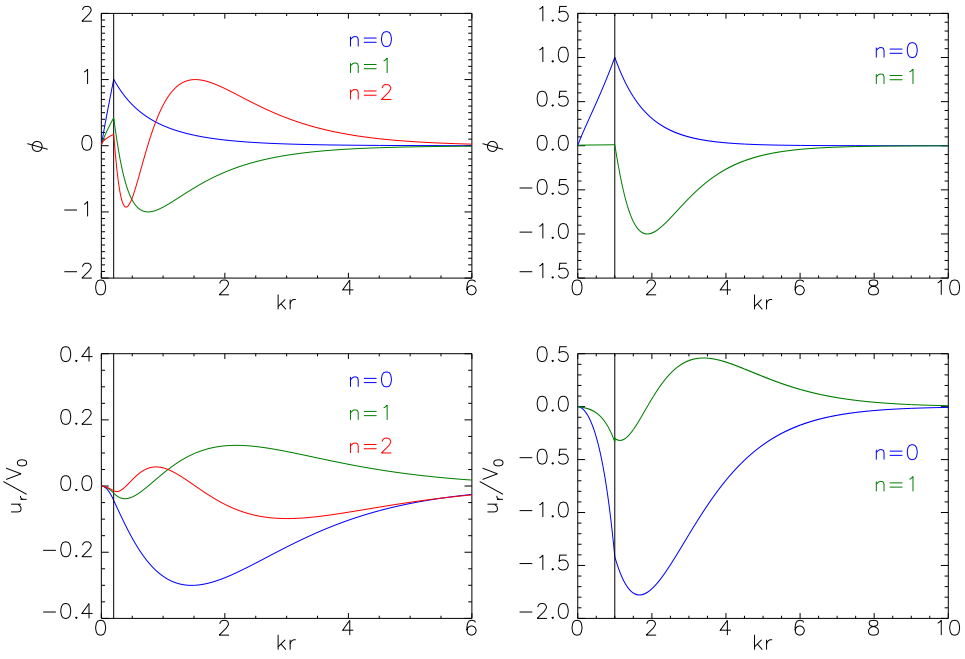

Figure 3.4: Plots of the eigenfunction ϕ and the radial velocity $\frac{u_r}{V_0}$ against radius kr, for $m = 1$, for $kr_0 = 0.2$ and $kr_0 = 1$. The vertical line denotes the value of kr_0.

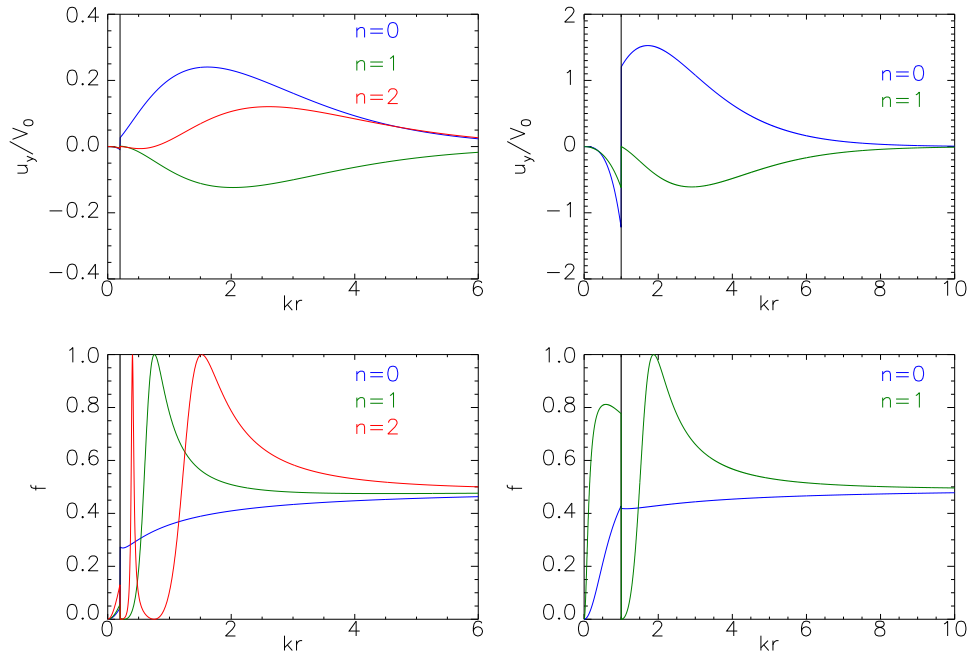

Figure 3.5: Plots of the axial velocity $\frac{u_y}{V_0}$, and the polarisation factor, f, against radius kr, for $m = 1$, for $kr_0 = 0.2$ and $kr_0 = 1$. The vertical line denotes the value of kr_0.

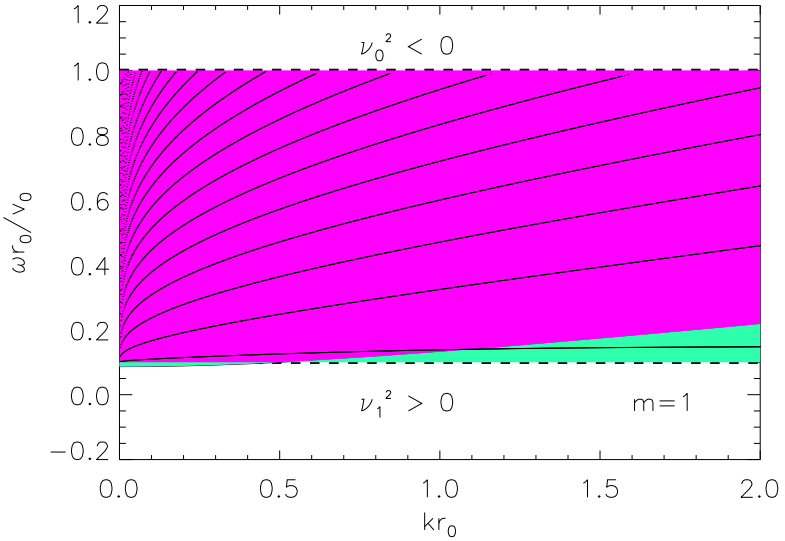

Figure 3.6: Plots of $\frac{\omega r_0}{v_0}$ against kr_0 for $m = 1$, $\frac{v_1^2}{v_0^2} = 0.01$.

Hence, using the two-shell model, we have shown the existence of fast modes with both radial and axial motion. However, observationally, the density contrasts of a coronal loop arcade do not necessarily appear as a sharp discontinuity as prescribed by Equation (3.41). Furthermore, there may be finer density structures within the coronal loops and their background which may be difficult to ascertain observationally, and this variation may contribute to changes in oscillatory behaviour. To this end, we extend the two-shell model and form a three-shell model, where loops may lie in a thin middle shell, and analyse the nature of the fast modes produced.

3.3 Three-shell model

3.3.1 The "Saw-tooth" model

We choose a finite region of density instead of a sharp interface, so that now we have three shells. The aim is to investigate the consequence of a slightly less discontinuous density between the inner and outer plasmas. The Alfvén speed is chosen such that

$$v_A(r) = \begin{cases} \dfrac{v_0}{r_0} r & r < r_0 \\ \dfrac{v_m}{r_0} r & r_0 \leq r \leq r_0 + a \\ \dfrac{v_1}{r_0} r & r_0 + a < r. \end{cases} \tag{3.58}$$

The positive constants r_0 and a describe the thickness of the middle layer. Setting $a = 0$ returns to the original two shell model. We once again plot the Alfvén speed profile for arbitrary parameters against r in Figure 3.7.

Here, we deal with new values for ν^2:

$$\nu^2 = \begin{cases} \nu_0^2 = m^2 - \dfrac{\omega^2 r_0^2}{v_0^2} & r < r_0 \\ \nu_m^2 = m^2 - \dfrac{\omega^2 r_0^2}{v_m^2} & r_0 \leq r \leq r_0 + a \\ \nu_1^2 = m^2 - \dfrac{\omega^2 r_0^2}{v_1^2} & r_0 + a < r. \end{cases} \tag{3.59}$$

As before, if we choose v_m and v_1 such that $v_1 < v_m < v_0$, then we can immediately see that there is a discontinuity between densities at both interfaces (r_0 and $r_0 + a$). In this case, the outer layer is denser than the middle layer, and the middle layer is denser than the inner-most layer.

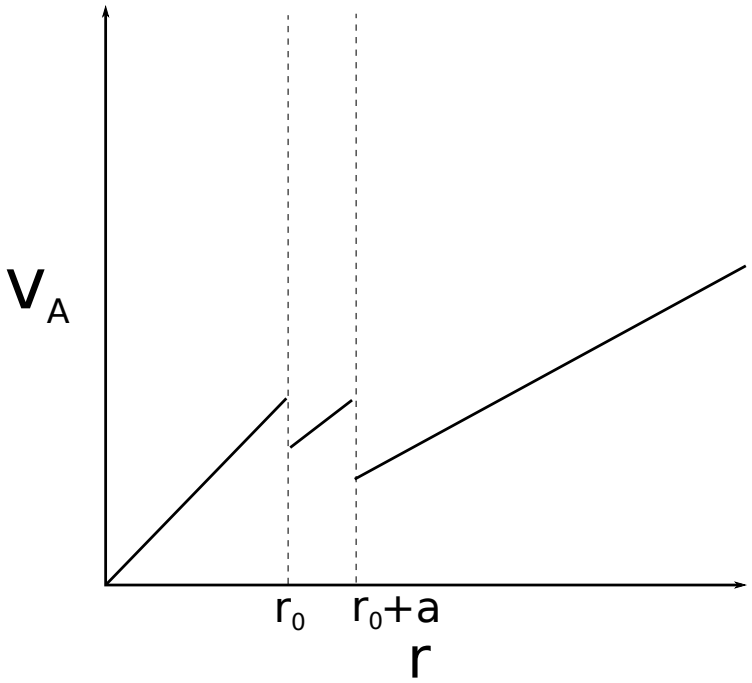

Figure 3.7: An arbitrary three-shell Alfvén speed profile $v_A(r)$, for the case where $v_1 < v_m < v_0$, plotted against radius r.

However, we are not restricted to choosing the velocities in such a way. Hence, for $\nu_m^2 > 0$, there is also the possibility of $v_1 < v_0 < v_m$. In this case, the middle cavity is less dense just after the first interface than in the inner cavity ($r < r_0$), and becomes much more dense after the second interface ($r > r_0 + a$). For $\nu_m^2 < 0$, the velocity profile such that $v_m < v_1 < v_0$ is possible, so that the middle shell is much denser then the outer-most shell.

Though we are comparing the behaviour to that of the two-layer model, it must be noted that the allowed eigenfrequencies for the new system will invoke slight changes in the behaviour of the eigenfunction and associated velocities in the first layer. However, these small changes are negligible in comparison to the two-layer case, and become indistinguishable over large wavenumbers.

Recall the equilibrium magnetic field is $\mathbf{B_0} = \left(0, \frac{B_0}{r}, 0\right)$. The new density profile is such that

$$\rho_0(r) = \begin{cases} \dfrac{B_0^2 r_0^2}{r^4 v_0^2} & r < r_0 \\ \dfrac{B_0^2 r_0^2}{r^4 v_m^2} & r_0 \leq r \leq r_0 + a \\ \dfrac{B_0^2 r_0^2}{r^4 v_1^2} & r_0 + a < r. \end{cases} \tag{3.60}$$

Thus, the governing equation is given by

$$\phi'' + \frac{1}{r}\phi' - \left(\frac{\nu^2}{r^2} + k^2\right)\phi = 0, \tag{3.61}$$

with ν taking different values ν_0, ν_m and ν_1 in regions $r < r_0$, $r_0 \leq r \leq r_0 + a$ and $r > r_0 + a$, respectively. Depending on the choice of $\nu_m^2 > 0$ or $\nu_m^2 < 0$, the region for which the fast waves can propagate changes.

Considering the case where $\nu_m^2 > 0$, the solution now becomes

$$\phi = \begin{cases} A_1 I_{\nu_0}(kr) & r < r_0 \\ A_2 I_{\nu_m}(kr) + B_2 K_{\nu_m}(kr) & r_0 \leq r \leq r_0 + a \\ B_3 K_{\nu_1}(kr) & r_0 + a < r, \end{cases} \tag{3.62}$$

since the boundary conditions for $r \to 0$ and $r \to \infty$ are the same as in the two-shell case. Applying the continuity of ϕ and $\Omega^2 u_r\,(= \phi')$ at $r = r_0$ and $r = r_0 + a$, we derive the new dispersion relation:

$$\begin{aligned} &\frac{\nu_0^2 I_{\nu_0}(kr_0)K'_{\nu_m}(kr_0) - \nu_m^2 I'_{\nu_0}(kr_0)K_{\nu_m}(kr_0)}{\nu_m^2 I'_{\nu_0}(kr_0)I_{\nu_m}(kr_0) - \nu_0^2 I_{\nu_0}(kr_0)I'_{\nu_m}(kr_0)} \\ =&\frac{\nu_1^2 K_{\nu_1}(k(r_0+a))K'_{\nu_m}(k(r_0+a)) - \nu_m^2 K_{\nu_m}(k(r_0+a))K'_{\nu_1}(k(r_0+a))}{\nu_m^2 I_{\nu_m}(k(r_0+a))K'_{\nu_1}(k(r_0+a)) - \nu_1^2 K_{\nu_1}(k(r_0+a))I'_{\nu_m}(k(r_0+a))}. \end{aligned} \tag{3.63}$$

We can also consider the case where $\nu_m^2 < 0$. Since the function I_{ν_m} is complex when $\nu_m^2 < 0$, we instead must employ a new kind of modified Bessel function L, defined by

$$L_\nu(kr) = \frac{\pi i}{2\sin(\nu\pi)}\left\{I_\nu(kr) + I_{-\nu}(kr)\right\} \tag{3.64}$$

to ensure a real solution (see Dunster (1990)). We note that, for comparison, the second modified Bessel function may be expressed similarly, as

$$K_\nu(kr) = \frac{\pi}{2\sin(\nu\pi)}\left\{I_{-\nu}(kr) - I_\nu(kr)\right\}, \tag{3.65}$$

where the inclusion of i as in (3.64) allows for the case of $\nu_m^2 < 0$.

Hence, the solution becomes

$$\phi = \begin{cases} A_1 I_{\nu_0}(kr) & r < r_0 \\ A_2 L_{\nu_m}(kr) + B_2 K_{\nu_m}(kr) & r_0 \leq r \leq r_0 + a \\ B_3 K_{\nu_1}(kr) & r_0 + a < r, \end{cases} \tag{3.66}$$

with corresponding dispersion relation

$$\begin{aligned}&\frac{\nu_0^2 I_{\nu_0}(kr_0)K'_{\nu_m}(kr_0) - \nu_m^2 I'_{\nu_0}(kr_0)K_{\nu_m}(kr_0)}{\nu_m^2 I'_{\nu_0}(kr_0)L_{\nu_m}(kr_0) - \nu_0^2 I_{\nu_0}(kr_0)L'_{\nu_m}(kr_0)}\\ =&\frac{\nu_1^2 K_{\nu_1}(k(r_0+a))K'_{\nu_m}(k(r_0+a)) - \nu_m^2 K_{\nu_m}(k(r_0+a))K'_{\nu_1}(k(r_0+a))}{\nu_m^2 L_{\nu_m}(k(r_0+a))K'_{\nu_1}(k(r_0+a)) - \nu_1^2 K_{\nu_1}(k(r_0+a))L'_{\nu_m}(k(r_0+a))}.\end{aligned} \tag{3.67}$$

3.3.2 Plots of the "Saw-tooth" model

3.3.2.1 Case I: $\nu_m^2 > 0$

We plot the propagation diagrams in Figure 3.8 for $ka = 0.1$, $\frac{v_m^2}{v_0^2} = 0.5$, and $\frac{v_1^2}{v_0^2} = 0.1$. As before, we found eigenfrequencies and wavenumbers which satisfy the corresponding dispersion relation (3.67). Since the eigenfrequencies will be different from the two-shell model, the behaviour before $r = r_0$ will be slightly different, though across large distances, the difference in behaviour would be negligible. Note that since we have $\nu_m^2 > 0$, but also $\nu_m < \nu_0$, the upper boundary for propagation is lower than in the two-shell case. Note that higher order nodes are absent when comparing Figure 3.8 to 3.3, which is largely due to the lowering of the upper boundary of the propagation region, a direct consequence of $\nu_m^2 > 0$, but also due to the lowered density of the middle region. We conclude that the middle layer with less density contrast inhibits the propagation of higher order radial modes. For $kr_0 = 0$, it is as if we only have the middle region and the outer region. Hence, the only interface is now at $kr_0 + ka = 0.1$, and it is as if there already is an impermeable interface between two regions, much like in the two-layer model. The effect once we have plotted the eigenfrequency curves is that of "shifting" the curves to the left on the two-layer plot in 3.3.

In Figure 3.9, we plot the variation of the eigenfunctions ϕ, the radial and axial velocities u_r and u_y and the polarisation fraction f, against the wavenumber. We plot these for the three-layer model for $ka = 0.1$ and $\frac{v_m^2}{v_0^2} = 0.5$, in the right panel, and for comparison plot the case where $ka = 0$ and $\frac{v_m^2}{v_0^2} = 1$ in the left panel. As expected, we notice that by setting $ka = 0$ and $\frac{v_m^2}{v_0^2} = 1$ in our new dispersion relation (see Equation (3.63)), we return to the same curves as in the two-layer model (shown in Figure 3.4). This can easily be verified from the left panel of Figure 3.9. We normalise with respect to the maximum value of each eigenfunction, so that the curves lie between -1 and 1.

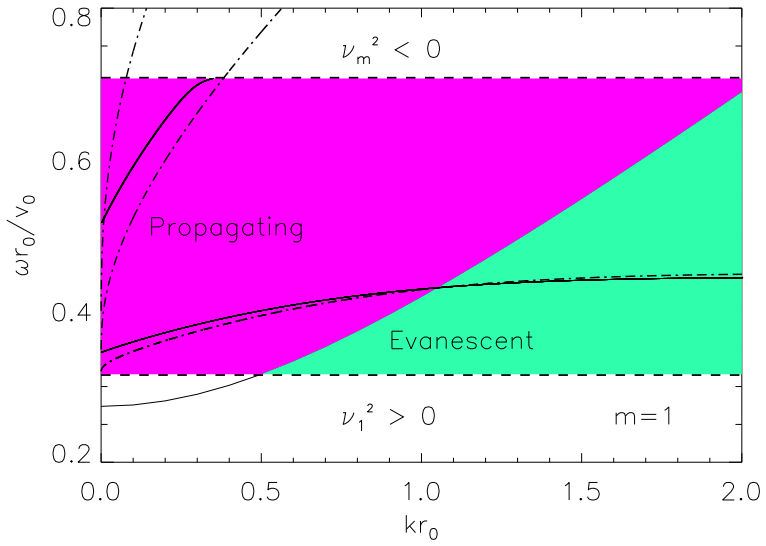

Figure 3.8: Plots of $\frac{\omega r_0}{v_0}$ against kr_0 for the case where $ka = 0.1$, $\frac{v_m^2}{v_0^2} = 0.5$, $\frac{v_1^2}{v_0^2} = 0.1$, $m = 1$ and $\nu_m^2 > 0$. The dash-dot curves indicate the corresponding curves in the two-layer model.

In Figure 3.9, we see that there are no curves for modes $n \geq 2$. The overall shape of the curve for $n = 0$ in the right panel is similar to that in the left, with the eigenfunction now reaching it's maximum at the second interface, further out from the origin. Similarly, the qualitative behaviour of the $n = 1$ curve is the same, with the lowest point of the curve occuring for a slightly larger wavenumber.

Figure 3.9 also shows the non-dimensionalised radial (u_r) and axial (u_y) velocities. As anticipated, the radial velocity in each case is continuous, with the axial velocity remaining discontinuous, though now at the second interface, rather than at kr_0. After the second interface, the qualitative behaviour of the radial and axial velocity is similar in the left and right panels. However, in the middle layer, we see that the radial velocity is further suppressed by the plasma.

By increasing the thickness of ka to 0.5, we note that all trapped modes are now suppressed, leaving only the $n = 0$ curve. This is shown in Figure 3.10. The qualitative shape of the eigenfunctions in Figure 3.11 remain mostly the same as in Figure 3.9, though the polarisation fraction (bottom right panel) shows that the $n = 0$ model indicates that the motion becomes more axial less sharply at the interface than for the thinner middle shell of Figure 3.9.

The plots of polarisation fraction, f, clearly demonstrate that, depending

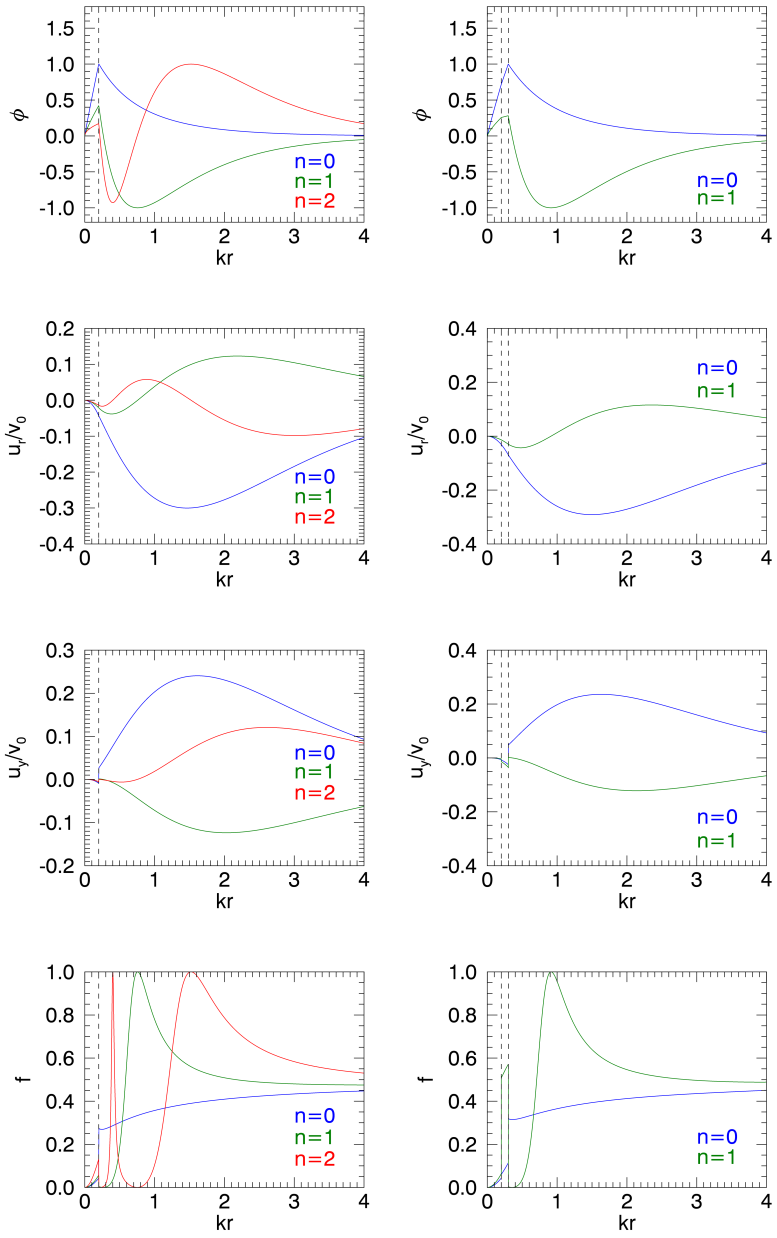

Figure 3.9: Plots of the eigenfunction ϕ, radial velocity u_r, axial velocity u_y and polarisation fraction f, using the dispersion relation in (3.63). The left panel shows the case $ka = 0$, $\frac{v_m^2}{v_0^2} = 1$, $\frac{v_1^2}{v_0^2} = 0.1$, for $kr_0 = 0.2$ and $m = 1$. The right panel is similar except now $ka = 0.1$ and $\frac{v_m^2}{v_0^2} = 0.5$.

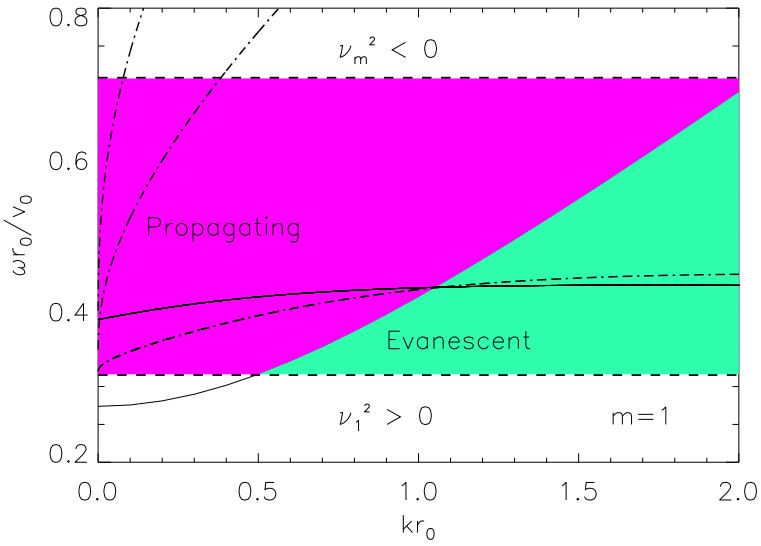

Figure 3.10: Plots of $\frac{\omega r_0}{v_0}$ against kr_0 for the case where $ka = 0.5$, $\frac{v_m^2}{v_0^2} = 0.5$, $\frac{v_1^2}{v_0^2} = 0.1$, $m = 1$ and $\nu_m^2 > 0$. The dash-dot curves indicate the corresponding curves in the two-layer model.

on the location of the observation (i.e. the line of sight), the horizontal or vertical polarisation dominates one or the other. Additionally, our investigation of the two-layer and three-layer cases clearly show that the eigenvalues and eigenfunctions are sensitive to the Alfvén speed profiles. Therefore, to understand the plasma properties of a coronal loop from the measurement of the observed frequency, the correct mode identification is crucial.

3.3.2.2 Case II: $\nu_m^2 < 0$

Plotting the propagation diagram as before in Figure 3.8, for $ka = 0.1$, $\frac{v_m^2}{v_0^2} = 0.5$ and $\frac{v_1^2}{v_0^2} = 0.1$, we obtain Figure 3.12. The value of $\frac{v_m^2}{v_0^2} = 0.5$ now alters the lower boundary for solutions, and we only obtain propagating solutions. Here, it appears as though the eigenfrequency curves have shifted right compared to the curves in the two-layer model, in the opposite manner to the $\nu_m^2 > 0$ case.

Following the second interface, the qualitative behaviour of the eigenfunction, and the radial and axial velocities is much the same as the two layer case, however we only have curves for $n = 1$ and $n = 2$. The polarisation fraction f once again indicates both radial and axial motion, with some wavenumbers giving purely radial or purely axial movement.

As in the case where $\nu_m^2 > 0$, we also plot the case where $ka = 0.5$. Once again, we only have propagating solutions. However, computation of the

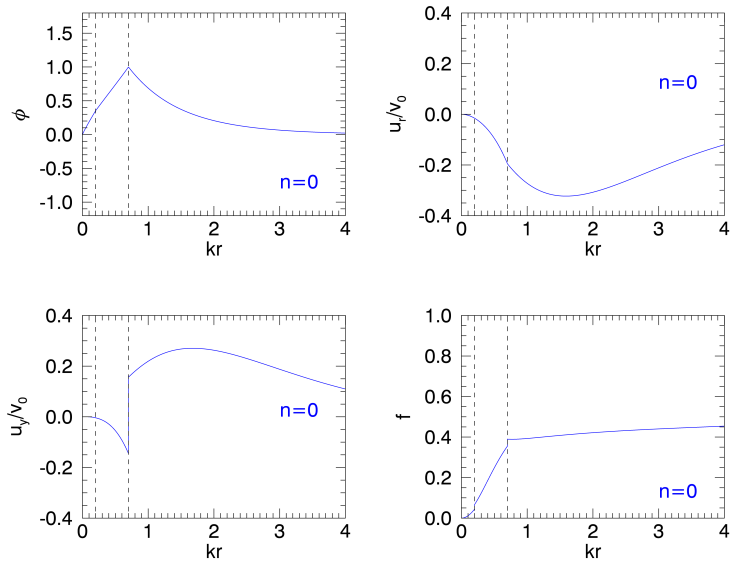

Figure 3.11: Plots of the eigenfunction ϕ, radial velocity u_r, axial velocity u_y and polarisation fraction f, for the case where $ka = 0.5$, $\frac{v_m^2}{v_0^2} = 0.5$, $\frac{v_1^2}{v_0^2} = 0.1$, for $kr_0 = 0.2$ and $m = 1$.

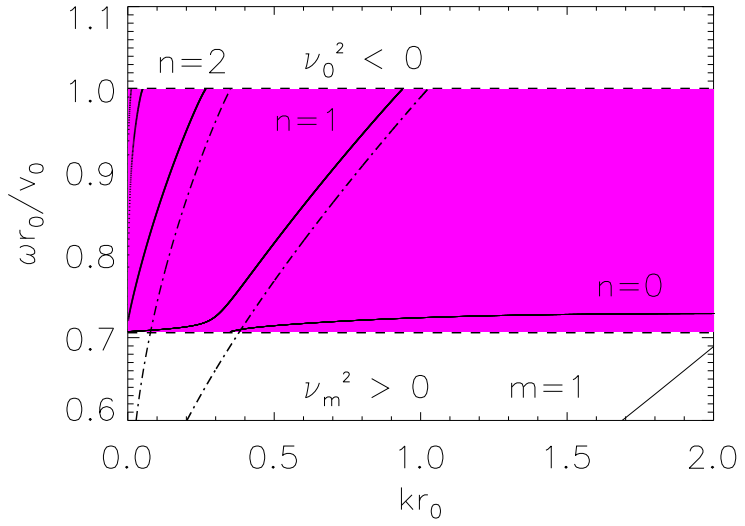

Figure 3.12: Plots of $\frac{\omega r_0}{v_0}$ against kr_0 for the case where $ka = 0.1$, $\frac{v_m^2}{v_0^2} = 0.5$, $\frac{v_1^2}{v_0^2} = 0.1$, $m = 1$ and $\nu_m^2 < 0$.

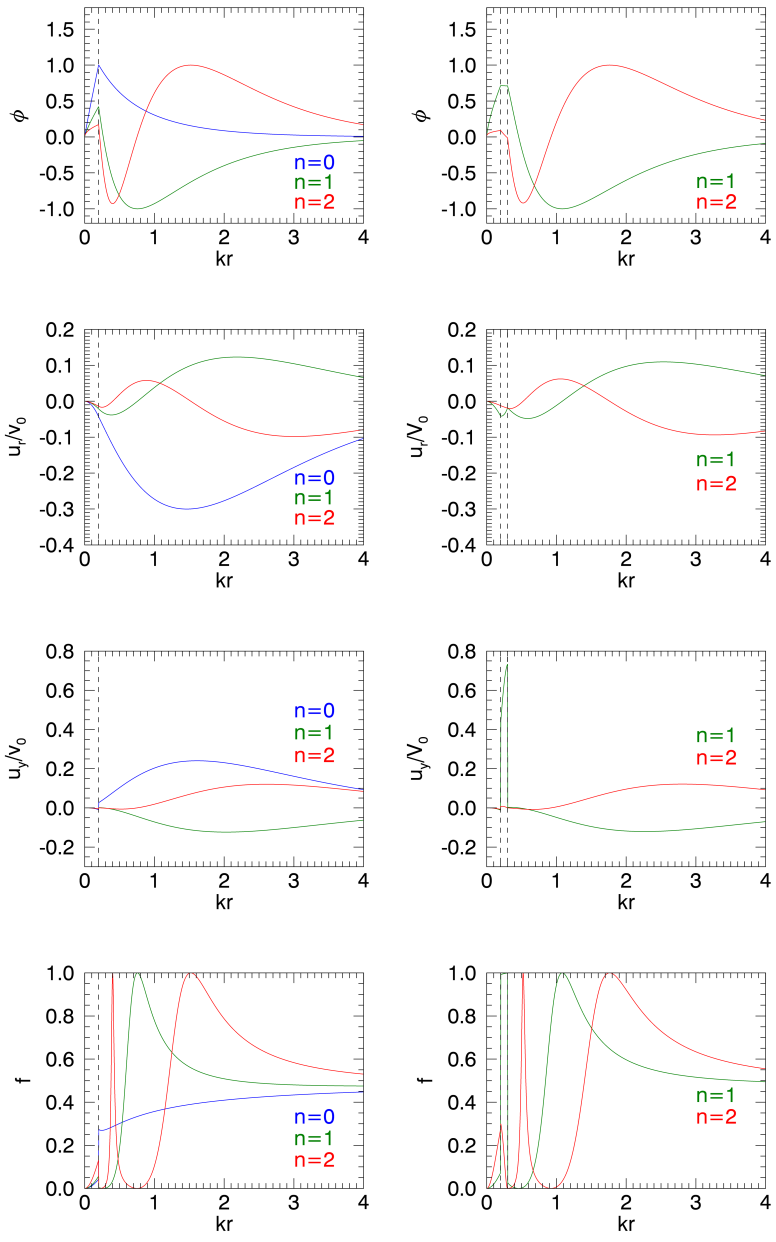

Figure 3.13: Plots of the eigenfunction ϕ, radial velocity u_r, axial velocity u_y and polarisation fraction f, using the dispersion relation in (3.67), for the case $ka = 0$ (left), $\frac{v_m^2}{v_0^2} = 1$, $\frac{v_1^2}{v_0^2} = 0.1$, for $kr_0 = 0.2$, $m = 1$ and $\nu_m^2 < 0$, and $ka = 0.1$ (right). The vertical dashed lines are the two interfaces.

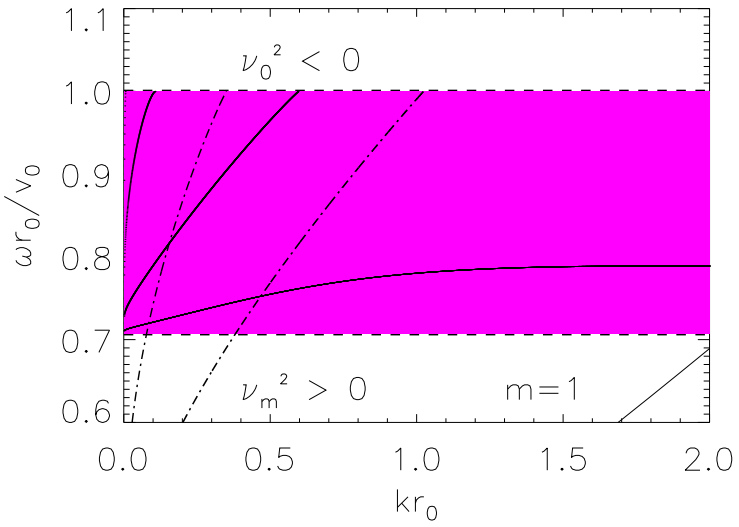

Figure 3.14: Plots of $\frac{\omega r_0}{v_0}$ against kr_0 for the case where $ka = 0.5$, $\frac{v_m^2}{v_0^2} = 0.5$, $\frac{v_1^2}{v_0^2} = 0.1$, $m = 1$ and $\nu_m^2 < 0$.

eigenfunctions in Figure 3.14 indicates a shift in behaviour after the second interface. We can no longer distinguish the two radial modes of the $n = 2$ case, though careful comparison with previous plots as in Figure 3.12, it is seen that we have both the $n = 1$ and $n = 2$ curves once again. Behaviour of eigenfunctions and the radial and axial velocities after this second interface is similar to that in the two-layer case in Figures 3.4 and 3.5. We note that once again the motion is both axial and radial in nature, with some wavenumbers exhibiting only axial or only radial motion.

3.3.3 The "Upside-down tilted hat" model

3.3.4 Plots of the "Upside-down tilted hat" model

To further probe the possible density structures of the coronal arcade, the three-shell models are extended to the case where the Alfvén velocity is the same for the inner-most cavity as in the outmost shell. That is, construct the profile such that $v_0 = v_1$, and consider the case where $\frac{v_m^2}{v_0^2}$ varies from 1. We plot the "Upside-down tilted hat" Alfvén speed profile for arbitrary parameters against r in Figure 3.16.

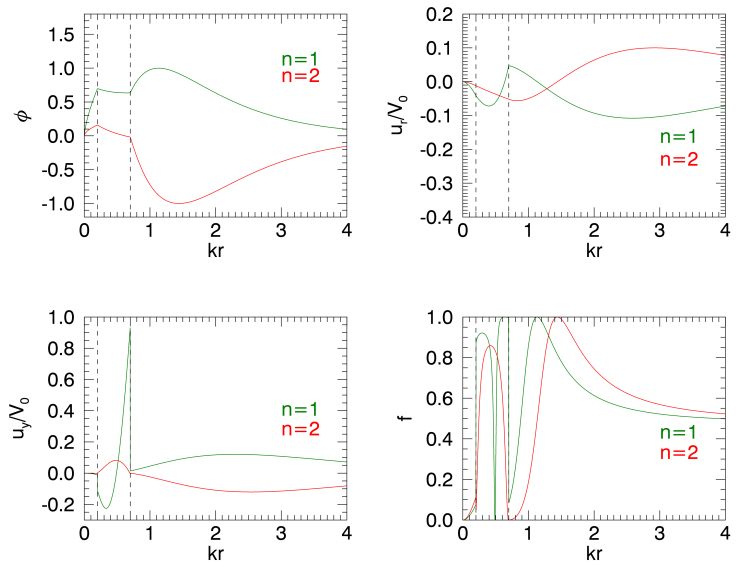

Figure 3.15: Plots of the eigenfunction ϕ, radial velocity u_r, axial velocity u_y and polarisation fraction f, for the case where $ka = 0.5$, $\frac{v_m^2}{v_0^2} = 0.5$, $\frac{v_1^2}{v_0^2} = 0.1$, for $kr_0 = 0.2$, $m = 1$ and $\nu_m^2 < 0$.

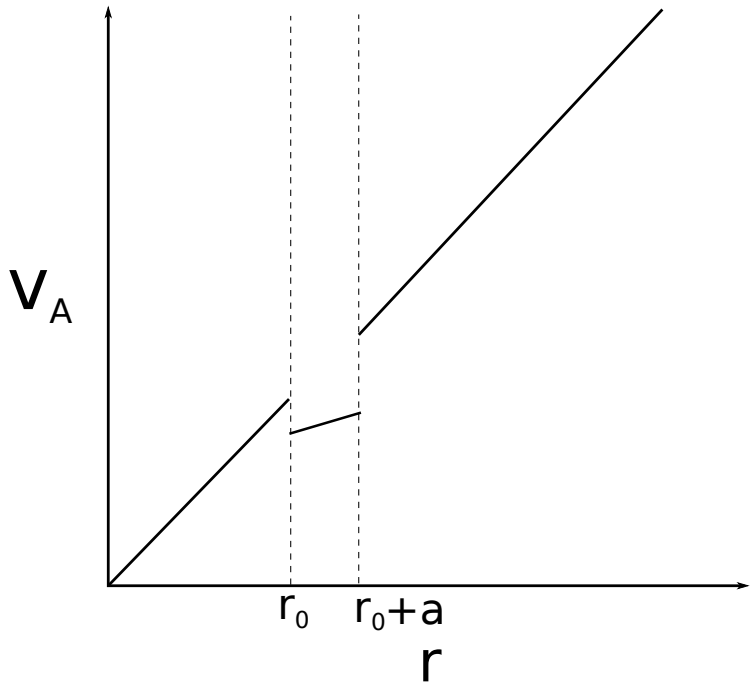

Figure 3.16: An arbitrary three-shell Alfvén speed profile $v_A(r)$, for the case where $v_1 = v_0$ and $v_m < v_0$, plotted against radius r.

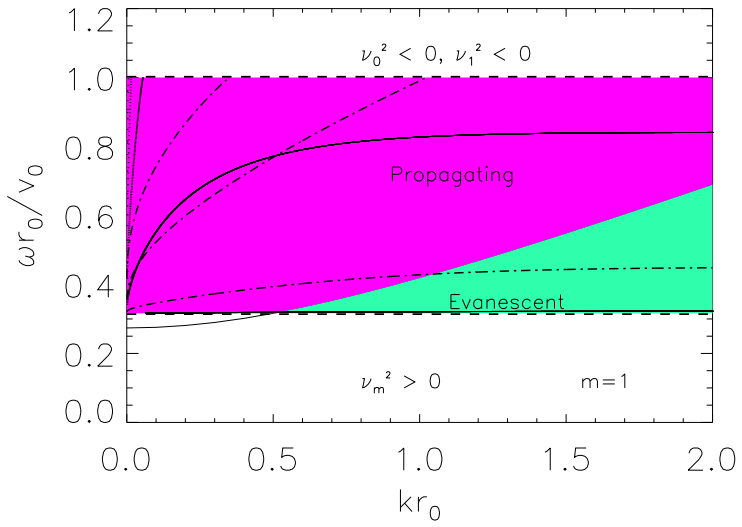

Figure 3.17: Plots of $\frac{\omega r_0}{v_0}$ against kr_0 for the case where $ka = 0.1$, $\frac{v_m^2}{v_0^2} = 0.1$, $\frac{v_1^2}{v_0^2} = 1$, $\nu_m^2 < 0$, and $m = 1$.

3.3.4.1 Case I: $ka = 0.1$

We consider the case where $\frac{v_m^2}{v_0^2} = 0.1$. Accordingly, this correlates to a shell which has a density ten times that of the cavity inside and the shell outside. Since $v_1 = v_0$, ν_1^2 must be greater than zero, so for eigenfrequency solutions to exist, it is necessary that $\nu_m^2 < 0$. The Alfvén speed profile is given as before in (3.59), and thus the eigenfunctions remain the same as in (3.66), since solutions are still required to be bounded as $r \to 0$ and $r \to \infty$.

To compare with results in previous sections, we start by taking $ka = 0.1$. Solving the dispersion relation as given in (3.67), we obtain the propagation diagram as before, shown in Figure 3.17.

Note that the $n = 0$ curve now sits close to the lower bound of the frequencies, and now the $n = 1$ curve asymptotes to some fixed value as kr_0 increases. The remaining curves for $n = 2$ and higher only exist for small kr_0. In Figure 3.18, taking the first interface at $kr_0 = 0.2$ as before, we plot the corresponding eigenfunctions, velocities and polarisation fraction for each wavenumber kr. We notice that it now appears there are two surface waves for $n = 0$ and $n = 1$, with the $n = 0$ curve exhibiting much higher axial velocity between the two interfaces. This is further demonstrated in the polarisation plot, as the middle region indicates completely axial motion, before both axial and radial motion beyond the second interface.

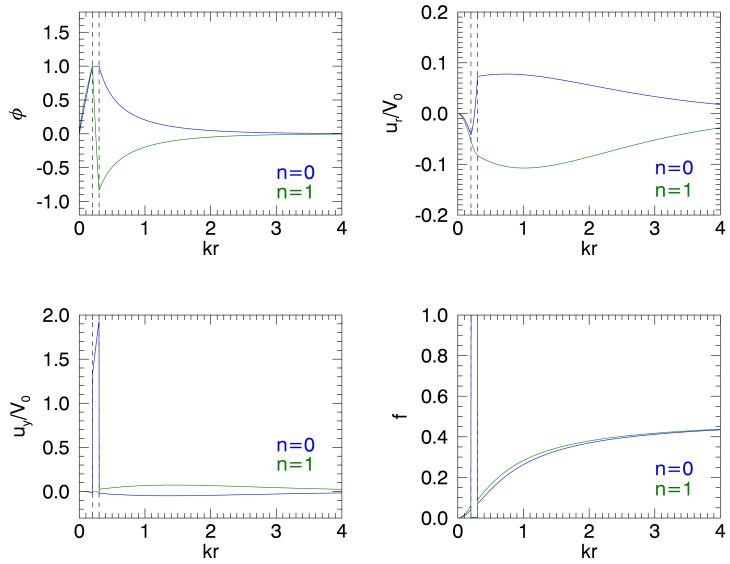

Figure 3.18: Plots of the eigenfunction ϕ, radial velocity u_r, axial velocity u_y and polarisation fraction f, for the case where $ka = 0.1$, $\frac{v_m^2}{v_0^2} = 0.1$, $\frac{v_1^2}{v_0^2} = 1$, $\nu_m^2 < 0$, for $kr_0 = 0.2$, and $m = 1$.

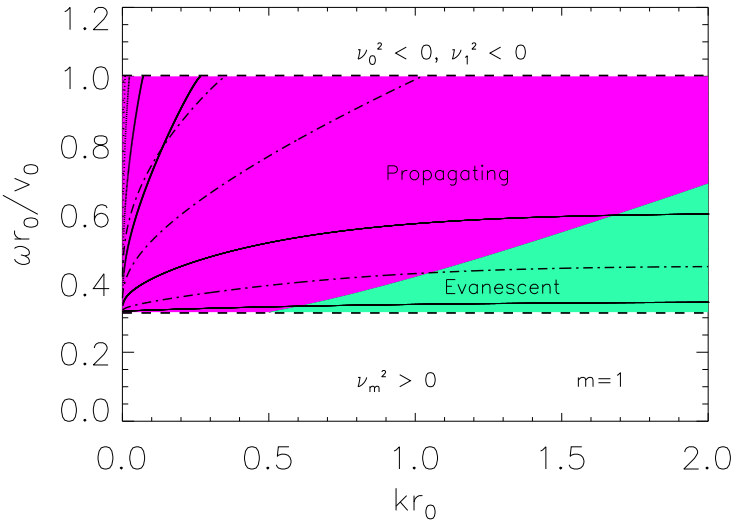

Figure 3.19: Plots of $\frac{\omega r_0}{v_0}$ against kr_0 for the case where $ka = 0.5$, $\frac{v_m^2}{v_0^2} = 0.1$, $\frac{v_1^2}{v_0^2} = 1$, $\nu_m^2 < 0$, and $m = 1$.

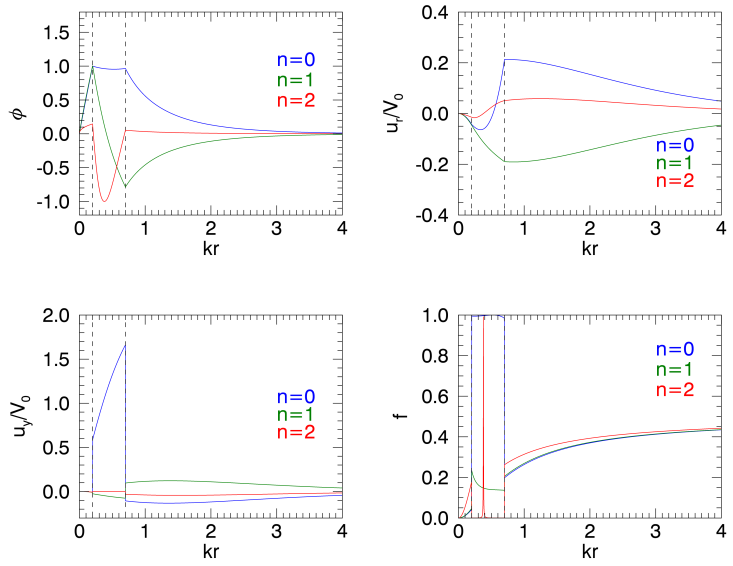

Figure 3.20: Plots of the eigenfunction ϕ, radial velocity u_r, axial velocity u_y and polarisation fraction f, for the case where $ka = 0.5$, $\frac{v_m^2}{v_0^2} = 0.1$, $\frac{v_1^2}{v_0^2} = 1$, $\nu_m^2 < 0$, for $kr_0 = 0.2$ and $m = 1$.

3.3.4.2 Case II: $ka = 0.5$

Increasing the thickness of the middle layer from $ka = 0.1$ to $ka = 0.5$ as before now permits more radial modes, as shown in Figure 3.19. As in Figure 3.18, there are two evanescent modes, and now an additional propagating mode, which is illustrated further in Figure 3.20. The $n = 2$ mode exhibits a node between kr_0 and $kr_0 + ka$. We may contrast this with Edwin and Roberts (1983) — increasing the thickness of the cylinder gave rise to additional body modes, though in the coronal limit, no surface modes were produced.

Between kr_0 and $kr_0 + ka$, the $n = 0$ mode possesses a sharp increases in axial velocity, further demonstrated by the polarisation fraction plot. Similarly, the $n = 2$ has mostly axial motion between the two radii, whilst the $n = 1$ mode appears to be mostly radial.

3.3.5 Reduction of the three-shell model

In extreme limits of ka, it can be shown that the three-shell model may be reduced to the two-shell model of Hindman and Jain (2015), through reduction of the dispersion relation in Equation (3.63).

3.3.5.1 $ka \to 0$

We first show that this is the case for when the thickness of the middle shell becomes infinitesimally thin i.e. $ka \to 0$. Since we will show that the middle shell disappears from the relation, we do not require that I_{ν_m} be real, or make any distinctions on the sign of ${\nu_m}^2$.

Taking $ka \to 0$ in Equation (3.63) yields

$$\frac{\nu_0^2 I_{\nu_0}(kr_0)K'_{\nu_m}(kr_0) - \nu_m^2 I'_{\nu_0}(kr_0)K_{\nu_m}(kr_0)}{\nu_m^2 I'_{\nu_0}(kr_0)I_{\nu_m}(kr_0) - \nu_0^2 I_{\nu_0}(kr_0)I'_{\nu_m}(kr_0)} \tag{3.68}$$

$$= \frac{\nu_1^2 K_{\nu_1}(kr_0)K'_{\nu_m}(kr_0) - \nu_m^2 K_{\nu_m}(kr_0)K'_{\nu_1}(kr_0)}{\nu_m^2 I_{\nu_m}(kr_0)K'_{\nu_1}(kr_0) - \nu_1^2 K_{\nu_1}(kr_0)I'_{\nu_m}(kr_0)} \tag{3.69}$$

$$\implies \nu_0^2 I_{\nu_0}(kr_0)K'_{\nu_1}(kr_0)[I_{\nu_m}(kr_0)K'_{\nu_m}(kr_0) - I'_{\nu_m}(kr_0)K_{\nu_m}(kr_0)] \tag{3.70}$$

$$= \nu_1^2 I'_{\nu_0}(kr_0)K_{\nu_1}(kr_0)[I_{\nu_m}(kr_0)K'_{\nu_m}(kr_0) - I'_{\nu_m}(kr_0)K_{\nu_m}(kr_0)] \tag{3.71}$$

$$\implies \nu_0^2 I_{\nu_0}(kr_0)K'_{\nu_1}(kr_0) = \nu_1^2 I'_{\nu_0}(kr_0)K_{\nu_1}(kr_0), \tag{3.72}$$

which is the dispersion relation as in Equation (3.47).

3.3.5.2 $ka \to \infty$

It can be shown that in the limit of large ka, the dispersion relation for the three-shell model (see Equation (3.63)) can also be reduced to an approximation to the dispersion relation of the two-shell model (Equation (3.47)). Again, we do not require that I be real, however, it must be the case that ${\nu_m}^2 < 0$, so the parity of the dispersion relation may be preserved.

In order to take the limit of $ka \to \infty$, note that we may reduce the modified Bessel functions I and K in the following manner

$$K_\nu(kr) \approx \sqrt{\frac{\pi}{2kr}}e^{-kr}, \tag{3.73}$$

$$K'_\nu(kr) \approx -k\sqrt{\frac{\pi}{2kr}}e^{-kr} - \frac{1}{2}\sqrt{\frac{\pi}{2kr^3}}e^{-kr} \tag{3.74}$$

and

$$I_\nu(kr) \approx \frac{e^{kr}}{\sqrt{2\pi kr}}, \tag{3.75}$$

$$I'_\nu(kr) \approx \frac{ke^{kr}}{\sqrt{2\pi kr}} - \frac{1}{2}\frac{e^{kr}}{\sqrt{2\pi kr^3}} \tag{3.76}$$

as $kr \to \infty$ (see Olver *et al.* (2010)).

Thus,

$$\frac{K'_\nu(kr)}{K_\nu(kr)} = k - \frac{1}{2r}, \quad \frac{I'_\nu(kr)}{I_\nu(kr)} = k - \frac{1}{2r},$$
$$\frac{I_\nu(kr)}{K_\nu(kr)} = \frac{e^{2kr}}{\pi}, \quad \frac{I'_\nu(kr)}{K_\nu(kr)} = \frac{e^{kr}}{\pi}\left[k - \frac{1}{2r}\right]. \tag{3.77}$$

Rearranging the right hand side of Equation (3.67),

$$\frac{\nu_1^2 \dfrac{K_{\nu_1}(k(r_0+a))K'_{\nu_m}(k(r_0+a))}{K_{\nu_m}(k(r_0+a))K'_{\nu_1}(k(r_0+a))} - \nu_m^2}{\nu_m^2 \dfrac{I_{\nu_m}(k(r_0+a))}{K_{\nu_m}(k(r_0+a))} - \nu_1^2 \dfrac{I'_{\nu_m}(k(r_0+a))K_{\nu_1}(k(r_0+a))}{K'_{\nu_1}(k(r_0+a))K_{\nu_m}(k(r_0+a))}}, \tag{3.78}$$

and from (3.77) becomes

$$\frac{\pi(\nu_1^2 - \nu_m^2)e^{-2kr}}{\nu_m^2 + \nu_1^2\left(\dfrac{2kr-1}{2kr+1}\right)} \to 0, \tag{3.79}$$

as $ka \to \infty$.

Thus, Equation (3.47) may be reduced to

$$\frac{\nu_0^2}{\nu_m^2}\frac{K'_{\nu_m}(kr_0)}{I'_{\nu_0}(kr_0)} = \frac{K_{\nu_m}(kr_0)}{I_{\nu_0}(kr_0)}. \tag{3.80}$$

3.4 Summary

Hindman and Jain (2015) proposed that, rather than modelling coronal loop structures as a single vertical flux tube, a loop arcade should be modelled in its entirety, forming a semi-cylinder, embedded in the photosphere. Here it is important to note that observations of arcades indicate inhomogeneity throughout the waveguide, and in particular, in a direction transverse to the magnetic field lines. However, by assuming that the scale length of inhomogeneity in the axial direction is much larger than that in height, we ignore any effects from inhomogeneity down the arcade axis. Section 3.2 details this set-up, describing the arcade in terms of cylindrical polar coordinates. Introducing the perturbed velocity field in Section 3.2.2, Section 3.2.3 yields the governing equation for the geometry, in terms of eigenfunction ϕ, leading to solutions in terms of modified Bessel functions. Here, the two-shell model of Hindman and Jain (2015) is presented as a sharp density contrast (see Section 3.2.4), and a dispersion relation (Equation (3.47)) is established. Numerical solutions

of Equation (3.47) lead to propagation diagrams, and in turn yield information about the propagating and evanescent modes present. Hence, we find the eigenfunctions for a specific density interface location, followed by the radial and axial velocities. Most importantly, the polarisation fraction is obtained, giving a measure of the radial or axial nature of each eigenfunction, respectively. Section 3.3 repeats a similar analysis with the introduction of a second spike in density, forming a thin shell.

The introduction of the polarisation fraction in Sections 3.2.4 and 3.3 confirms an important observational aspect of coronal loop arcades. In particular, data analysis of observed coronal loop intensities in Jain, Maurya and Hindman (2015) proposed interaction between adjacent loops, highlighting the existence of a wave propagating perpendicularly to the loop tops, down the axis of the coronal loop arcade. This was further conjectured in Hindman & Jain (2015), where the two-shell model in Section 3.2.4 was first proposed. In this Chapter, it was shown that, when modelled as a 3-dimensional semi-cylindrical arcade, the resultant eigenfunctions exhibited both radial and axial motions, indicating elliptically polarised waves.

Most notably, by careful consideration of both Sections 3.2.4 and 3.3, it is clear that the choice of density profile should not be made frivolously. Small changes to the interface location as in Figures 3.4 and 3.5 suppresses the existence of modes, and changes to the density contrast could suppress or augment the resultant modes. Introduction of the second interface only complicates matters: since coronal loops are viewed as bright structures within a faint background, it follows that the loops are comparatively dense. Assuming a density profile which quickly decreases in height allows for waves to be more easily refracted back to the surface, whilst more slowly decreasing profiles cause eigenfunctions to disappear. However, the stratification of the background may not be completely isotropic, and so choice of density structure even in the three-shell case must be taken with care (see Figures 3.9, 3.11 and 3.18).

It would possibly be judicious here to compare the resultant modes of the coronal loop model in Cartesian coordinates (from Chapter 3) with that in the cylindrical geometry of the current Chapter. However, this remains difficult — the Alfvén speed profile for the two and three-shell models is assumed to be linearly increasing in each shell, so that the modes may be trapped radially. However, in the Cartesian model, the Alfvén speeds are assumed to *decrease* exponentially in height. Hence, comparisons of the fast and Alfvén

mode solutions may not yield accurate conclusions in the context of coronal loop modelling. In addition, the Cartesian model of Chapter 2 allowed for decoupling of the fast and Alfvén modes — in this Chapter, it was shown that both modes were coupled, thus manifesting as elliptical motion. However, we showed that Cartesian and cylindrical models could both have fast mode solutions decaying far from the loop arcade, in the coronal approximation.

The preliminary paper of Edwin and Roberts (1983) gave light to a cylindrical model in the context of MHD. There, propagation was only considered parallel to the magnetic field fields, i.e. the case where the three-shell model would have axial wavenumber $k = 0$. Furthermore, the densities examined in Edwin and Roberts (1983) are uniform in each region, whilst varying here, for the two and three-shell models. However, even though the two models for coronal structures in cylindrical coordinates are difficult to compare, it can be noted that the existence of surface modes in the middle shell as in Figure 3.18 is also acknowledged in Figure 5 of Edwin and Roberts (1983).

In reality, the two-shell model of Section 3.2.4 may be extended far beyond the three-shell model of Section 3.3 to any number of interfaces; however, it is clear that even a small change to the density structure may lead to the suppression of modes. Additionally, both the models discussed neglected to include gas pressure, due to the zero-β approximation of the corona. Though gas pressure does, indeed, contribute less to the dynamics of the system than magnetic terms, a more realistic model of a coronal loop arcade would involve consideration of these pressure terms. Finally, we note that the loops are taken to be of the same height, though we see observationally that loop tops vary drastically in height, and though loops may sit in the same arcade, neighbouring loops will have distinctly different properties. All of these simplifications aside, it is clear that a semi-cylindrical model for a coronal loop structures represent better the "realistic" arcades as viewed in observations.

CHAPTER 4

Subsurface flows in flaring and non-flaring solar coronal active regions

4.1 Introduction

Many studies concerning active regions focus on their propensity to emit *solar flares*. Priest (2013) gives a thorough overview of the mechanisms behind solar flaring and related events, but here we give a brief summary.

Historically, solar flares were described as short brightenings in the Hα spectral line. However, in recent times, solar flares were found to emit X-rays (Peterson and Winckler (1959)), and the brightening in Hα was likely due to interactions between the emitted magnetised plasma and particles, and the chromosphere. The classification of such flares depends on their maximum X-ray flux, and ranges across A, B, C, M or X classes, with A being the smallest and X being the largest. The maximum flux of flares increases by a factor of 10 from one class to another.

There are four stages in the process of a solar flare (Heyvaerts *et al.* (1977)). First is the *pre-flare phase*, where the intensity of the soft X-rays build. Next comes a hard X-ray and microwave burst, as electrons are accelerated internally, known as the *impulsive phase*. The particles are further accelerated in the *rise phase*, where the soft X-ray intensity rapidly increases and surrounding plasma in the corona becomes swiftly heated. Finally comes the *main phase*, where intensity slowly decreases.

This chapter is based on the following journal article which has been submitted pending peer review:

- Thackray, H., Jain, R., Jain, K., Tripathy, S., Hill, F.; Subsurface flows of active regions associated with eruptive and confined flares in Solar Cycle 24, *Astron. Astrophys.*, recommended for publication following revisions (Dec 2019)

During this flaring process, the conversion between magnetic energy and particle motion causes surrounding plasma to heat up and move. In doing so, flares may stimulate wave motions, and in particular may be capable of initiating coronal loop oscillations. Some types of waves or bursts associated with flaring events (and resultant shock waves) include *Moreton waves* which are detected in the chromosphere as fast modes, presented in the Hα spectral line (Athay and Moreton (1961)). These fast shock waves are also known as *EIT waves*, so-called because of their discovery using the Extreme ultraviolet Imaging Telescope (EIT) by Thompson *et al.* (1998).

Flares may be categorised by many different characteristics, but we will focus on those which are *eruptive* or *confined*. Eruptive flares are those which have an associated *coronal mass ejection* (CME), and confined flares are those without. CMEs present a much larger threat to the Earth than solar flares, since the ejected magnetised plasma blobs can interfere with the Earth's magnetic field and cause widespread transformer blackouts. Hence, the prediction of solar flares (and thus CMEs) has significance in the context of protecting and maintaining infrastructure here on Earth.

Magnetic reconnection is one of the most common processes thought to be behind the production of solar flares. Here, magnetic field lines "break" suddenly, possibly due to rearrangements by subsurface flows, and reconnect in a different orientation, causing magnetic energy to be quickly released. This energy transfers into kinetic energy, and the shock waves produced excite particles, ejecting them out of the photosphere and into the corona. Reconnection is thought to be the catalyst for the impulsive phase of the flare.

Since magnetic reconnection processes reconfigure the field lines and the associated plasma flows, it is important to examine flows in and around the active regions. As the field lines of the coronal active regions are anchored below the surface, it is obvious to investigate any signatures of flaring, if any, in this layer of the Sun. In this Chapter, we examine the differences between flaring and non-flaring active regions, by investigating the subsurface flows using helioseismic techniques. In particular, we use a technique in the frequency-wavenumber domain, *Ring Diagram Analysis*, introduced below in Section 4.3. Chosen flaring active regions are those that produced X-class flares, since these are the most energetic, and the most likely to cause shock waves which could onset coronal loop oscillations in neighbouring loops. Different approaches to determining these subsurface flows are discussed in Section 4.4, before a thorough

examination of flaring and non-flaring regions from Solar Cycle 24 is presented in Section 4.4.3.

4.2 Helioseismology

In Section 1.4.2, we covered the basics of helioseismology, with reference to uncovering the structures inside the Sun using frequencies obtained at the surface. In this section, helioseismology and its relevance is covered in more detail, from the first observational evidence of solar oscillations, to the types of modes examined, and the need for both global and local helioseismology. For extensive reviews on helioseismology, see, for example, Christensen-Dalsgaard (2002), Thompson (2004) or Basu (2016).

4.2.1 Solar oscillations

The first concrete observational evidence of solar oscillations was presented by Leighton *et al.* (1962) through the use of Doppler velocity shifts at the surface of the Sun. Examination of localised velocities led to the discovery of oscillations with a period of around 5 minutes. However, their initial interpretation was to attribute these motions to the convection beneath the solar surface. It was only later that further observational analysis revealed the existence of global acoustic modes resonating in the vast cavities of the Sun (Deubner (1975)) as the cause of the Doppler shift. Though the push for higher resolution spectral imaging was highlighted, Deubner (1975) discussed the use of such modes for diagnosis of the interior of the Sun.

In the region lying closest to the surface, the instability of the convection zone lends itself to the excitation and damping of these solar oscillations as they reflect off from the inside of the photosphere. On the whole, these solar oscillations are mainly acoustic in nature, and thus are reliant on pressure as a restoring force: as such, they are referred to as p-modes. Furthermore, some modes may be mostly dependent on buoyancy, and so may be called g-modes, or gravity modes. However, the richness of the Sun's interior means that the sound-speed, with which the acoustic modes propagate, changes dependent on their instantaneous location. Since the gas pressure increases rapidly as the waves approach the core, they slow down and change direction, before speeding back up to the surface.

Modelling the Sun's interior using a spherical coordinate system, and assuming the oscillations are low amplitude enough in comparison to the scales

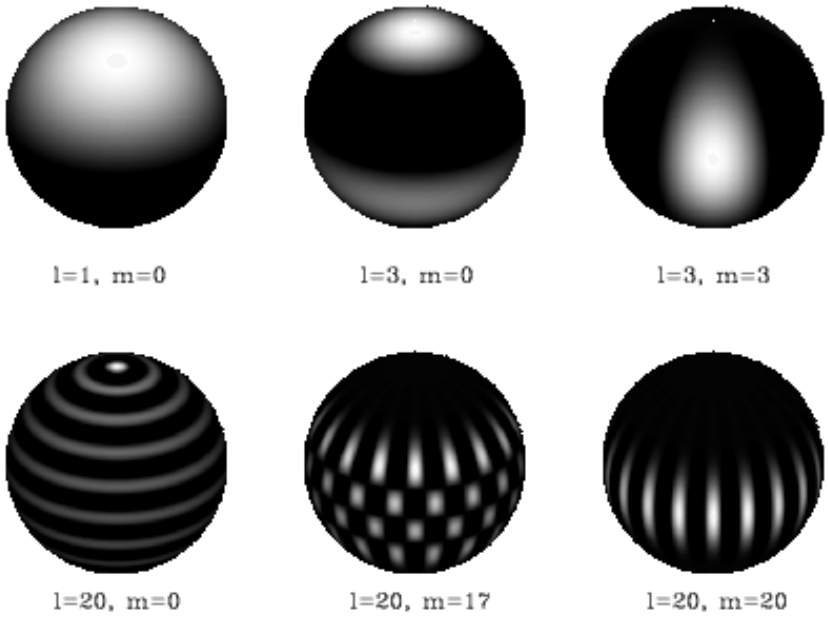

Figure 4.1: A demonstration of spherical harmonics for different combinations of degree, l, and order, m. White and black indicate motions in opposite directions. Credit: inspirehep.net

of the background, the oscillations poleward (north-south) and parallel to the equator (east-west) are represented in terms of spherical harmonics

$$Y_l^m(\theta, \phi). \tag{4.1}$$

Here, l, known as the degree, gives information about oscillations in the θ direction, and m, known as the order, gives information about oscillations in the azimuthal (or ϕ) direction. Each of these parameters are integers, where l must be positive or zero, and $-l \leq m \leq l$. Consideration of boundary conditions for the radial component of the oscillations (i.e. towards the centre of the sphere) introduces the radial order n, whose magnitude defines the number of nodes found from the surface to the centre of the Sun. Hence, all oscillations have some unique frequency, which may be classified as $\omega_{n,l,m}$ for some values of n, l and m. Figure 4.1 illustrates the spherical harmonics of varying degree and order.

It is this radial order which defines whether a mode finds their restoring force mainly in gas pressure or buoyancy — p-modes have positive values of n and high frequencies, and g-modes have negative values and low frequencies.

The mode corresponding to $n = 0$ is known as the f-mode, and observationally we mainly see global modes of low n-values in the form of f and p-modes, since these are the ones most easily affected by the innermost workings of the Solar interior. However, higher order radial modes are observed locally, and it is in these modes that the flows closest to the photosphere may present themselves.

These solar oscillations are mainly observed using Dopplergrams, which give information about line-of-sight velocity at the Sun's photosphere, from the Doppler shifting in spectral lines. This is covered in more detail in Section 4.3.1, however, we first discuss how helioseismology has been employed both globally and locally with respect to the Sun's interior.

4.2.2 Global helioseismology

Helioseismology has been successfully used to examine global properties of the Sun for over 30 years (for example, see Deubner and Gough (1984)). Since the p-modes are dominantly acoustic, and their properties thus dependent on the sound speed, models connecting sound speed and subsurface depth have been developed, discussed in detail in Christensen-Dalsgaard *et al.* (1996).

One such achievement following the development of such solar models, is the determination of the location of the convection zone (Christensen-Dalsgaard *et al.* (1991)), which was found to within 0.003 solar radii. In particular, studies of the rotation rate depending on the location have been conducted, with the different structures and densities of the radiative and convective zones respectively holding a large role (Schou *et al.* (1998)). There, a rapid change in rotation was found at the bottom of the convection layer. A major result following this was the thin tachocline lying between the radiative and convective zones, which could be important in relation to the solar dynamo.

Comparison of the Sun and standard models indicated differences in structuring, giving light to the "solar neutrino problem" (see, Basu (2016), for example). Observations of neutrino flux was around a third of the expected value as predicated by standard models. It was here that helioseismology proved an indispensable tool, for its use in prediction of temperature in the solar interior, and thus information regarding neutrino flux (Antia and Chitre (1997)). There, it was shown that a model for the Sun could not be reconstructed using the observed neutrino flux values, and thus there was some exterior mechanism causing the production of neutrinos to be suppressed.

However, in the context of this thesis, we concern ourselves with local helioseismology, which studies smaller scale motion close to the solar surface

and captures the effects of magnetic active regions, rather than motions deep into the solar interior. Some of these advances were briefly discussed in Section 1.4.2, however here we discuss some relevant results in more detail.

4.2.3 Local helioseismology

On a broad scale, helioseismology has been used to investigate the way zonal and meridional flows change throughout the solar cycle. Komm *et al.* (2014) (and subsequently Komm *et al.* (2015)) studied such changes, comparing estimations of near-surface flows with expected flows calculated using results from global helioseismology. There, zonal flows were shown to be faster (and meridional flows more poleward) than expected in the regions near the equator, and slower (and meridional flows less poleward) than expected near poles. These faster regions appeared to correlate with times when magnetic activity was highest in either hemisphere.

However, local helioseismology has proven extremely useful in the context of studying active regions, particularly those which produced solar flares. By studying the kinetic helicity density (see Moffatt and Tsinober (1992)), Komm *et al.* (2005) compared values obtained from subsurface flows of flaring active regions with the various activity indices of the flares. A good agreement was found between larger flares and regions with high kinetic helicity density values. Furthermore, Reinard *et al.* (2010) found an increase in kinetic helicity density of flaring regions in the days preceding eruption.

By examining morphology of a specific active region during the flaring process, Jain, Tripathy and Hill (2015) concluded that flow magnitudes were suppressed following the production of a flare, and that this was likely due to the conversion of kinetic energy of the subsurface flows into the energy released by the solar flare within the active region. Magnetic field rearrangement was suggested as a contributor to suppression of flow magnitudes, as well as the rotation of sunspots within the region. Repeating analyses and comparing results with a flaring active region from a different solar cycle, Jain *et al.* (2017) suggested rearrangement and sunspot rotation were not always sufficient to alter the magnitudes in flows, and this was particularly evident for active regions producing significantly large flares. The above analyses were conducted using a local helioseismological technique known as *Ring Diagram Analysis*, which we will discuss next in more detail.

4.3 Ring Diagram Analysis

4.3.1 Background to Ring Diagram Analysis

Ring Diagram Analysis (RDA) is a helioseismological technique first illustrated in Hill (1988). By examining velocities from observed Doppler shift data, RDA infers flow properties beneath the photosphere. Phenomena investigated using RDA include, but are not limited to, flows under active regions (Jain, Tripathy and Hill (2015); Komm *et al.* (2011)), variation in flows across solar cycles (Komm *et al.* (2014); Komm *et al.* (2015)) and large scale near-surface flows and sub-surface flow shearing (Howe *et al.* (2006)).

As mentioned in the previous section, the Sun is host to internal acoustic oscillations (p-modes) which have their signature in Doppler shifts at the surface. If the frequency of the p-modes in the quiet Sun, when magnetic activity is low, is considered to be $\omega_{n,l,m}$, a shift in the frequency $\Delta\omega$ due to, for example, flows in and around active regions can be described in terms of the horizontal spatial wavenumbers k_x and k_y for horizontal surface flow $\mathbf{U}$. Subsequently, $\Delta\omega$ can be written in the Cartesian coordinate system as

$$\Delta\omega = \mathbf{k} \cdot \mathbf{U} = k_x U_x + k_y U_y \tag{4.2}$$

where U_x is known as the zonal velocity, or "east-west", and U_y is the meridional velocity, or "north-south".

Generally, Doppler velocity patches of around $15° \times 15°$ are tracked at the rotation rate of the surface using Dopplergrams captured by instruments such as the Helioseismic and Magnetic Imager (HMI) on the Solar Dynamics Observatory (SDO), or by the Global Oscillation Network Group (see section 1.2) observatories (see Birch *et al.* (2007) for more details). Tracking the patches for a time period creates data cubes, denoted in reference to the Sun's rotation as $\Phi(\mathbf{x}, t)$, in the two spatial and temporal directions, which are then Fourier transformed in time. Differential rotation is thus accounted for, within the shallow layer analysed.‘ For this reason, only the larger flow patterns will survive, since smaller fluctuations will become insignificant over long timescales. For example, data is often averaged over 1664 minutes, since this is the amount of time it takes for a patch to move 15°, and is often referred to as a "ring day".

In order to reduce the projection effects, the first step in the ring analysis is *apodization* (spatially and temporally) of the data cube. This is done in

relation to the centre of the patch, so that for some central location $\mathbf{x_0}$, the apodized cube has the form

$$\Theta(\mathbf{x}, t; \mathbf{x_0}) = a(|\mathbf{x} - \mathbf{x_0}|)\Phi(\mathbf{x}, t). \tag{4.3}$$

The apodization function is assumed to have the form

$$a(x) = \begin{cases} 1, & x < x_1 \\ \left[1 - \frac{(x-x_1)^2}{(x-x_2)^2}\right]^2, & x_1 \leq x \leq x_2, \\ 0, & x > x_2. \end{cases} \tag{4.4}$$

Parameters x_1 and x_2 are determined in terms of the apodized diameter.

The data cube is then Fourier decomposed into spatial and temporal components to get a 3-D power spectrum as $P(k_x, k_y, \omega)$. Here, (k_x, k_y), which may also be written as $\mathbf{k}$, constitutes a wave-vector in the x-y directions, and ω is the observed frequency. We may express this transformed data discretely as the following series:

$$P(k_x, k_y, \omega) = \left| C_k^2 \sum_{\mathbf{k}'} a(\mathbf{k} - \mathbf{k}')\Phi(\mathbf{k}', \omega) \right|^2, \tag{4.5}$$

as in Gizon and Birch (2004). The constant C_k gives the sample length for (k_x, k_y).

The data is then fitted using a maximum likelihood procedure to a Lorentzian power spectrum profile

$$P(k_x, k_y, \omega) = \frac{A}{(\omega - \omega_0 + \mathbf{k} \cdot \mathbf{U})^2 + \Gamma^2} + \frac{b}{k^3}, \tag{4.6}$$

to completely resolve the three-dimensional power spectra. Here A is the amplitude, b is the background noise, ω_0 is the central frequency, Γ is the mode width, k is the wavenumber and $\mathbf{k} \cdot \mathbf{U}$ is the Doppler shift (Haber *et al.* (2000)). By comparison with the expected power spectrum $P_0(k_x, k_y, \omega)$, information about the perturbation in the power spectrum may be obtained, from which the flow estimates may be derived (see Birch *et al.* (2007) for more detail).

Assuming incompressibility and density variations only due to depth, RDA uses so-called "inversion" techniques to derive flows below the surface. If the flows at the surface are given by $\mathbf{U}$ as above, then the assumption that the flows $\mathbf{V}$ can be linearly interpolated at each depth means that the sub-surface flows can be related to each component of $\mathbf{U}$ in depth z, as in Greer *et al.* (2015), by

$$U_i(\mathbf{x_0}) = \int \int \mathrm{d}\mathbf{x}\, \mathrm{d}z\, \mathcal{K}_i(\mathbf{x_0} - \mathbf{x}, z) V_i(\mathbf{x}, z). \tag{4.7}$$

Here, $\mathcal{K}_i(\mathbf{x_0} - \mathbf{x})$ relates the interaction of the sub-surface velocity V_i with the perturbed power spectrum and is known as the "sensitivity kernel". The position $\mathbf{x_0}$ is the central position of the patch for which we are inverting flows. Regularized least squares can then be used to calculate the inverted flow estimate for $\mathbf{V}$.

4.3.2 Instrument: Global Oscillation Network Group (GONG)

In this study, we use data obtained by Global Oscillation Network Group (GONG), a collection of six observatories and various institutions, collecting ground-based solar data for the purpose of helioseismology. Data is collected daily, with the six observatories aligned in such a way that the Sun is viewed for the optimum amount of time, and are located in the USA, Western Australia, India, the Canary Islands and Chile. The instruments located at each of the GONG sites collect magnetic field strength, intensity and Doppler velocity data of the Sun.

For GONG Doppler velocity data, RDA products are usually calculated for an overlapping grid of 189 patches, centred on the Sun's disk. Patch centres are 7.5° apart and span from $-52.5°$ to 52.5° in both latitude and longitude. Beyond these coordinates, RDA becomes unreliable due to projection effects from contamination in the line-of-sight velocities close to the limb. However, the ring pipeline can be applied to "custom" patch locations, enabling patches to be centred on areas of interest, such as active regions.

4.3.2.1 Data

Active regions are structures of strong magnetic fields on the Photosphere. Some active regions are often host to events such as solar flares and coronal mass ejections, where plasma is expelled from the corona of the Sun at a high rate. These features are numbered once they come into view of the ground-based instruments of National Oceanic and Atmospheric Administration (NOAA), such as "AR 11166", where "AR" stands for "Active Region". Since the NOAA equipment is ground-based, the active regions can only be viewed on the side of the Sun facing Earth. Hence, when the active regions pass across the far-side and come back to the visible side, they may have a different active region number. Some active regions are relatively long-lived and thus may be given several different identifiers.

Active regions consist of loop-like structures in the corona which seem to oscillate occasionally after the eruption of flares. Many studies of such oscillations pertain to the idea that they are triggered by movement of plasma above the surface, such as by blast waves following flares. However, sub-surface flows could also cause buffeting of field lines arching out of the photosphere, and, especially if the flows are large scale, may cause oscillatory motions in collections of coronal loops.

In addition to this, research on active regions touches on the characteristics of the sunspot groups from which they are comprised. Sunspots are viewed as dark holes on the photosphere, since they are cooler than surrounding plasma. These spots occur due to the magnetic field lines arching out of the plasma, and their evolution and formation determines the cycle of their hosting active region. Sunspots may be stationary within their active regions, or may be rotating. Groups of sunspots may be unipolar (i.e. either positive or negative polarity), bipolar (where the group may be split neatly with a continuous line), or a complex mixture of the two.

Similarly, the magnetic activity index (MAI) also characterise active regions. MAI is a calculated by averaging the strongest absolute values of magnetic field strength across the patch (i.e. when $|B|$ is greater than $50G$), and is therefore used to diagnose more magnetically active regions relative to the quiet sun. A threshold of $50G$ is introduced in order to minimise spurious errors from measurements of the lower activity regions. Jain, Tripathy and Hill (2015) investigated active region 11158, and discovered an increase in MAI closer to the largest flare, which was X2.2 type and occurred on the 15th Feb 2011.

4.3.2.2 Possible sources of error

Since active regions often cover large portions of the $15^\circ \times 15^\circ$ patches, and due to the averaging of the horizontal velocities across the patch, we are able to estimate the flows directly beneath such features. However, comparison of active regions located at different positions on the Sun's disk is complicated since surface curvature means the centre of the disk seems brighter than the limb. As a result, the errors in velocity estimations become greater further away from the centre, and spatial resolution is lost (Jain, Tripathy and Hill (2015)) Additionally, the Sun's axis is inclined to the Earth, creating an annual fluctuation in the angle of the Sun's axis as viewed from the Earth, known as B_0-angle variation (Zaatri *et al.* (2006)). This shift, whilst less impactful on

the zonal velocities, causes significant changes in the estimates for meridional flows.

To combat the interference of residual flows and the B_0-angle effect, Jain, Tripathy and Hill (2015) took quiet region data from the Sun around the same time in the solar cycle, a month earlier than the active region's most active period. Flow estimates are derived for several days and then averaged in order to smooth systematic errors. Solar activity varies during the solar cycle, resulting in changes in sub-surface flows (Komm *et al.* (2014); Komm *et al.* (2015)). The solar cycle is an approximately 11 year fluctuation in the magnetic activity of the Sun. At the solar minimum, that is when magnetic activity is low, meridional flows are larger than at the solar maximum. Hence, the quiet region data must be from the same epoch as the active regions being examined (Komm *et al.* (2015)). Alternatively, data can be chosen from active regions at a similar stage in the solar cycle, to minimise influence from large-scale flows.

Additional errors can be introduced by taking a time series which is too small for RDA to be employed successfully. Short time series' give rise to large amounts of noise in the observed frequencies. Hence, when the ring pipeline is applied, the flow estimates can be unreliable. It is thus important to choose a time scale long enough to reduce the noise in the observed frequencies, but not so long that the small nuances of the flow are "ironed out". In the same way that selection of time series can instigate errors, choosing a patch that is too small can produce inconsistent flow estimates. However, most analyses as standard choose patches with area $15^\circ \times 15^\circ$.

4.4 Analysis of flaring active regions

4.4.1 A day-by-day study of several active regions

As previously discussed, Jain, Tripathy and Hill (2015) studied sub-surface flow patterns in the context of active region 11158, with a particular focus on the period between the 11th and 16th of February 2011. Using data from HMI, $12^\circ \times 12^\circ$ and $7.5^\circ \times 7.5^\circ$ regions are tracked, focussing on the whole active region. Data are obtained for consecutive calendar days.

In a similar manner, we conduct an analysis of seven active regions, at varying stages of the solar cycle, using GONG data. The data set for each active region comprises of 7 days (1440 minutes), with the flare of interest

AR #	Central date	Size of flare	Flare total	Sunspot area	Hemisphere
11158	15/02/11	X2.2	55	450	South
11166	09/03/11	X1.5	32	550	North
11283	06/09/11	X2.1	20	220	North
11520	12/07/12	X1.4	31	1320	South
11890	08/11/13	X1.1	54	920	South
12158	10/09/14	X1.6	13	420	North
12192	24/10/14	X3.1	114	2740	South

Table 4.1: The active regions studied. Sunspot area is given in millionths of heliospheric radius.

occurring on the 4th day, so that data are obtained 3 days before and 3 days after. These active regions are detailed in Table 4.1.

All of the active regions listed in Table 4.1 are from Solar Cycle 24. A solar cycle is approximately 11 years long and depends the change from a period of minimal activity, to its most active state, and back again. Activity of a Solar Cycle is determined by the number of sunspot regions. The minimum (and hence beginning) of Solar Cycle 24 was in December 2008. Activity increased with the advent of AR11158, where the first X-class flare of Solar Cycle 24 occurred (as listed in Table 4.1). The maximum occurred in April 2014, and the cycle is due to return to a minimum late 2019.

In most cases, the flare of interest in the largest flare of that region. However, in the case of AR11890, the flare is the second largest. This is due to the passage of the active regions across the disk centre: since RDA can only be performed successfully away from the limb, the active regions must be close to the disk centre at the time of flaring. Such criteria meant that many interesting active regions were not fit for exploration. Additionally, we focussed on active regions host to X-class flares. These are the most energetic type of X-ray flares, and thus thought to contribute more to sub-surface flow patterns (Komm *et al.* (2005)).

If the active region is too close to the limb, estimates cannot be found for all depths, and errors are introduced. Additionally, the ring pipeline often obtains zonal and meridional velocities for slightly different depths, meaning that interpolation is necessary in order to construct 3D plots. For each active region, we construct such a 3D plot of the zonal (U_x) and meridional (U_y) velocities in m/s and the sub-surface depth in Mm. It is important to note that these are total velocities, and therefore any background flows in the photosphere are included, as well as flows due to magnetic features. Figure 4.2 shows such information for active region 11158. The top left panel shows the

flows 3 days before and 3 days after the flare of interest, the top right 2 days before and after, the bottom left 1 day before and after, and the bottom right on the day of the flare of interest. Before is indicated in blue and after in pink.

However, it is clear that the signature of the flow changes as time progresses — that is, the shear of the flow shown in blue before flaring does not directly align with the flow in pink once flaring has occurred. Thus, it is sufficient to say that once a flare is emitted, the active region has undergone an irreversible flow change. Furthermore, the flows appear less sheared on the date of flaring, compared to flows before and after.

We plot the horizontal flows of active region 11166 in the same way in Figure 4.3. Comparing Figures 4.2 and 4.3, it is interesting to note that AR11166 appears to exhibit less shearing than AR11158. This could be due to the increased flaring activity of AR11158, even though they are of comparable area. The sizes of flows are comparable, most likely due to the active regions in Figures 4.2 and 4.3 existing at roughly the same point in the solar cycle.

The flows of active region 11283 are shown in Figure 4.4, in the same way as the previous two active regions. Table 4.1 shows that AR11283 is less than half the size of the previous two active regions — since the patch size is kept constant throughout our analyses, and flows are averaged spatially and temporally, this may be reflected in the flow patterns. Once again, it is clear to see the reduction in shear as the active region moves towards its largest flare, and the tendency to alter signature once the moment of greatest flaring has passed.

Since AR11283 is around six months after the one shown in Figure 4.3, and thus closer to the solar maximum, we expect to see some increase in flow magnitude. However, the magnitudes are comparable with those before, which could be a reflection of the size of the active region.

The increase in flow magnitude due to the size of active region is illustrated well in Figure 4.5, AR11520. This active region was almost 3 times the size of AR11158 during the date of flaring, resulting larger zonal and meridional flows. As expected, we also have less shear closer to the central date, with flow patterns almost completely reversed away from the surface 3 days after, compared with the flow patterns 3 days before.

Active region 11890, shown in Figure 4.6 is also a good example of increased flow magnitude due to the temporal position in the solar cycle. Here, flows are augmented in comparison to those in Figures 4.2, 4.3 and 4.4, though not as

large as those in Figure 4.5. This is because AR11520 was around 1.4 times the size of AR11890, thus covering a larger area of the sampling patch.

We previously noted that the flare examined in AR11890 is in fact the second largest, due to the active regions position on the disk. Hence, flow patterns here may be misleading, as the largest flare occurred three days before the given central date in Table 4.1. However, there appears to be the signature reduction in flow twist towards the central date, and re-twisting once again afterwards.

Figure 4.7 shows the velocity plots for active region 12158. This particular active region existed after the solar maximum, but close enough that the flows are still augmented compared to those in the first few Figures. AR12158 had only 13 flares, so the twisting seen in the first three panels could are particularly indicative of the changes in flow pattern leading up to the date of largest flare, where shear is at its lowest.

Finally, we consider the flows of active region 12192, the largest active region in Table 4.1. Unsurprisingly, the shear vastness of this active region is clearly shown in the magnitudes of the flows. In addition, AR12192 experienced nearly double the number of flares than the next most energetic region, at 114 flares. The combination of size and flaring activity leads to extreme shear, and unpredictability in true flow pattern. However, there is some evidence that the flow becomes more sheared after the flare has erupted, when comparing the pink points in the first three panels with the black points in the bottom right panel.

A conclusive remark would be that the flow patterns are significantly altered by the release of the larger flares in the active regions lifetime. However, the choice of time intervals may not be well-suited to comparison, even following the same format as in Jain, Tripathy and Hill (2015). Each of the X flares occurred at a different time interval during the day, so taking an average of each calendar day may lead to skew in the flow estimates when comparing two active regions. Hence, it makes sense to compare active regions using a bisection method for choosing time intervals, centring the flare of interest in the middle of the time series. This is detailed further in Section 4.4.2.

4.4.2 A concentrated study of the flaring nature of two active regions

In the previous section, the time intervals for RDA were chosen with respect to dates in the calendar. However, since flares do not occur at the same point in

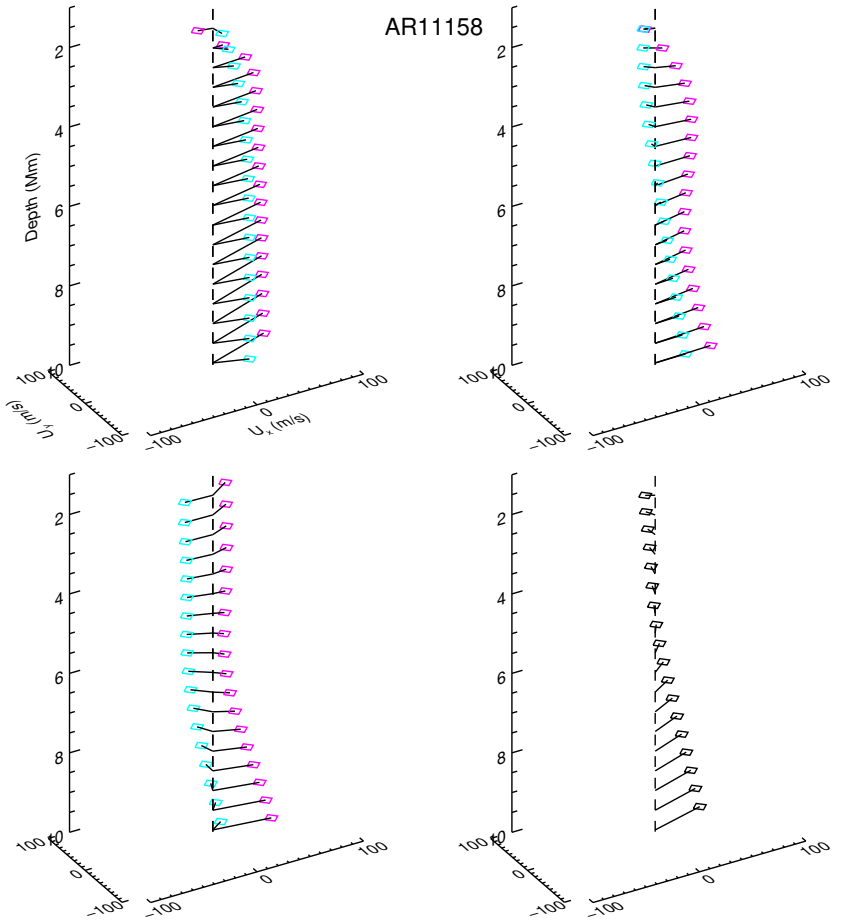

Figure 4.2: Plot of the horizontal velocities (U_x and U_y) in m/s against the subsurface depth in Mm of active region AR11158. The blue and pink circles denote "before" and "after" flaring in the top panel and the bottom left panel. The top panel indicates three days before and after (left) and two days before and after (right). The bottom left panel indicates one day before and after, and the bottom right panel shows flows for the day of flaring.

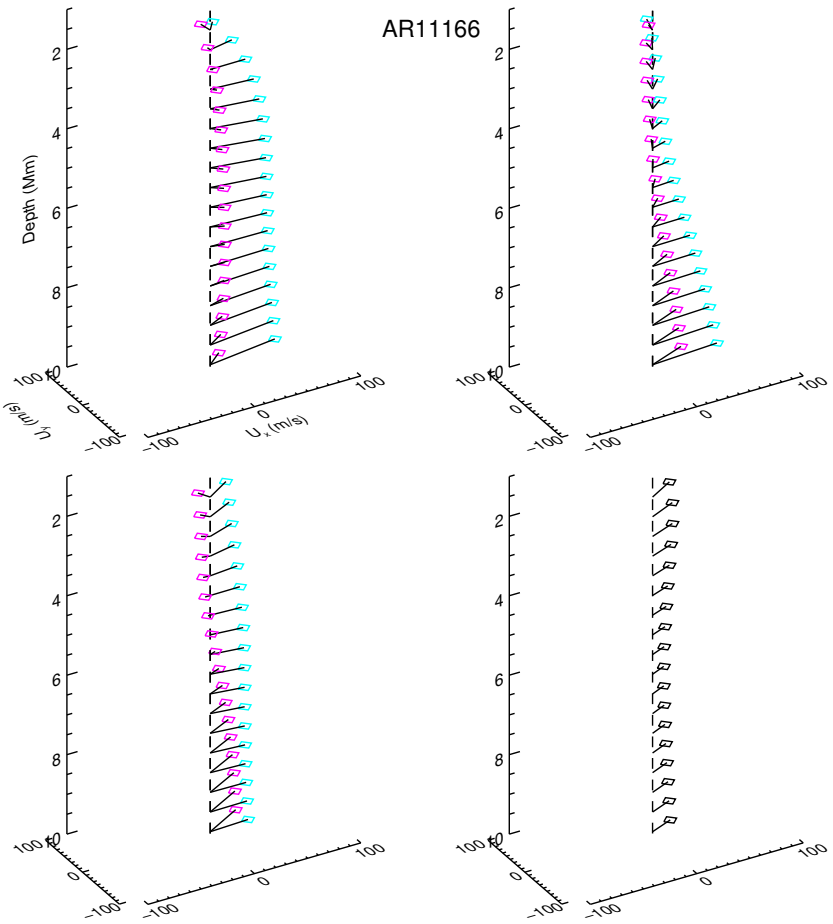

Figure 4.3: Plot of the horizontal velocities (U_x and U_y) in m/s against the subsurface depth in Mm of active region AR11166. The layout of the panels is the same as in Figure 4.2.

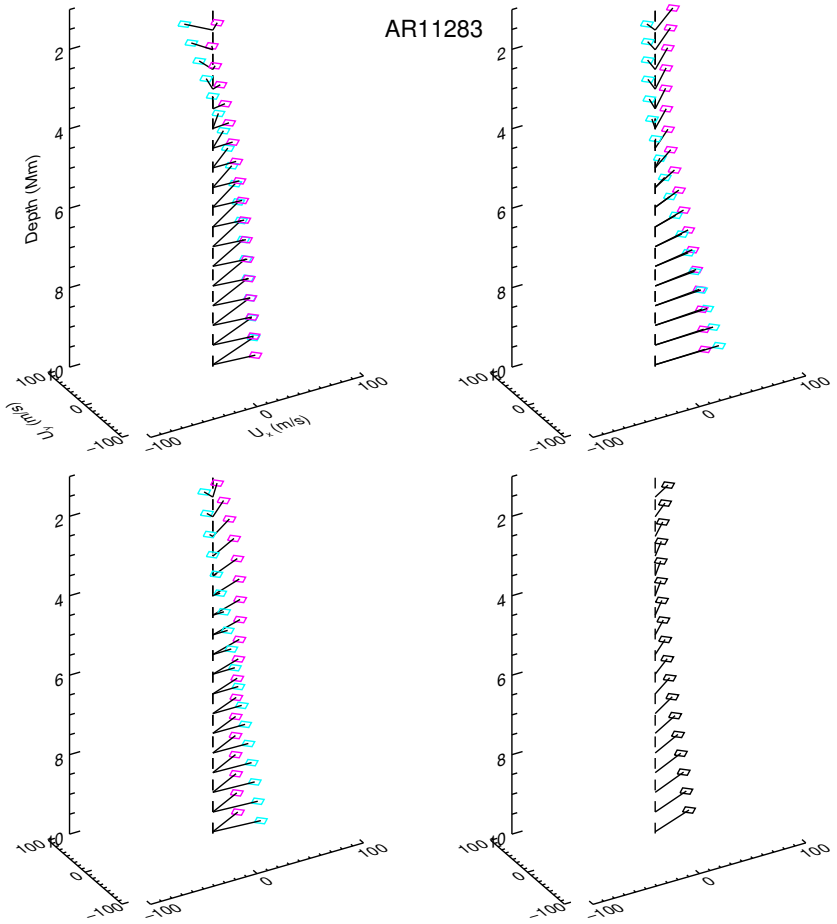

Figure 4.4: Plot of the horizontal velocities (U_x and U_y) in m/s against the subsurface depth in Mm of active region AR11283. The layout of the panels is the same as in Figure 4.2.

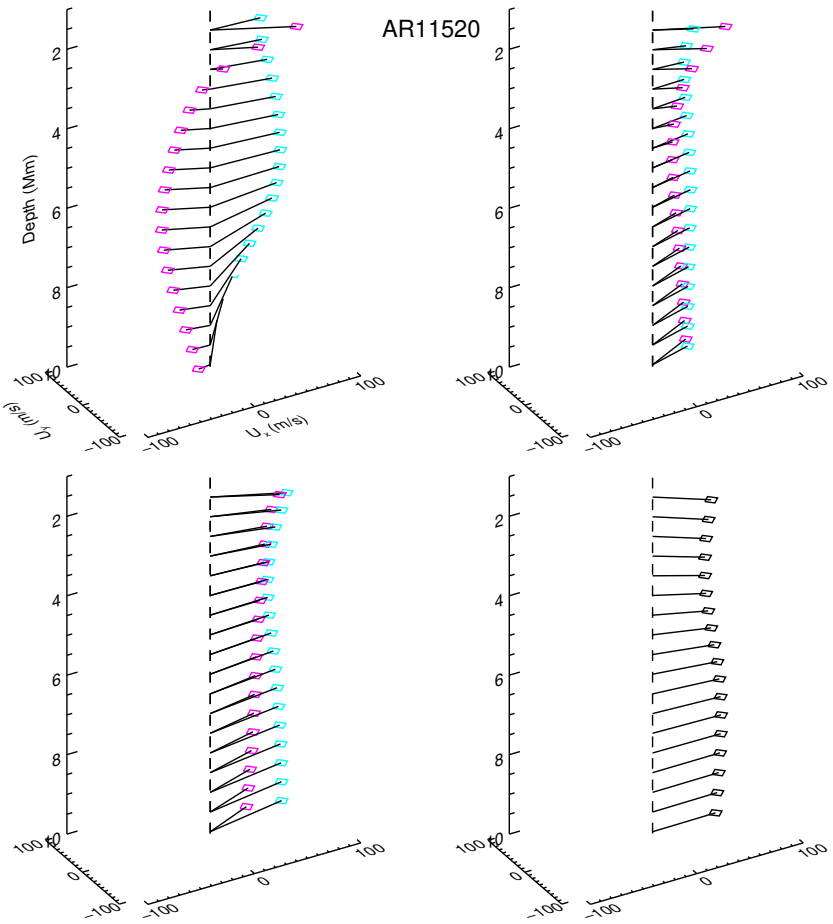

Figure 4.5: Plot of the horizontal velocities (U_x and U_y) in m/s against the subsurface depth in Mm of active region AR11520. The layout of the panels is the same as in Figure 4.2.

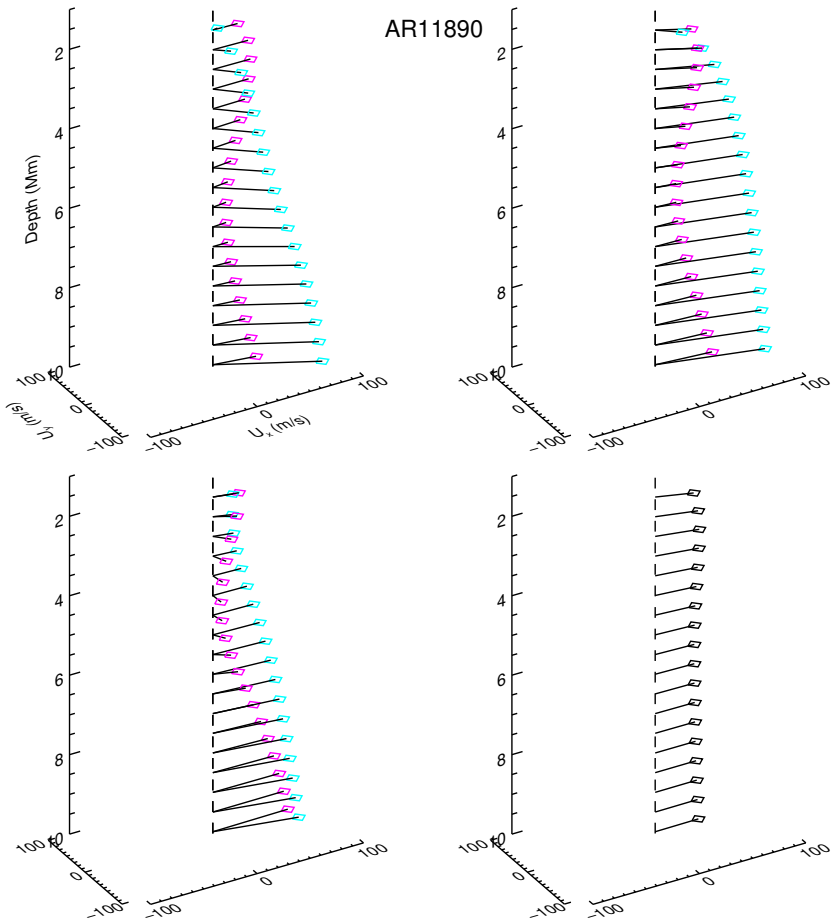

Figure 4.6: Plot of the horizontal velocities (U_x and U_y) in m/s against the subsurface depth in Mm of active region AR11890. The layout of the panels is the same as in Figure 4.2.

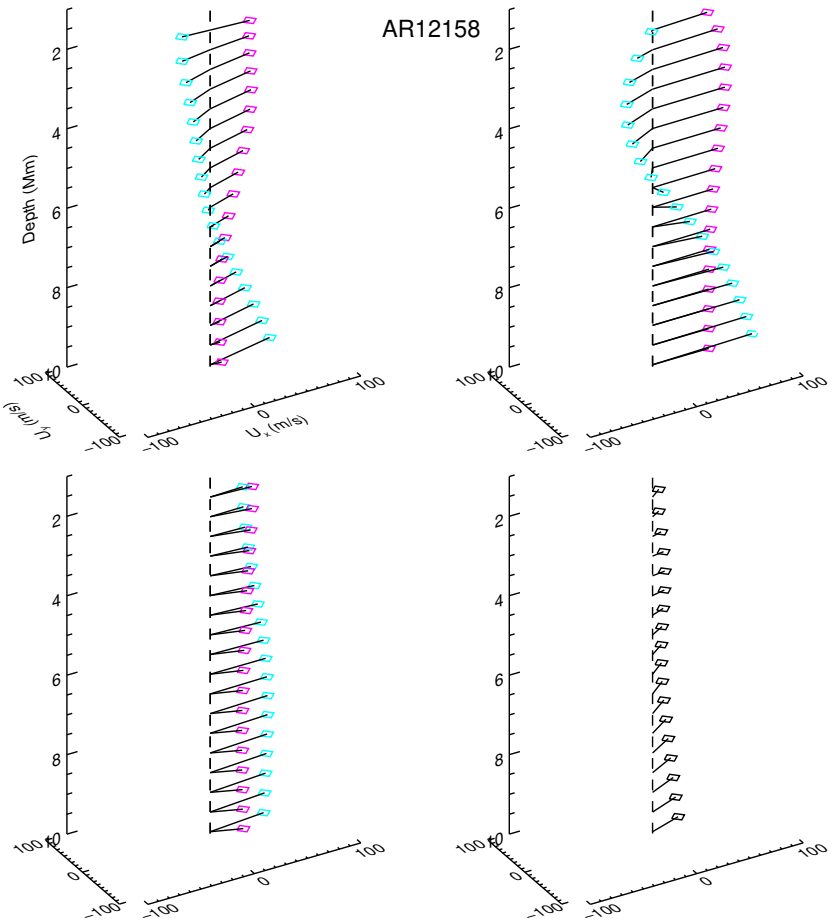

Figure 4.7: Plot of the horizontal velocities (U_x and U_y) in m/s against the subsurface depth in Mm of active region AR12158. The layout of the panels is the same as in Figure 4.2.

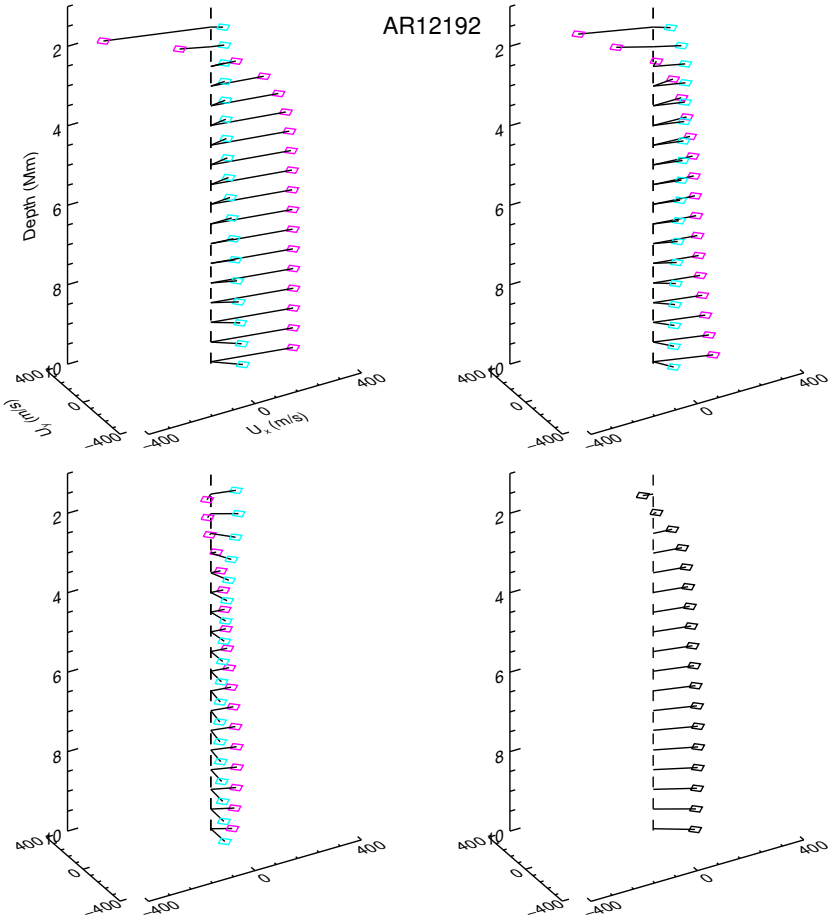

Figure 4.8: Plot of the horizontal velocities (U_x and U_y) in m/s against the subsurface depth in Mm of active region AR12192. The layout of the panels is the same as in Figure 4.2.

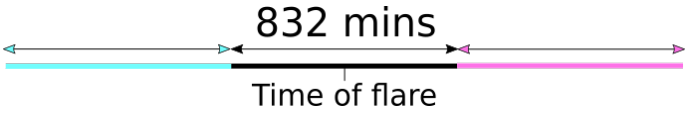

Figure 4.9: Illustration of time series intervals, for the case of 832 minutes. Blue indicates the time interval before flaring, black during and pink after.

the day, and RDA uses temporal averaging in order to calculate the flows, the true nature may be skewed for each active region comparatively. To combat this, we devise a method of bisection. In each case, we centre the time series on the flare of interest. For example, one of the time series lengths is a ring day i.e. 832 minutes (half a "ring day"). Thus, the time series is sampled such that the flare is seated in the centre of the 832 minutes. We repeat this for 1664 minutes (a "ring day") and for 20 hours (1200 minutes), since this is approximately halfway between 832 and 1664 minutes. Then, the same length of time series is sampled before and after the time series seated on the flare of interest, so that there are three consecutive time series. This is illustrated in Figure 4.9, where blue signifies the time interval before, black during and pink after.

In particular, we compare the flows of two active regions: AR11166 and AR11283. Both active regions flared in approximately the same area on the disk centre, and existed at a similar time in the solar cycle. We investigate the flow patterns around the time of their largest flares, by plotting their total horizontal velocities (in m/s) in sub-surface depth (Mm).

The active region AR11166 first emerged into view on the 2nd of March 2011, and produced 32 X-ray flares (25 C-class, 4 M-class and 1 X-class). The largest flare emitted was an X1.5 flare on the 9th of March, between 23:13 - 23:29. Centring the time series on the flare, we produce Figure 4.10, where the zonal (U_x) and meridional (U_y) velocities in m/s, denoted by solid lines and dashed lines respectively, are plotted against sub-surface depth in Mm. The first panel in Figure 4.10 shows the horizontal velocities for an 832 minute time series centred at the time of flaring. The middle and bottom panels are the same as the top panel, but for 1200 minutes and 1664 minutes. As in Section 4.4.1, the velocities are of the total flow in that region, so contain background flows as well as those contributed by the active region.

In the top panel of Figure 4.10, as time progresses, the zonal velocities become suppressed near the surface, but become augmented much further away. The meridional velocities remains similar close to the surface before and during the flaring period, but decreases soon after. However, far away from the

surface, the meridional velocities decreases at the time of flaring and increases after.

Considering now the middle and bottom panels, we note that the behaviour of the flows seems quite different. This is because the time intervals chosen overlap, meaning that the 1200 minute and 1664 minute velocity curves during the flare contain flows from the 832 minute series before and after. Hence, the temporal averaging has contributed significantly to the behaviour of the flows. The meridional velocity in the middle and bottom panels remains approximately the same magnitude near the surface before, during and after the flare, but this behaviour differs at further depths. The minimum for the zonal velocities in the top panel is shifted by contributions from the before and after zonal velocities, indicated by the middle and bottom panels.

The second active region we study in detail is AR11283. Emerging on the 30th of August 2011, this active region was about half the area of AR11166. It produced 20 flares in total (13 C-class, 5 M-class and 2 X-class), the largest of which being X2.1 between 22:12 and 22:24 on the 6th September. The active region flows are plotted in the same was as in Figure 4.10.

Once again, we note that the zonal flows are more spread out close to the surface in the first panel, compared with the flows in the middle and bottom. It's clear that the zonal flows exhibit a stronger nature than the meridional flows before the flare occurs, but once the flare is emitted zonal flows are only diminished close to the surface. However, in the same time frame, the magnitude of the meridional flows increases. Further away from the surface, zonal flows are more similar in magnitude when averaged over longer time series as in the middle and bottom panels.

Compared with the flows in Figure 4.10, the flows appear to be less affected by their sub-surface depth. Since flows are estimated using Doppler shift parameters at the surface, this could be due to the size of the active region. AR11283 is much smaller than AR11166, and averaging across spatial values in patches of the same size means that there is less contribution to estimated flows by AR11283 than AR11166. This is because there is a higher ratio of quiet Sun to active region in the patch taken for AR11283 than for AR11166. To this end, it is prudent to choose a patch size smaller for AR11283, so that the quiet region does not dampen the effects of the active region - this is our approach in section 4.4.3.

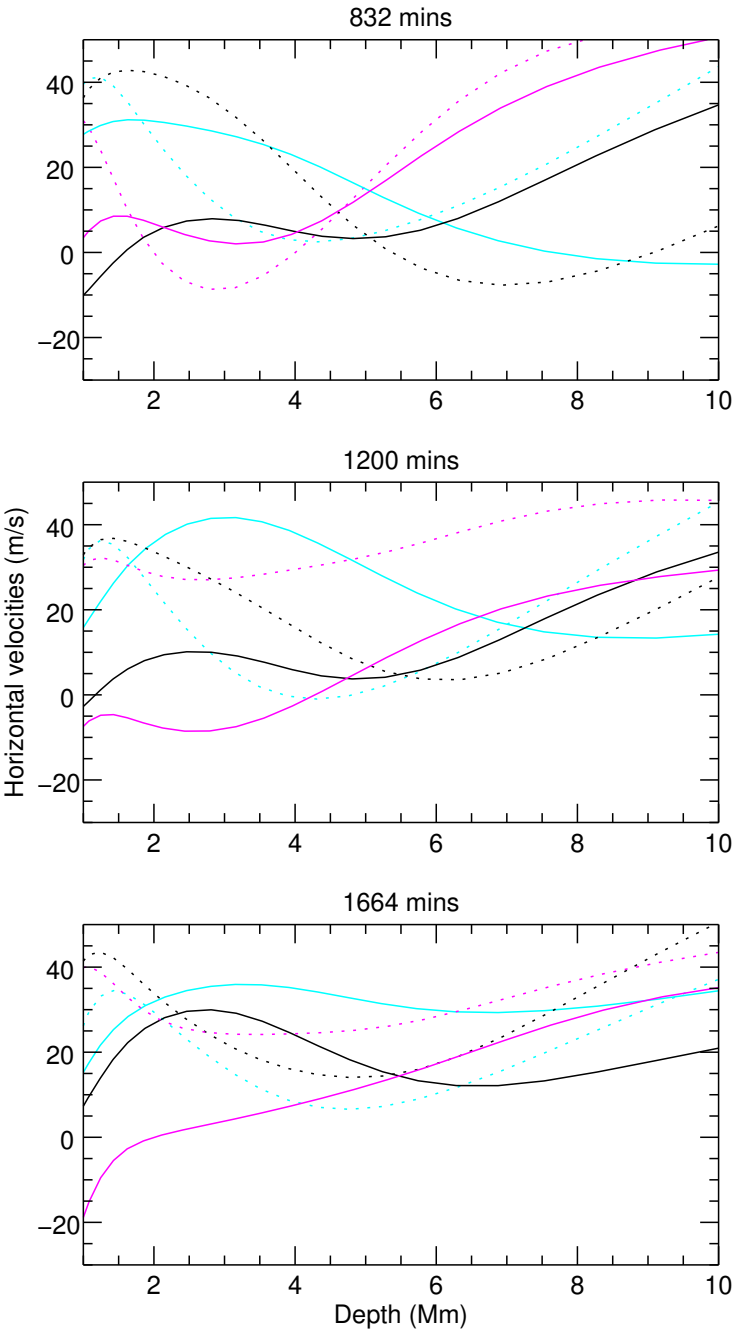

Figure 4.10: Plot of the horizontal velocities (U_x, indicated by a solid line, and U_y, indicated by a dashed line) in m/s against the subsurface depth in Mm of active region AR11166. Here, the time series are of length 832 minutes (top), 1200 minutes (middle) and 1664 minutes (bottom), which are centred on the time of flaring. The colours follow the same pattern as in Figure 4.9.

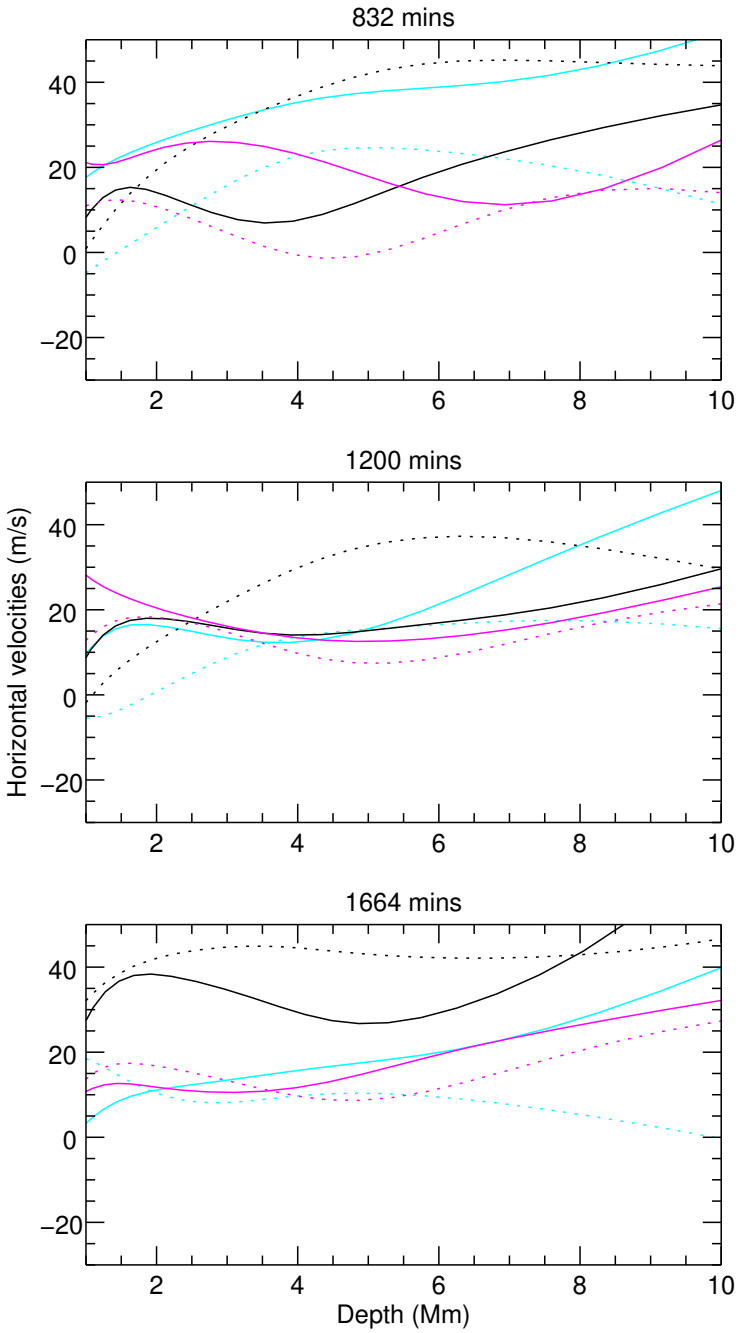

Figure 4.11: Plot of the horizontal velocities (U_x, indicated by a solid line, and U_y, indicated by a dashed line) in m/s against the subsurface depth in Mm of active region AR11283. Here, the time series are of length 832 minutes (top), 1200 minutes (middle) and 1664 minutes (bottom), which are centred on the time of flaring. The colours follow the same pattern as in Figure 4.9.

4.4.3 A comparison of active regions across the first half of Solar Cycle 24

As previously mentioned, the Solar cycle is the approximate 11-year variation of activity on the Sun. The maximum corresponds to the point in the cycle where sunspot activity as at its highest, and the minimum is when the sunspot activity is at its lowest. Komm *et al.* (2014) (also see Komm *et al.* (2015); Komm *et al.* (2017)) investigated the variation of subsurface flows during the Solar cycle. Strips of zonal flow which are of higher magnitude than average appear around three or four years before magnetic activity starts, and corresponding meridional velocities exhibit motion more towards the poles than average. The amplitudes of meridional velocities are greater during solar minimum. The locations of higher magnetic activity exhibit convergent flows between 0-10Mm, whereas the quieter regions are host to divergent flows.

Since active regions are comprised of sunspots, it follows that there could be a link between active region activity at different points in the solar cycle. Hence, we examine the subsurface flows of twelve active regions, listed in Table 4.4.3. This table contains the seven ARs listed in Table 4.1, and has information about the peak time of the flare, the total number of flares and their classification (C, M or X), the coordinate location on the disk, whether they produced a coronal mass ejection (CME), and whether they had rotating sunspots. Of these twelve active regions, ten are regions which produced X-class flares, and two did not produce any X or M-class flares during the time series studied, for comparison.

The time series length chosen in 1664 mins, since this is the standard time series length studied in RDA literature. This is centred on the time of flaring. In the previous section, errors were introduced by choosing a time series that was too short. Additionally, we noted that averaging over the spatial parameters of the patch can be problematic for active regions which are not of comparable size. AR11283 and AR11793 are much smaller than the others sampled, so patches of around $12^\circ \times 12^\circ$ are tracked - patches much smaller can introduce spurious errors.

The large-scale flows are then plotted with quiet flows subtracted at around the same latitude to show contribution to large-scale flows by the active region. The quiet data is taken from 2008, since this was a period of low solar activity, and for each AR we take five 1664 minute series at approximately the same time in the year, to take into account the yearly variation in the tilt-angle of the Sun, known as the B_0 angle (Zaatri *et al.* (2006)). It is important to choose

AR #	Date	X-type duration	X-type size	Flare total			Sunspot area	Sunspot number	Location	CME	Rotating
				C	M	X					
11158	2011 Feb 15	01:44 - 02:06 UT	X2.2	48	6	1	450	36	S19W15	Y	Y
11166	2011 Mar 9	23:13 - 23:29 UT	X1.5	27	4	1	550	55	N11W11	N	N
11283	2011 Sep 6	22:12 - 22:24 UT	X2.1	13	5	2	220	29	N14W19	Y	Y
11429	2012 Mar 7	00:02 - 03:49 UT	X5.4	32	14	2	1120	28	N18E29	Y	Y
11520	2012 Jul 12	15:37 - 17:30 UT	X1.4	26	5	1	1320	60	S15W02	Y	Y
11890	2013 Nov 8	04:20 - 04:29 UT	X1.1	46	5	3	920	59	S11E09	Y	Y
11944	2014 Jan 7	18:04 - 18:58 UT	X1.2	44	7	1	1415	116	S09E00	Y	Y
12158	2014 Sep 10	16:59 - 22:40 UT	X1.6	11	1	1	420	29	N15E06	Y	Y
12192	2014 Oct 24	20:50 - 00:14 UT	X3.1	73	35	6	2740	66	S14W16	N	N
12242	2014 Dec 20	00:11 - 00:55 UT	X1.8	51	6	1	1080	34	S19W31	Y	Y
11711	2013 Apr 5	N/A	N/A	2	0	0	580	19	S19E04	N	N
11793	2013 Jul 19	N/A	N/A	2	0	0	310	18	N21E13	N	N

Table 4.2: The ARs and X-type flares studied, along with relevant morphological information. The sunspot area is given in millionths.

longitudes and latitudes close to the location examined during flaring since the Dopplergram images are based on the line-of-sight, and projection effects can be introduced. The five data sets are then averaged to remove systematic errors. Using RDA, the sub-surface flows for each active region are obtained, and are illustrated in Figures 4.12-4.14, in the form of three-dimensional plots of zonal and meridional velocities in depth. As in Section 4.4.2, the flow patterns of the AR at for three time intervals are examined - 1664 minutes before (left), during (centre) and after (right) flaring. Sample quiet zonal and meridional flows of two ARs (Northern, black; Southern, red) are demonstrated in Figure 4.15

Considering the first panel of Figure 4.12 (AR11158), it is immediately clear that the flow patterns change shape in time, similar to the flows in the section 4.4.1. However, since we are now centring time series on the peak time of the flare, the flows have changed significantly. The middle panel shows that during flaring, the magnitude increases, with a maximum around 4-5Mm. The flows in the left hand panel, before the flare, are more strongly sheared than those during and after flaring. Using SDO/HMI intensity imaging, Jiang *et al.* (2012) investigated the rotation of sunspots within AR11158. This rotation started around 20 hours before the flare erupted, contributing to the flows in the left hand panel and middle panel, coming to a sudden halt approximately an hour after the flaring finished (around half way through the middle time series). This lack of sunspot rotating following flaring could explain the lack of shear in flows in the right panel.

The next row in Figure 4.12 corresponds to AR11166. Table 4.4.3 indicates that this AR did not have rotating sunspots, and did not produce a CME, unlike AR11158. There is a distinct change in shear between the first and second panels, though this cannot be a manifestation of the rotation in flows. Hence, this shearing is most likely due to changes in the magnetic field configuration, as in Jain *et al.* (2017). There, the strong confined magnetic field and its reconfiguration were deemed to be the cause of flaring. After flaring, there is little change in the shape of the flow in depth.

AR11283, as described in section 4.4.2, is smaller than most of the other ARs considered. Therefore, it was necessary to choose a patch size of $12^\circ \times 12^\circ$. The magnitudes in flows are much smaller than those in AR11158, which had a similar morphology. However, the flows before flaring are extremely sheared, with this twist rapidly changing in time, becoming reversed after flaring.

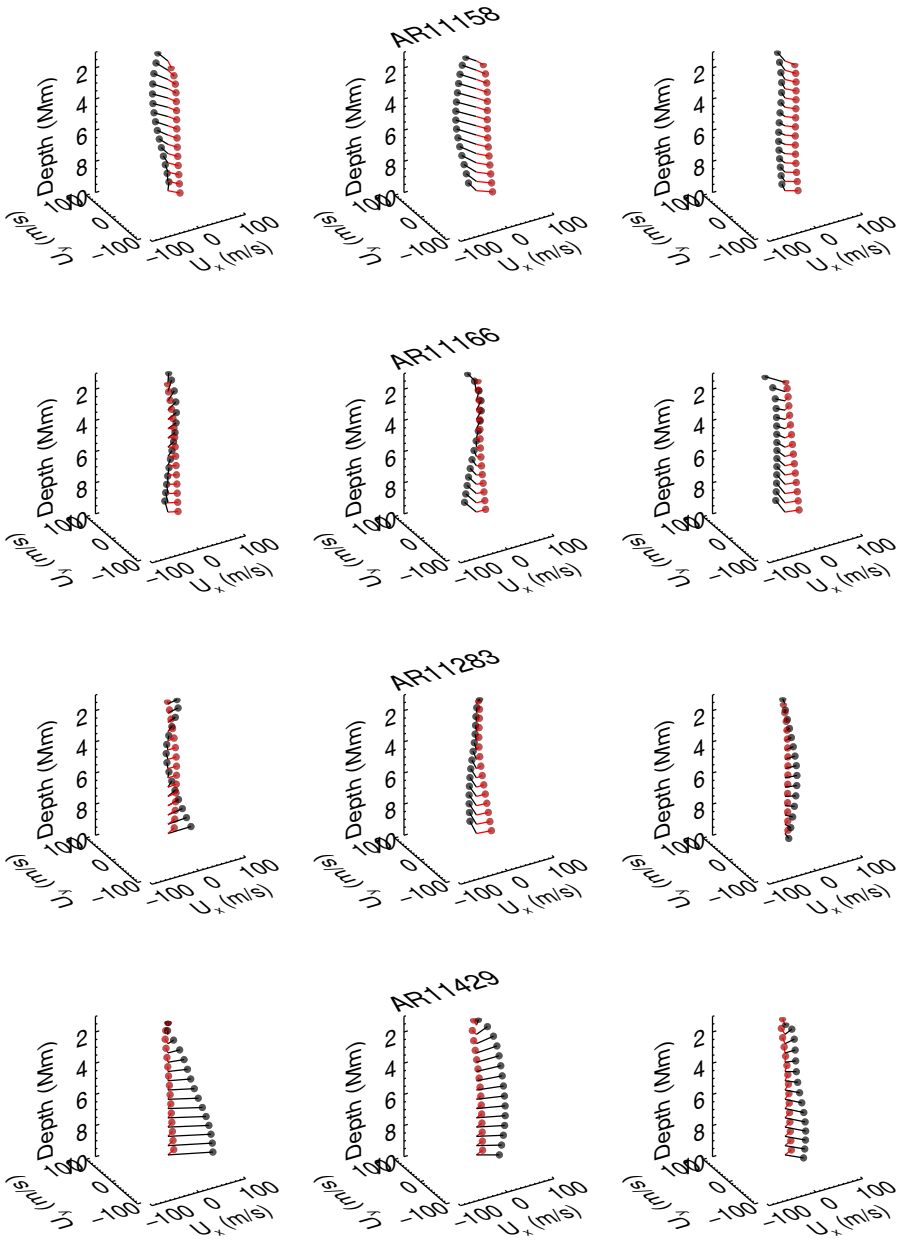

Figure 4.12: The horizontal flows U_x and U_y in m/s plotted against sub-surface depth (Mm), for the first four active regions in Table 4.1. The left panel shows the flows the day before, the middle shows the day of flare of interest, the right panel shows the day after. The red circles indicate the quiet region data.

In the final panel of Figure 4.12 are the flows for AR11429. The flows before flaring are much higher in magnitude than during and after flaring, which may be the cause of the strong flare which was released soon after ($X5.4$). During flaring, as in AR11158 (top panel), the flows are augmented between 4-5Mm. Similarly, the flows change once again after flaring, possibly due to the sunspot rotation.

Though the flows in the first panel (AR11520) of Figure 4.13 show strong shear, they do not change as rapidly over time as the previous ARs which produced CMEs and exhibited sunspot rotation. Despite being an X-type flare, it is not as high in magnitude as those in AR11158, AR11283 and AR11429, which could explain the comparatively small changes in shear and magnitude across all time series.

AR11711 and AR11793 did not exhibit any X-class flares in their lifetimes, but are plotted in Figure 4.13 for comparison with the other ARs. Both ARs have some changes in flow throughout time, but their magnitudes stay relatively similar. In the case of AR11793, some of the changes in magnitude could be due to its proximity to the limb in the early time series, or errors introduced when decreasing the patch size to $12^\circ \times 12^\circ$ as for AR11283.

The flows of AR11890 are similar to those of AR11283 in time — they are not especially large in magnitude but they change rapidly before flaring to during flaring. Once flaring has taken place, there is not much change in the flows in depth. Comparing these flows to those in AR11793, there is not much difference in flow patterns, which could mean that magnetic fields were more responsible for the flare production than the motion of flow beneath the AR. Historically, AR11890 also produced an $X3.3$ flare on the 5th Nov 2011, so the production of an $X1.1$ three days later may signify the release of leftover energy stored.

The top panel of Figure 4.14 illustrates the zonal and meridional velocities of AR11944. As with AR11520, though the magnitudes of flows do not differ much in time, the flows are sheared, and the AR itself is large in area (see Table 4.4.3). AR12158, however, was around a third the size of AR11944, and produced a higher magnitude flare ($X1.6$, as opposed to $X1.2$). Examining the second panel of Figure 4.14, it is clear that the flows become extremely sheared in depth during flaring, before reversing as in AR11283. This is likely an explanation of the flare's magnitude.

The largest flows of the AR set, AR12192 was also the largest in area. Illustrated in the second to last panel of Figure 4.14, the flows sheared for

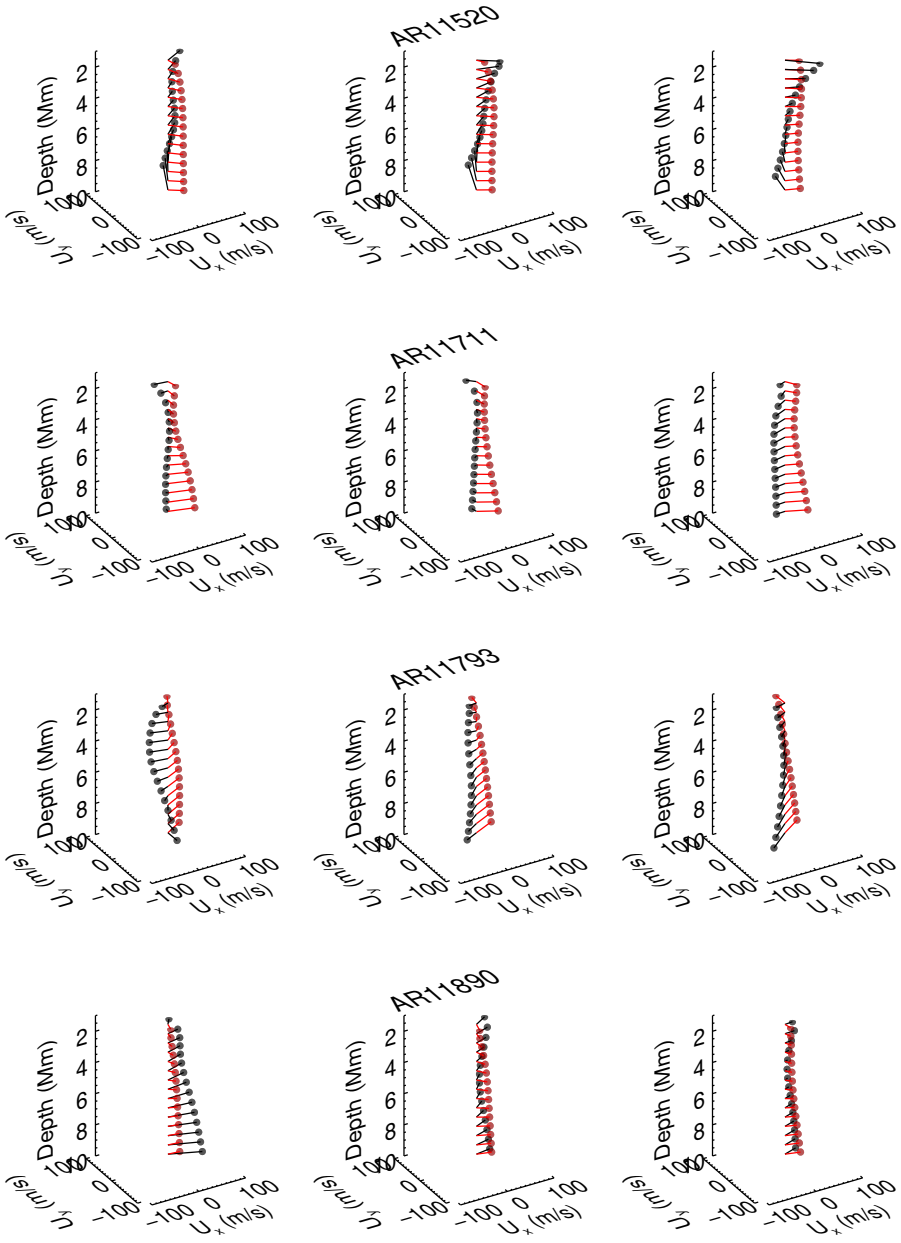

Figure 4.13: The horizontal flows U_x and U_y in m/s plotted (black) against sub-surface depth (Mm), for the central four active regions in Table 4.1, as in Figure 4.12. The red circles indicate the quiet region data.

all time series, with the flows changing pattern in depth quite rapidly before and during flaring, with the shear remaining almost constant after flaring has occurred. This behaviour is similar to the flows during and after flaring of AR11166 in Figure 4.12. With larger-than-average flows, the last panel of Figure 4.14 shows the flows beneath AR12242. The shearing demonstrated in all three time series changes radically over the duration, with high magnitude flows in depth for each time series. At around 4-5Mm, flows during flaring are at a maximum. The high magnitude flows following shearing are quite atypical, especially considering the size of the active region. However, during the final time series, the active region was located very close to the boundary for which Ring Diagram Analysis can be most accurately employed. Hence, it follows that some uncertainty in flows could have been introduced.

4.4.3.1 Emergence of ARs, CME production and rotating sunspots

The comparison of features such as whether the ARs were emerging or decaying, the production of CMEs, or the existence of rotating sunspots could be used to explain the differences in sub-surface flows of ARs which otherwise appear similar.

The magnetic activity index (MAI) for each active region in Table 4.4.3 for 5 days as they pass across the Sun's disk are shown in Figure 4.16. The grey box in each plot indicates the longitudes examined in the subsurface flow Figures 4.13-4.15, and the dashed line indicates the MAI at the time of flaring. MAI can be used to determine whether the active regions were emerging or decaying at the time of flaring. In most cases, ARs decayed once flaring had occurred. However, there were differences in when the flaring activity occurred i.e. when the active region was still evolving or had started decaying. Using these criteria, AR11158, AR11166 and AR111429 all flared whilst emerging, though AR11429 carried on evolving following the production of the flare studied. Conversely, AR11283, AR11520, AR11944, AR12192 and AR12242 all flared whilst decaying. Finally, AR11890 and AR12158 did not exhibit much variance in MAI before, during or after flaring. Referring to Figures 4.13-4.15, it is clear that the MAI values in Figure 4.16 do not clearly show any link between those which are emerging or those decaying at the time of flare production. Note here that the two non-flaring ARS (AR11711 and AR11793) both have MAI around 100G throughout their passage across the disk. This increase in magnetic activity at each region explains well the increased magnitude subsurface flows in Figure 4.14.

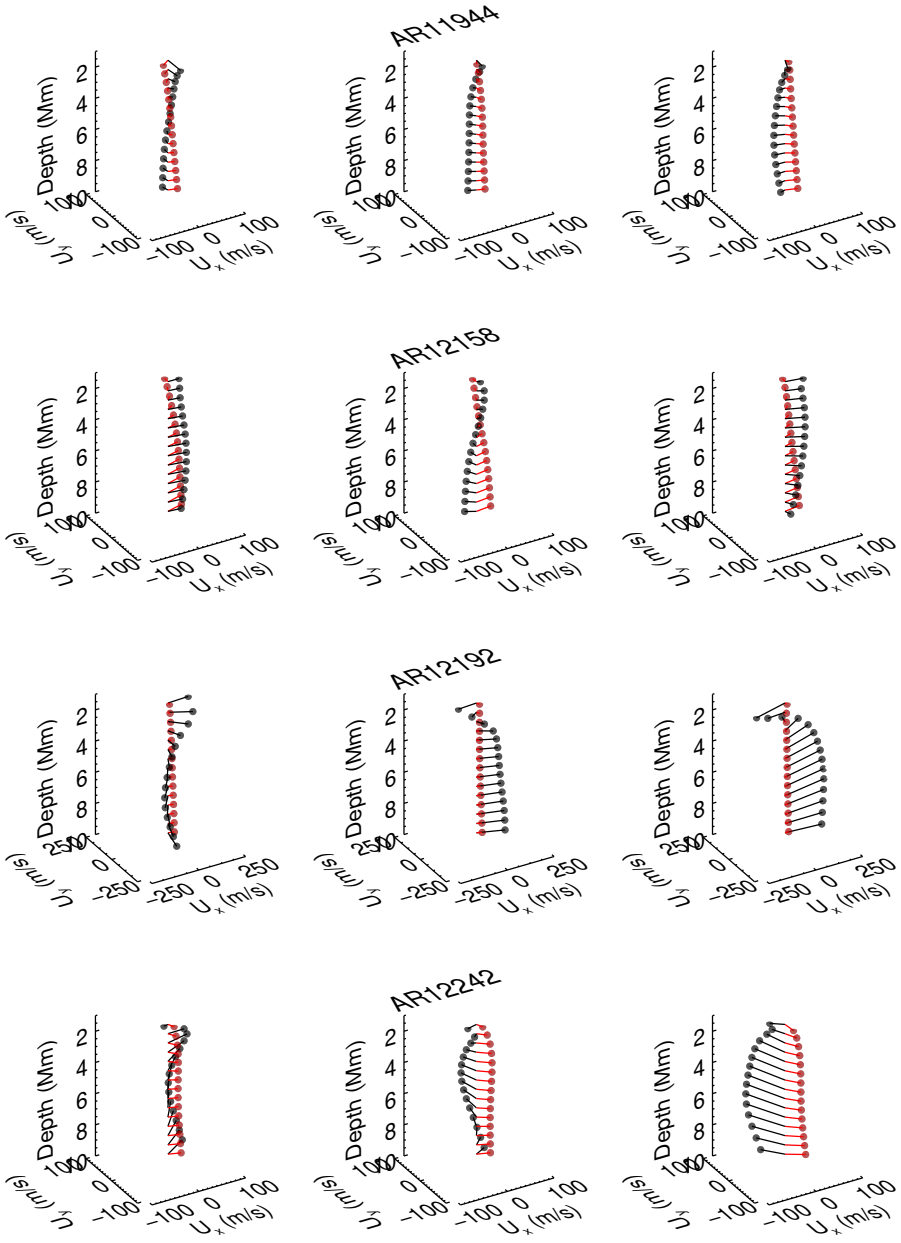

Figure 4.14: The horizontal flows U_x and U_y in m/s plotted (black) against sub-surface depth (Mm), for the last four active regions in Table 4.1, as in Figure 4.12. The red circles indicate the quiet region data.

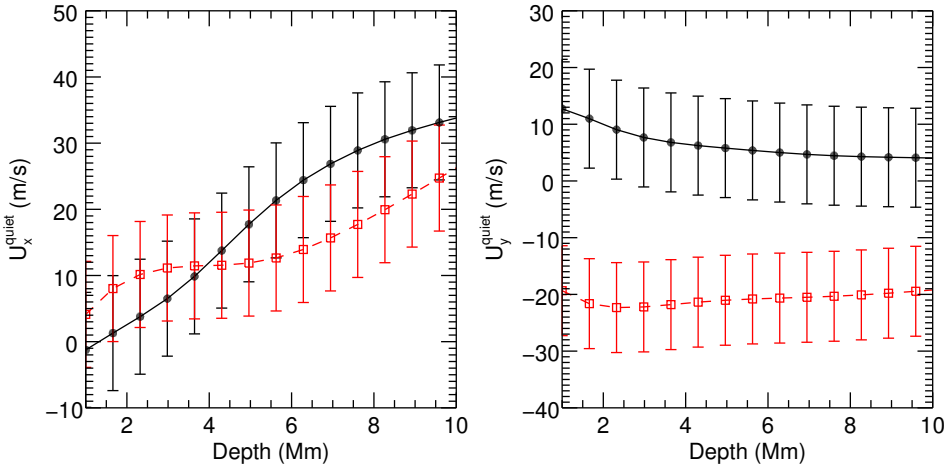

Figure 4.15: Sample quiet flows U_x and U_y in m/s plotted against sub-surface depth (Mm), for the Northern (black) and Southern (red) hemispheres.

Active regions can be further categorised into two types of regions: those which produced a coronal mass ejection (CME) and those which did not. We refer to those producing CMEs during flaring as "eruptive" active regions and otherwise refer to "confined" regions (Cliver (1995)). The ARs in Table 4.4.3 then form three distinct groups: the eruptive regions (AR11158, AR11283, AR11429, AR11520, AR11890, AR11944, AR12158 and AR12242), the confined regions (AR11166 and AR12192), and the non-flaring regions (AR11711 and AR11793). We note here that the eruptive active regions all possessed rotating sunspots, whilst the confined regions did not.

Comparing the sub-surface flows of the eruptive ARs (Figures 4.13-4.15), though all regions appear to show changes in flow pattern across the three time series, there are not distinct features which link each AR. On the other hand, there appears to be little change in shearing during and after flaring for the two confined active regions, possibly explained by the absence of sunspot rotation. However, the presence of rotating sunspots does not always mean that the sub-surface flows below such active regions exhibit shearing motions.

4.4.3.2 Size of active region and average sunspot area

There are vast differences in the size of each AR and the number of sunspots the active regions host. In the case of AR12192, the largest of the active regions studied, the large magnitude flows appear to coincide with the its vastness. However, AR12242 is host to flows of a much larger magnitude than AR11944, despite being a much smaller active region. Consider instead the

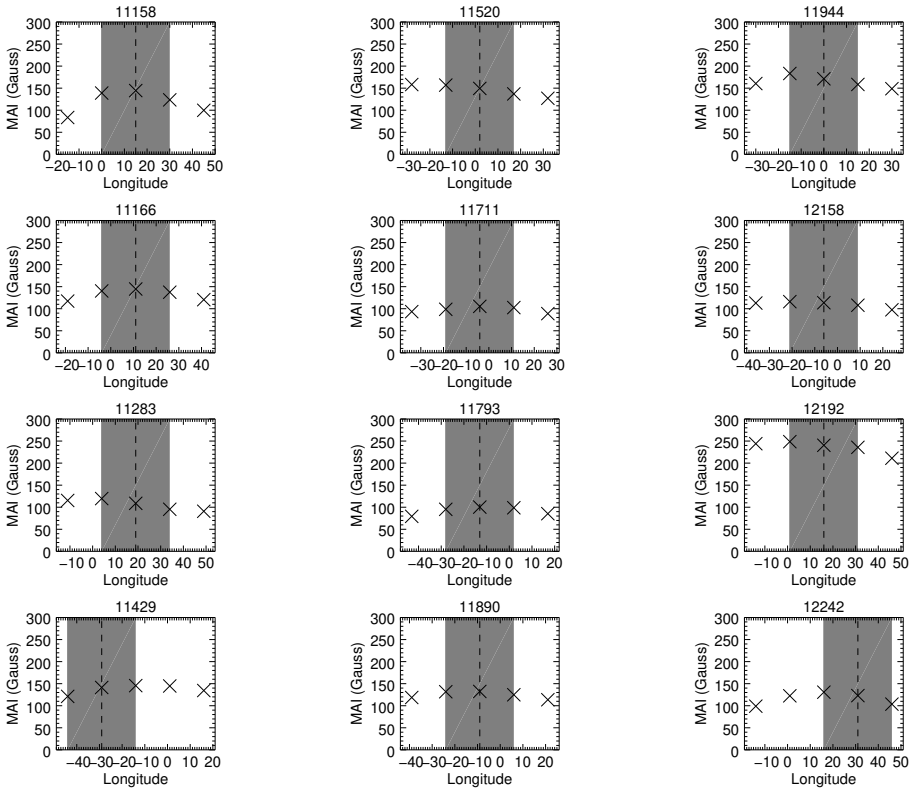

Figure 4.16: The MAI against the longitude of the AR as is progresses across the Sun's disk in time. The vertical dashed line indicates the position of the active region at the flare of interest.

average sunspot area of each active region. Doing so, we see that active regions with a large average sunspot area exhibited much more twisting in depth and through time than those with smaller average sunspot area. The magnetic field lines in regions with larger sunspots require a significantly greater source of rearrangement than those with smaller sunspots, and hence show more shear in flows.

4.5 Summary

By using the techniques of Ring Diagram Analysis first introduced in Hill (1988), the horizontal flows under active regions may be studied using Dopplergram data. The technical details of this process were detailed extensively in Section 4.3. In particular, the use of data from the ground-based telescope network GONG (see Section 4.3.2) is promoted, which provides Dopplergram and Magnetogram images (to name but a few) for use with RDA and other

helioseismological techniques. The RDA technique in conjunction with flaring active regions, as in Jain, Tripathy and Hill (2015), is applied initially to 7 active regions across 7 calendar days (i.e. 1440 minutes), with the flare of interest occurring at some point on the central day. All active regions were selected from the first half of the Solar Cycle. Since this did not account for the time of flaring within each of the centralised calendar dates, some of the shearing information may have been lost due to averaging the time series asymmetrically. Hence, Sections 4.4.2, 4.4.3.1 and 4.4.3.2 saw the time series analysis centred on the time of flaring.

The effects of tile size and time series length of the data were discussed in detail throughout the Chapter, demonstrated fully in Section 4.4.2. By taking time series which are too long, effects seen during flaring may be smoothed out by the inclusion of time periods where the region was less active, leading to flows which appear more sedentary than expected. Similarly, patches too large in comparison to the active region of interest may average out the activity by taking too much of the surrounding quiet region. This was counteracted by removing the estimated "quiet" flows from the estimated flows, to simulate the removal of the effects of the surrounding quiet region.

By introducing more active region data in Section 4.4.3, it was demonstrated that the amount of shearing below an active region varies drastically, even when comparing two active regions of comparable flare size. Even when comparing those which also hosted a CME or not, there appeared to be only small similarities. However, by comparing the size of the average sunspot area (i.e. the size of the active region in relation to the number of sunspots present), it was shown that there was a possible correlation with the amount of twisting present in the flows. It was concluded that this was due to the compactness of the magnetic field lines, and thus the amount of rearrangement required before magnetic reconnection could be easily achieved. Similarly, we see that regions which did produce flares had raised magnetic activity compared to those which did not.

All of the above analyses were performed using GONG data. Since this is ground-based data, it may be interesting to see if similar data analysis carried out on data obtained from space instruments yield similar findings. For example, the analyses could be repeated using HMI Dopplergram data obtained by the Solar Dynamics Observatory, though this requires extensive calibration for use with RDA. The advantage here would also be the much higher resolution imaging obtained using HMI with respect to the GONG

network. Additionally, the advent of the Daniel K. Inouye Solar Telescope (due for completion within the next two years), ground-based observations will be achieved at a much higher resolution and more readily calibrated for use with the RDA technique.

CHAPTER 5
Conclusions and future work

5.1 Overview

The current thesis is focussed on understanding two main aspects of solar coronal active regions, the coronal loop oscillations and their excitation mechanisms. Firstly, the loop oscillations triggered by flaring events in such active regions, and, in particular, the propagation of waves in the multi-dimensional waveguides present. Secondly, the changes in the flow patterns below the surface of the active region. The footpoints of the loops are believed to be anchored below the surface which can play a part in the loop oscillations. Hence, studying the plasma properties in and around the active region, both above and below the surface, is important for understanding the full picture of the solar active region. A brief background of the solar structure was covered in Chapter 1, paying special attention to loop arcades, active regions and associated features on the photosphere and in the lower corona. The basic introduction to magnetohydrodynamics and magnetohydrodynamic waves was then covered, before suggesting some implications for observations based on our analytical modelling. Finally, we covered helioseismology, and the way we can use it to "see" cavities inside the Sun which are otherwise "invisible".

Chapters 2 and 3 concentrated on the mathematical modelling of loop oscillations in 3D waveguides. In both cases, eigenfunctions and frequencies were examined, and the effects of density structure changes explored. However, Chapter 2 presented a 3D model in Cartesian coordinates, with a vertically stratified density distribution. Both Alfvén and fast mode solutions were calculated for different ratios of magnetic and gas pressure scale heights. Preferential excitation of modes following application of a perturbation was also studied, in the context of both types of modes. Finally, the addition of a small region of differing density close to the footpoints of the structure was examined for fast mode solutions, and changes to eigenmodes demonstrated.

Constructing a 3D wave model in cylindrical coordinates, a coronal arcade model formed by a density interface for a semi-circular geometry was proposed in Chapter 3. The need for density variation in radius rather than just in the vertical direction was noted, since the loops are expected to be of similar density from the loop footpoint through to the loop apex, and the sharp increase in density at the interface reasoned through observations of arcade structures. Eigenfunctions, radial and axial velocities, and polarisation of waves was determined for some interface location, following the derivation of a dispersion relation. By extending the model and introducing a second density interface, a model more representative of observational properties of coronal loops was explored.

Diving below the surface, Chapter 4 used observations of Doppler shifts at the photosphere to determine subsurface flows of active regions. Using Ring Diagram Analysis, flows of different durations were compared for multiple active regions, before examining 12 flaring and non-flaring regions from Solar Cycle 24. In each case, background flows were removed so that the true nature of flaring activity could be investigated. Furthermore, magnetic activity was inferred from magnetogram data, for both flaring and non-flaring active regions.

5.2 Summary of results

5.2.1 Chapter 2

As previously discussed, the purpose of Chapters 2 and 3 was the study of analytical models for coronal loop oscillations. In particular, Chapter 2 introduced a model in Cartesian geometry. By assuming a magnetohydrostatic equilibrium, projection along the magnetic field lines leads to the derivation of the background pressure and density, that vary with the height above the solar surface. The magnetic field lines are then assumed to form magnetic surfaces which are invariant perpendicular to the field lines. Hence, a background magnetic field profile may be derived in both the x and z directions. Using the linearised ideal MHD equations, perturbations could be deconstructed into fast modes (normal to the magnetic surface) and Alfvén modes (perpendicular to the magnetic field lines).

By using the fact that the magnetic surfaces were constant, the Alfvén perturbations could be reduced to one spatial variable, thus described by an ordinary differential equation. Depending on the ratio between magnetic and

pressure scale heights, the solutions could be obtained analytically or numerically. When the pressure scale height became dominant over the magnetic scale height, we obtained cosine solutions for each wavenumber, symmetrical from footpoint to footpoint, where line-tying conditions forced the perturbations to be zero. However, as the magnetic scale height became more comparable with the pressure scale heights, we saw that amplitudes of perturbations became dampened away from the loop apex. Next, assuming a Gaussian excitation at $x = 0$, we could determine which wavenumbers existed. When the ratio of the magnetic and pressure scale heights was increased from 0, the power becomes more suppressed for larger frequencies, though peak power occurs in all atmospheres for infinitesimally small frequencies.

Next, we turned to the perturbations normal to the magnetic surface, known as the fast mode. Solving the governing equation separably in x and z lead to a purely sinusoidal contribution in the x direction, following a cosine or sine depending on the wavenumber. In the z direction, the solution was also purely sinusoidal in the case where the magnetic and pressure scale heights were the same. However, the perturbations otherwise possessed velocities damping as z increased with height when the ratio was less than 2, i.e when the gas pressure scale height was larger than the magnetic pressure scale height, and velocities diverging for large values of z when the ratio was greater than 2, i.e when the gas pressure scale height was smaller than the magnetic pressure scale height. Here, we introduced a region of density variation close to the footpoints of the magnetic arcade, reasoned by the finitely varying densities observed in the solar corona. Assuming a sharp density contrast, we showed that eigenfrequencies could be significantly altered, and that this could lead to some difficulties in the determination of modes in an observational context. Finally, we presented a case for excitation of fast modes. However, due to the complex nature in finding orthogonal functions numerically, this was only presented for the case where the magnetic and pressure scale heights were directly comparable ($\delta = 2$). By applying a Gaussian perturbation at the loop apex once more, we found very similar power spectrum to the Alfvén mode, suggesting that the Alfvén and fast modes contributed to the perpendicular and normal perturbations (respectively) contributed to the perturbations in the arcade for a similar frequency distribution.

5.2.2 Chapter 3

A coronal loop arcade in cylindrical geometry was introduced in Chapter 3. The necessity for a 3D waveguide was highlighted, with particular emphasis on recent observational evidence for loop interaction and multiple loop oscillations following flaring events (Jain, Maurya and Hindman (2015)). Additionally, a density interface was proposed such that the loops would lie in a shallow region of higher density, atop a rare cavity, with a sharp contrast between the two regions.

By assuming a force-free magnetic field in cylindrical coordinates, the arcade was modelled in semi-circular geometry, with field lines intersecting the photosphere at the footpoints of each field line. Assuming the loops lie in a cold plasma, and utilising the linearised ideal MHD equation once again, a velocity perturbation is introduced, varying only in the radial and axial directions. Hence, governing partial differential equations for both the radial and axial velocities were found. The azimuthal component of the temporal variation in the perturbed magnetic field could then be exploited to find the eigenmode solutions, reducing the radial and axial components to an ODE in terms of r.

At this point, a linear and discontinuous Alfvén speed profile was chosen, since this ensured the trapping of modes radially, such that there was a sudden jump in density at some defined radius, r_0. The choice of such Alfvén speeds reduced the governing equation for the eigenfunctions to a modified Bessel equation, with I or K modified Bessel function solutions on either side of the interface to ensure that waves were evanescent. Thus, a dispersion relation could be obtained by assuming continuity at the density interface, and propagation diagrams were obtained numerically for several different azimuthal modes. Choosing a location for the interface lead to the existence of both propagating and evanescent eigenfunctions satisfying the dispersion relation. For two such Alfvén speed profiles, and two different widths of the middle shell, the eigenfunctions, radial and axial velocities, and polarisation fraction were calculated. There, it was shown that all eigenfunctions became evanescent far away from the interface, and that there was elliptical polarisation for all modes, often switching smoothly between purely radial and purely axial motion, before becoming a mixture of the two for large radii. When the radius of the coronal loop arcade was increased, some modes became suppressed, indicating the sensitivity of choice in density distribution. Increasing the den-

sity contrast at the interface augmented the number of existing modes for all wavenumbers.

The Sun's corona shows discrete, bright loops above the limb. These preferred illuminated loops are believed to be more dense than their surroundings. In order to model a dense, finite width loop embedded in a rarer medium, we consider a three-shell model. In this sense, the coronal loops would be situated either at each of the interfaces (if there is a density increase at each interface) or in the middle of the two interfaces (if there is a density increase or decrease only for the middle shell). By updating the Alfvén speed profile to accommodate a middle shell of finite thickness, a third modified Bessel equation is used. Hence, by analytically solving and assuming continuity for eigenfunctions and radial velocities, the eigenfrequencies from a new dispersion relation are obtained. When the Alfvén speeds were assumed to be such that the density sharply increased at both interfaces, either a propagating or an evanescent mode was suppressed, when compared with the two-shell and three-shell models with differing density structures, though the present modes still exhibited elliptical motions. Increasing the thickness of the middle shell could also suppress modes, but not for all solutions of the governing equation. If we instead assumed that the middle shell was a dense region, surrounded on either side by a rare background, propagating modes were entirely suppressed for most interface locations, and instead another evanescent mode was produced. However, when the thickness of this shell was increased, the number of modes increased, and a propagating mode now existed, accompanied by two evanescent modes. Finally, by taking the limit of the middle shell thickness tending to infinity, it was shown that the two-shell model could be re-derived.

5.2.3 Chapter 4

Directing ourselves away from mathematical modelling, Chapter 3 delved into observational data analysis. We started by giving a brief background to solar flares, and their connection to coronal loop oscillations. The technique of Ring Diagram Analysis was described in depth, as well as details about the GONG network and the data used. Possible sources of error were highlighted — that is, that data maybe not be sampled too close to the limb of the Sun, and spatial and temporal samples may not be taken too large or too small (so that they may be untampered by noise or averaging). Similarly, when removing background flow to reveal the flows due to magnetic activity, we discussed the need to sample data from a similar epoch.

Data from seven flaring active regions in Solar Cycle 24 was sampled using Ring Diagram Analysis, each across seven calendar days (so for seven time series length 1440 mins), such that a flare occurred on the fourth day of each data set. Our analysis focussed on those active regions which produced X-class flares, as these are the most energetic. For each of the active regions, we obtained the total zonal and meridional flows. In most cases, the subsurface flows are irreversibly changed following large-scale flaring, and flow appear to become less sheared on the date the flare occurred. However, since the flaring process may have started at a different time in each series, significant changes to flows may have occurred the day before or the day after. Hence, the next step was to centre the time series on the exact time of the flare of interest.

To examine the effect of time series length and test our method of centring the time series on the flare, we studied two active regions in detail. For comparison, we sampled flows for time series of lengths 1664 minutes (the time taken for the patches sample to move one patch width), 832 minutes (the taken taken for half a patch width), and 1200 mins (which roughly bisects the first two time series lengths). We also sampled a time series on either side of the central time series, so that we could examine changes to flows preceding and following the flare. Once again, we examine the total horizontal flows (i.e. those without background flow removed). It was clear that the choice of temporal length had a large effect on the nature of the flows, since there was the possibility of sampling more or less flaring behaviour on either side of the flare of interest. However, there may have been noise added to the flow estimates by the shortened time series of 832 minutes. In particular, the zonal velocities appeared to behave differently when comparing the shortest time series with the other two time series, whilst the meridional flow behaviour remained very similar. Spatial averaging effects were also indicated here, as the active regions were of vastly different scales. In this case, the smaller active region will have contributed less to the overall flow patterns within the same size patch. Hence, for the final analyses, we chose to sample the smaller active region in patch more suitably sized.

Armoured with the knowledge gained throughout our journey into Ring Diagram Analysis, we carefully selected twelve active regions from Solar Cycle 24 (ten flaring and two non-flaring, for comparison). In addition to information pertaining to the size, date and time of the flare, we collected information about the number of sunspots, whether the active regions produced CMEs and their hemispheric location. Following the in-depth analysis of the Section 4.4.2

regarding time series length, we sampled across 1664 minutes. However, two active regions in this data set were small in comparison to others, so were sampled with a smaller patch size. In this analysis, background flows were also taken from a period when the Sun was relatively quiet (2008), and removed from each active region, to reveal the flows due to magnetic activity. However, comparison of active regions did not show any distinct properties of flaring regions beyond change in signature to flows, though magnitudes of flows were higher than those which did not flare. Some regions' shear became less pronounced during flaring, but this was not the case for all regions. Considering the properties of active regions, we saw that the magnetic activity index (MAI) did not show any clear links with flaring activity, though there was increased MAI compared to non-flaring regions. Similarly, it was not clear whether the presence of CMEs influenced the flows, or whether rotation of sunspots indicated an increased in flow twist. However, when comparing the size of the active region with average sunspot area, we found that those which had larger average sunspot area showed significantly more twisting than those with smaller area. Intuitively, this corresponded to more twisting needed to rearrange magnetic field lines.

5.3 Future work

Chapters 2 and 3 of this Thesis presented two different approaches to modelling coronal loop arcades, both in Cartesian and cylindrical geometries. However, both the models assumed the plasma to be zero-β, since magnetic forces were assumed to dominate in the solar corona. However, to adapt both the models to a more generic condition of the corona, we could assume the plasma to be low-β, so that the pressure gradient terms are included.

In Chapter 2, the density is assumed to vary vertically, with no adjustment accounting for the possibility that the density in the loops is not more than their surroundings. Hence, another way to make the model more realistic is to adapt a density profile which allows for the density to reflect the properties of the coronal loop more accurately.

The magnetic field profile chosen in Chapter 3 tends to infinity as $r \to 0$. Whilst this does not present itself an issue in analysis, since we are investigating the eigenfunctions away from the singularity, it does not make physical sense for there to be a point of magnetic field which is infinitely valued. Hence, further analysis could include the introduction of a magnetic field which does

not have a singular point. However, choice of magnetic field should be made with care, as this could affect the stability of the equilibrium atmosphere.

The analysis of active regions using Ring Diagram Analysis (RDA) was conducted using GONG data, obtained from a ground-based network. The advantage of using GONG for the data sets was that it is already readily calibrated for use with the RDA technique. However, since the network is ground-based, reliable data is dependent on the weather at the time of observation. RDA may be used with higher resolution satellite data such as that obtained from the Solar Dynamics Observatory's Helioseismic and Magnetic Imager (HMI), however this requires extensive manipulation before it can be used within the ring pipeline. Hence, the study could be repeated using HMI data. In a similar vein, with the advent of the DKIST telescope in the near future, ground-based data at a much higher quality than that obtained by GONG will be available and ready to use with the RDA technique.

APPENDIX A

Governing equation for u_r

We rearrange (3.13) in order to eliminate u_y:

$$u_y = \frac{-ikv_A^2 r u_r + ikv_A^2 r^2 \frac{\mathrm{d}u_r}{\mathrm{d}r}}{m^2 v_A^2 + k^2 v_A^2 r^2 - \omega^2 r^2}. \tag{A.1}$$

Differentiating (A.1) with respect to r yields

$$(m^2 v_A^2 + k^2 v_A^2 r^2 - \omega^2 r^2)^2 \frac{\mathrm{d}u_y}{\mathrm{d}r} = -ikm^2 v_A^4 u_r + 2ik^3 v_A^4 r^2 u_r - ik\omega^2 v_A^2 r^2 u_r \tag{A.2}$$

$$+ ikm^2 v_A^4 r \frac{\mathrm{d}u_r}{\mathrm{d}r} - ik^3 v_A^4 r^3 \frac{\mathrm{d}u_r}{\mathrm{d}r} \tag{A.3}$$

$$+ ik\omega^2 v_A^2 r^3 \frac{\mathrm{d}u_r}{\mathrm{d}r} + 2ik\omega^2 v_A r^3 \frac{\mathrm{d}u_r}{\mathrm{d}r} \tag{A.4}$$

$$- 2ik\omega^2 v_A r^4 \frac{\mathrm{d}v_A}{\mathrm{d}r} \frac{\mathrm{d}u_r}{\mathrm{d}r} + ikm^2 v_A^2 r^2 \frac{\mathrm{d}^2 u_r}{\mathrm{d}r^2} \tag{A.5}$$

$$+ ik^3 v_A^4 r^4 \frac{\mathrm{d}^2 u_r}{\mathrm{d}r^2} - ik\omega^3 v_A^2 r^4 \frac{\mathrm{d}^2 u_r}{\mathrm{d}r^2}. \tag{A.6}$$

Replacing (A.6) within (3.12) gives

$$-\omega^2 u_r (m^4 v_A^4 + k^4 v_A^4 r^4 + \omega^4 r^4 + 2k^2 m^2 v_A^4 r^4 - 2m^2 \omega^2 v_A^2 r^2 - 2k^2 \omega^2 v_A^2 r^4) \tag{A.7}$$

$$= (m^4 v_A^4 + k^4 v_A^4 r^4 + \omega^4 r^4 + 2k^2 m^2 v_A^4 r^4 - 2m^2 \omega^2 v_A^2 r^2 \tag{A.8}$$

$$- 2k^2 \omega^2 v_A^2 r^4) \cdot \left(\frac{(1-m^2) v_A^2}{r^2} u_r - \frac{v_A^2}{r} \frac{\mathrm{d}u_r}{\mathrm{d}r} + v_A^2 \frac{\mathrm{d}^2 u_r}{\mathrm{d}r^2} \right) \tag{A.9}$$

$$+ ikv_A^2 \cdot \Bigg(- ikm^2 v_A^4 u_r + 2ik^3 v_A^4 r^2 u_r - ik\omega^2 v_A^2 r^2 u_r + ikm^2 v_A^4 r \frac{\mathrm{d}u_r}{\mathrm{d}r} \tag{A.10}$$

$$- ik^3 v_A^4 r^3 \frac{\mathrm{d}u_r}{\mathrm{d}r} + ik\omega^2 v_A^2 r^3 \frac{\mathrm{d}u_r}{\mathrm{d}r} + 2ik\omega^2 v_A r^3 \frac{\mathrm{d}u_r}{\mathrm{d}r} - 2ik\omega^2 v_A r^4 \frac{\mathrm{d}v_A}{\mathrm{d}r} \frac{\mathrm{d}u_r}{\mathrm{d}r} \tag{A.11}$$

$$+ ikm^2 v_A^2 r^2 \frac{\mathrm{d}^2 u_r}{\mathrm{d}r^2} + ik^3 v_A^4 r^4 \frac{\mathrm{d}^2 u_r}{\mathrm{d}r^2} - ik\omega^3 v_A^2 r^4 \frac{\mathrm{d}^2 u_r}{\mathrm{d}r^2} \Bigg), \tag{A.12}$$

which can be expanded out to yield

$$-3m^4\omega^2 v_A^4 u_r - k^4\omega^2 v_A^4 r^4 u_r - \omega^6 r^4 u_r + 3m^2\omega^4 v_A^2 r^2 u_r + 2k^2\omega^4 v_A^2 r^4 u_r \quad \text{(A.13)}$$

$$=(1-m^2)\frac{m^4 v_A^6}{r^2}u_r - (1+m^2)k^4 v_A^6 r^2 u_r + \omega^4 v_A^2 r^2 u_r + 3k^2 m^2 v_A^6 u_r \quad \text{(A.14)}$$

$$- 2k^2 m^4 v_A^6 u_r - 2m^2\omega^2 v_A^4 u_r + 2k^2 m^2\omega^2 v_A^4 r^2 u_r - \frac{m^4 v_A^6}{r}\frac{\mathrm{d}u_r}{\mathrm{d}r} \quad \text{(A.15)}$$

$$- \omega^4 v_A^2 r^3\frac{\mathrm{d}u_r}{\mathrm{d}r} - 3k^2 m^2 v_A^6 r\frac{\mathrm{d}u_r}{\mathrm{d}r} + 2m^2\omega^2 v_A^4 r\frac{\mathrm{d}u_r}{\mathrm{d}r} + k^2\omega^2 v_A^4 r^3\frac{\mathrm{d}u_r}{\mathrm{d}r} \quad \text{(A.16)}$$

$$+ m^4 v_A^6\frac{\mathrm{d}^2 u_r}{\mathrm{d}r^2} + \omega^4 r^4 v_A^2\frac{\mathrm{d}^2 u_r}{\mathrm{d}r^2} + k^2 m^2 v_A^6 r^2\frac{\mathrm{d}^2 u_r}{\mathrm{d}r^2} - 2m^2\omega^2 v_A^4 r^2\frac{\mathrm{d}^2 u_r}{\mathrm{d}r^2} \quad \text{(A.17)}$$

$$- k^2\omega^2 v_A^4 r^4\frac{\mathrm{d}^2 u_r}{\mathrm{d}r} + k^2\omega^2 v_A^4 r^2 u_r - 2k^2\omega^2 v_A^3 r^3\frac{\mathrm{d}v_A}{\mathrm{d}r}u_r + 2k^2\omega^2 v_A^3 r^4\frac{\mathrm{d}v_A}{\mathrm{d}r}\frac{\mathrm{d}u_r}{\mathrm{d}r}. \quad \text{(A.18)}$$

Since (A.18) has so many terms, it is extremely difficult to solve analytically or even numerically. We, therefore, solve the governing equation for ϕ instead (see (3.27)).

APPENDIX B

An extension to the two and three-shell models

In Chapter 3, the extension of a two-shell model for a coronal loop arcade in cylindrical coordinates to that of a three-shell model indicated that a choice of model should be made with care. However, there is no reason to limit the choice of shells to just that of two or three. We here demonstrate the method of extending the model to the four, five and n-shell cases.

To invoke the four-shell model, assume that there is now an Alfvén speed profile such that

$$v_A(r) = \begin{cases} \dfrac{v_0}{r_0} r & r < r_0 \\ \dfrac{v_1}{r_0} r & r_0 \leq r < r_1 \\ \dfrac{v_2}{r_0} r & r_1 \leq r < r_2 \\ \dfrac{v_3}{r_0} r & r_2 \leq r, \end{cases} \tag{B.1}$$

where the density interfaces then reside at the radii $r = r_0$, r_1 and r_2.

Then, solution of the governing equation as in (3.39) yields

$$\phi = \begin{cases} A_0 I_{\nu_0} & r < r_0 \\ A_1 I_{\nu_1} + B_1 K_{\nu_1} & r_0 \leq r < r_1 \\ A_2 I_{\nu_2} + B_2 K_{\nu_2} & r_1 \leq r < r_2 \\ B_3 K_{\nu_3} & r_2 \leq r. \end{cases} \tag{B.2}$$

We once again assume continuity in ϕ and $\Omega^2 u_r$, and write these conditions in matrix form in Equation (B.3). The dispersion relation may then be obtained by setting the determinant of the coefficient matrix in (B.3) equal to zero. However, evaluation of the determinant is complex and involves many

$$
\begin{pmatrix}
I_{\nu_0}(kr_0) & -I_{\nu_1}(kr_0) & -K_{\nu_1}(kr_0) & 0 & 0 & 0 \\
\frac{I'_{\nu_0}(kr_0)}{\nu_0^2} & -\frac{I'_{\nu_1}(kr_0)}{\nu_1^2} & -\frac{K'_{\nu_1}(kr_0)}{\nu_1^2} & 0 & 0 & 0 \\
0 & I_{\nu_1}(kr_1) & K_{\nu_1}(kr_1) & -I_{\nu_2}(kr_1) & -K_{\nu_2}(kr_1) & 0 \\
0 & \frac{I'_{\nu_1}(kr_1)}{\nu_1^2} & \frac{K'_{\nu_1}(kr_1)}{\nu_1^2} & -\frac{I'_{\nu_2}(kr_1)}{\nu_2^2} & -\frac{K'_{\nu_2}(kr_1)}{\nu_2^2} & 0 \\
0 & 0 & 0 & I_{\nu_2}(kr_2) & K_{\nu_2}(kr_2) & -K_{\nu_3}(kr_2) \\
0 & 0 & 0 & \frac{I'_{\nu_2}(kr_2)}{\nu_2^2} & \frac{K'_{\nu_2}(kr_2)}{\nu_2^2} & -\frac{K'_{\nu_3}(kr_2)}{\nu_3^2}
\end{pmatrix}
\begin{pmatrix} A_0 \\ A_1 \\ B_1 \\ A_2 \\ B_2 \\ B_3 \end{pmatrix}
=
\begin{pmatrix} 0 \\ 0 \\ 0 \\ 0 \\ 0 \\ 0 \end{pmatrix}
\tag{B.3}
$$

terms, so we do not include the explicit dispersion relation in this appendix.

Similarly, the four-shell model may be extended to the five-shell model by assuming an Alfvén speed profile of the form

$$v_A(r) = \begin{cases} \frac{v_0}{r_0} r & r < r_0 \\ \frac{v_1}{r_0} r & r_0 \leq r < r_1 \\ \frac{v_2}{r_0} r & r_1 \leq r < r_2 \\ \frac{v_3}{r_0} r & r_2 \leq r < r_3 \\ \frac{v_4}{r_0} r & r_3 \leq r, \end{cases} \tag{B.4}$$

giving rise to eigenmode solutions of the form

$$\phi = \begin{cases} A_0 I_{\nu_0} & r < r_0 \\ A_1 I_{\nu_1} + B_1 K_{\nu_1} & r_0 \leq r < r_1 \\ A_2 I_{\nu_2} + B_2 K_{\nu_2} & r_1 \leq r < r_2 \\ A_3 I_{\nu_3} + B_3 K_{\nu_3} & r_2 \leq r < r_3 \\ B_4 K_{\nu_4} & r_3 \leq r. \end{cases} \tag{B.5}$$

The matrix form following continuity conditions may then be expressed as in Equation (B.8), where once again taking the the determinant of the coefficient matrix equal to zero yields the dispersion relation.

Finally, we may extend the model to any number of shells by assuming an Alfvén speed profile of the following form:

$$v_A(r) = \begin{cases} \frac{v_0}{r_0} r & r < r_0 \\ \frac{v_1}{r_0} r & r_0 \leq r < r_1 \\ \ldots & \\ \frac{v_{n-2}}{r_0} r & r_{n-3} \leq r < r_{n-2} \\ \frac{v_{n-1}}{r_0} r & r_{n-2} \leq r, \end{cases} \tag{B.6}$$

which corresponds to eigenmode solutions

$$\phi = \begin{cases} A_0 I_{\nu_0} & r < r_0 \\ A_1 I_{\nu_1} + B_1 K_{\nu_1} & r_0 \leq r < r_1 \\ ... & \\ A_3 I_{\nu_{n-2}} + B_3 K_{\nu_{n-2}} & r_{n-3} \leq r < r_{n-2} \\ B_4 K_{\nu_{n-1}} & r_{n-2} \leq r. \end{cases} \tag{B.7}$$

It then follows that the general form of the determinant which must be equated to zero to obtain the dispersion relation of an n-shell model is given by Equation (B.9). However, since we rely on the boundary conditions allowing the trapped modes to become evanescent over large radii, there is a limit to the physicality of the solutions or a large number of shells, unless they are assumed to be thin. Hence, the case for n-shells must be used with care, particularly alongside observational data.

$$
\begin{pmatrix}
I_{\nu_0}(kr_0) & -I_{\nu_1}(kr_0) & -K_{\nu_1}(kr_0) & 0 & 0 & 0 & 0 & 0 \\
\frac{I'_{\nu_0}(kr_0)}{\nu_0^2} & -\frac{I'_{\nu_1}(kr_0)}{\nu_1^2} & -\frac{K'_{\nu_1}(kr_0)}{\nu_1^2} & 0 & 0 & 0 & 0 & 0 \\
0 & I_{\nu_1}(kr_1) & K_{\nu_1}(kr_1) & -I_{\nu_2}(kr_1) & -K_{\nu_2}(kr_1) & 0 & 0 & 0 \\
0 & \frac{1}{\nu_1^2}I'_{\nu_1}(kr_1) & \frac{1}{\nu_1^2}K'_{\nu_1}(kr_1) & -\frac{1}{\nu_2^2}I'_{\nu_2}(kr_1) & -\frac{1}{\nu_2^2}K'_{\nu_2}(kr_1) & 0 & 0 & 0 \\
0 & 0 & 0 & I_{\nu_2}(kr_2) & K_{\nu_2}(kr_2) & -I_{\nu_3}(kr_2) & -K_{\nu_3}(kr_2) & 0 \\
0 & 0 & 0 & \frac{I'_{\nu_2}(kr_2)}{\nu_2^2} & \frac{K'_{\nu_2}(kr_2)}{\nu_2^2} & -\frac{I'_{\nu_3}(kr_2)}{\nu_3^2} & -\frac{K'_{\nu_3}(kr_2)}{\nu_3^2} & 0 \\
0 & 0 & 0 & 0 & 0 & I_{\nu_3}(kr_3) & K_{\nu_3}(kr_3) & -K_{\nu_4}(kr_3) \\
0 & 0 & 0 & 0 & 0 & \frac{I'_{\nu_3}(kr_3)}{\nu_3^2} & \frac{K'_{\nu_3}(kr_3)}{\nu_3^2} & -\frac{K'_{\nu_4}(kr_3)}{\nu_4^2}
\end{pmatrix}
\begin{pmatrix} A_0 \\ A_1 \\ B_1 \\ A_2 \\ B_2 \\ A_3 \\ B_3 \\ B_4 \end{pmatrix}
=
\begin{pmatrix} 0 \\ 0 \\ 0 \\ 0 \\ 0 \\ 0 \\ 0 \\ 0 \end{pmatrix}
\tag{B.8}
$$

$$
\begin{vmatrix}
I_{\nu_0}(kr_0) & -I_{\nu_1}(kr_0) & -K_{\nu_1}(kr_0) & 0 & 0 & ... & 0 & 0 & 0 & 0 & 0 \\
\frac{I'_{\nu_0}(kr_0)}{\nu_0^2} & -\frac{I'_{\nu_1}(kr_0)}{\nu_1^2} & -\frac{K'_{\nu_1}(kr_0)}{\nu_1^2} & 0 & 0 & ... & 0 & 0 & 0 & 0 & 0 \\
0 & I_{\nu_1}(kr_1) & K_{\nu_1}(kr_1) & -I_{\nu_2}(kr_1) & -K_{\nu_2}(kr_1) & ... & 0 & 0 & 0 & 0 & 0 \\
0 & \frac{1}{\nu_1^2}I'_{\nu_1}(kr_1) & \frac{1}{\nu_1^2}K'_{\nu_1}(kr_1) & -\frac{1}{\nu_2^2}I'_{\nu_2}(kr_1) & -\frac{1}{\nu_2^2}K'_{\nu_2}(kr_1) & ... & 0 & 0 & 0 & 0 & 0 \\
... & ... & ... & ... & ... & ... & ... & ... & ... & ... & ... \\
0 & 0 & 0 & 0 & 0 & ... & I_{\nu_{n-3}}(kr_{n-3}) & K_{\nu_{n-3}}(kr_{n-3}) & -I_{\nu_{n-2}}(kr_{n-3}) & -K_{\nu_{n-2}}(kr_{n-3}) & 0 \\
0 & 0 & 0 & 0 & 0 & ... & \frac{I'_{\nu_{n-3}}(kr_{n-3})}{\nu_{n-3}^2} & \frac{K'_{\nu_{n-3}}(kr_{n-3})}{\nu_{n-3}^2} & -\frac{I'_{\nu_{n-2}}(kr_{n-3})}{\nu_{n-2}^2} & -\frac{K'_{\nu_{n-2}}(kr_{n-3})}{\nu_{n-2}^2} & 0 \\
0 & 0 & 0 & 0 & 0 & ... & 0 & 0 & I_{\nu_{n-2}}(kr_{n-2}) & K_{\nu_{n-2}}(kr_{n-2}) & -K_{\nu_{n-1}}(kr_{n-2}) \\
0 & 0 & 0 & 0 & 0 & ... & 0 & 0 & \frac{I'_{\nu_{n-2}}(kr_{n-2})}{\nu_{n-2}^2} & \frac{K'_{\nu_{n-2}}(kr_{n-2})}{\nu_{n-2}^2} & -\frac{K'_{\nu_{n-1}}(kr_{n-2})}{\nu_n^2}
\end{vmatrix}
\tag{B.9}
$$

Bibliography

Alfvén, H. and Lindblad, B. (1947), 'Granulation, Magneto-Hydrodynamic Waves, and the Heating of the Solar Corona', *Monthly Notices of the Royal Astronomical Society* **107**(2), 211–219.

Antia, H. M. and Chitre, S. M. (1997), 'Helioseismic models and solar neutrino fluxes', *Monthly Notices of the Royal Astronomical Society* **289**(2), L1–L4.

Arregui, I. and Asensio Ramos, A. (2011), 'Bayesian magnetohydrodynamic seismology of coronal loops', *The Astrophysical Journal* **740**(1), 44.

Arregui, I., Terradas, J., Oliver, R. and Ballester, J. L. (2007), 'Damped oscillations of two interacting coronal loops', *Proceedings of the International Astronomical Union* **3**(S247), 133–139.

Aschwanden, M. J. (2005), *Physics of the Solar Corona: An Introduction with Problems and Solutions*, Praxis Publishing.

Aschwanden, M. J., Fletcher, L., Schrijver, C. J. and Alexander, D. (1999), 'Coronal Loop Oscillations Observed with the Transition Region and Coronal Explorer', *The Astrophysical Journal* **520**(2), 880–894.

Athay, R. G. and Moreton, G. E. (1961), 'Impulsive Phenomena of the Solar Atmosphere. I. Some Optical Events Associated with Flares Showing Explosive Phase', *The Astrophysical Journal* **133**, 935.

Baldner, C. S., Basu, S., Bogart, R. S., Burtseva, O., González Hernández, I., Haber, D., Hill, F., Howe, R., Jain, K., Komm, R. W., Rabello-Soares, M. C. and Tripathy, S. (2013), 'Latest Results Found with Ring-Diagram Analysis', *Solar Physics* **287**(1-2), 57–69.

Basu, S. (2016), 'Global seismology of the sun', *Living Reviews in Solar Physics* **13**(1), 1–126.

Birch, A., Gizon, L., Hindman, B. and Haber, D. (2007), 'The Linear Sensitivity of Helioseismic Ring Diagrams to Local Flows', *The Astrophysical Journal* **662**(1), 730–737.

Bogart, R. S., Baldner, C. S. and Basu, S. (2015), 'Evolution of near-surface flows inferred from high-resolution ring-diagram analysis', *The Astrophysical Journal* **807**(2), 125.

Cameron, A. G. (1962), 'The formation of the sun and planets', *Icarus* **1**(1-6), 13–69.

Campbell, W. R. and Roberts, B. (1989), 'The influence of a chromospheric magnetic field on the solar p- and f-modes', *The Astrophysical Journal* **338**, 538.

Christensen-Dalsgaard, J. (2002), 'Helioseismology', *Reviews of Modern Physics* **74**(4), 1073–1129.

Christensen-Dalsgaard, J., Dappen, W., Ajukov, S. V., Anderson, E. R., Antia, H. M., Basu, S., Baturin, V. A., Berthomieu, G., Chaboyer, B., Chitre, S. M., Cox, A. N., Demarque, P., Donatowicz, J., Dziembowski, W. A., Gabriel, M., Gough, D. O., Guenther, D. B., Guzik, J. A., Harvey, J. W., Hill, F., Houdek, G., Iglesias, C. A., Kosovichev, A. G., Leibacher, J. W., Morel, P., Proffitt, C. R., Provost, J., Reiter, J., Rhodes, E. J., Rogers, F. J., Roxburgh, I. W., Thompson, M. J. and Ulrich, R. K. (1996), 'The Current State of Solar Modeling', *Science* **272**(5266), 1286–1292.

Christensen-Dalsgaard, J., Gough, D. O. and Thompson, M. J. (1991), 'The depth of the solar convection zone', *The Astrophysical Journal* **378**(1), 413.

Cliver, E. W. (1995), 'Solar flare nomenclature', *Solar Physics* **157**(1-2), 285–293.

De Groof, A., Paes, K. and Goossens, M. (2002), 'Fast and Alfvén waves driven by azimuthal footpoint motions', *Astronomy and Astrophysics* **386**(2), 681–690.

De Moortel, I. (2005), 'An overview of coronal seismology', *Philosophical Transactions of the Royal Society A: Mathematical, Physical and Engineering Sciences* **363**(1837), 2743–2760.

Deubner, F.-L. (1975), 'Observations of low wavenumber nonradial eigenmodes of the Sun', *Astronomy and Astrophysics* **44**, 371–375.

Deubner, F.-L. and Gough, D. (1984), 'Helioseismology: Oscillations as a Diagnostic of the Solar Interior', *Annual Review of Astronomy and Astrophysics* **22**(1), 593–619.

Díaz, A. J., Zaqarashvili, T. and Roberts, B. (2006), 'Fast magnetohydrodynamic oscillations in a force-free line-tied coronal arcade', *Astronomy and Astrophysics* **455**(2), 709–717.

Dunster, T. M. (1990), 'Bessel Functions of Purely Imaginary Order, with an Application to Second-Order Linear Differential Equations Having a Large Parameter', *SIAM Journal on Mathematical Analysis* **21**(4), 995–1018.

Edwin, P. and Roberts, B. (1982), 'Wave propagation in a magnetically structured atmosphere', *Solar Physics* **76**(2).

Edwin, P. and Roberts, B. (1983), 'Wave propagation in a magnetic cylinder', *Solar Physics* **88**(1-2), 179–191.

Gizon, L. and Birch, A. C. (2004), 'Time-Distance Helioseismology: Noise Estimation', *The Astrophysical Journal* **614**(1), 472–489.

Gizon, L. and Birch, A. C. (2005), 'Local Helioseismology', *Living Reviews in Solar Physics* **2**.

Goldreich, P., Murray, N., Willette, G. and Kumar, P. (1991), 'Implications of solar p-mode frequency shifts', *The Astrophysical Journal* **370**, 752.

Goossens, M., Andries, J. and Aschwanden, M. J. (2002), 'Coronal loop oscillations', *Astronomy and Astrophysics* **394**(3), L39–L42.

Greer, B. J., Hindman, B. W., Featherstone, N. A. and Toomre, J. (2015), 'Helioseismic imaging of fast convective flows throughout the near-surface shear layer', *The Astrophysical Journal* **803**(2), L17.

Gruszecki, M., Murawski, K., Solanki, S. K. and Ofman, L. (2007), 'Attenuation of Alfvén waves in straight and curved coronal slabs', *Astronomy and Astrophysics* **469**(3), 1117–1121.

Haber, D. A., Hindman, B. W., Toomre, J., Bogart, R. S., Thompson, M. J. and Hill, F. (2000), 'Solar shear flows deduced from helioseismic dense-pack samplings of ring diagrams', *Solar Physics* **192**, 335–350.

Hernandez, I. G. (2008), 'Subsurface flows from ring diagram analysis', *Journal of Physics: Conference Series* **118**(1).

Heyvaerts, J. and Priest, E. R. (1983), 'Coronal heating by phase-mixed shear Alfven waves', *Astronomy and Astrophysics* **117**, 220–234.

Heyvaerts, J., Priest, E. R. and Rust, D. M. (1977), 'An emerging flux model for the solar flare phenomenon', *The Astrophysical Journal* **216**, 123.

Hill, F. (1988), 'Rings and trumpets - Three-dimensional power spectra of solar oscillations', *The Astrophysical Journal* **333**, 996.

Hindman, B. W. and Jain, R. (2014), 'An interpretation of flare-induced and decayless coronal-loop oscillations as interference patterns', *The Astrophysical Journal* **784**(2), 103.

Hindman, B. W. and Jain, R. (2015), 'Eigenmodes of Three-Dimensional Magnetic Arcades in the Sun'S Corona', *The Astrophysical Journal* **814**(2), 105.

Hindman, B. W. and Jain, R. (2018), 'A Novel Approach to Resonant Absorption of the Fast Magnetohydrodynamic Eigenmodes of a Coronal Arcade', *The Astrophysical Journal* **858**(1), 6.

Howe, R., Komm, R., Hill, F., Ulrich, R., Haber, D. A., Hindman, B. W., Schou, J. and Thompson, M. J. (2006), 'Large-Scale Zonal Flows Near the Solar Surface', *Solar Physics* **235**(1-2), 1–15.

Hoyle, F. (1946), 'The Synthesis of the Elements from Hydrogen', *Monthly Notices of the Royal Astronomical Society* **106**(5), 343–383.

Ionson, J. A. (1978), 'Resonant absorption of Alfvenic surface waves and the heating of solar coronal loops', *The Astrophysical Journal* **226**, 650.

Jain, K., Tripathy, S. C. and Hill, F. (2015), 'Divergent horizontal sub-surface flows within active region 11158', *The Astrophysical Journal* **808**(1), 60.

Jain, K., Tripathy, S. C. and Hill, F. (2017), 'Probing Subsurface Flows in NOAA Active Region 12192: Comparison with NOAA 10486', *The Astrophysical Journal* **849**(2), 94.

Jain, R. and Hindman, B. W. (2012), 'What can be learned from the seismology of a coronal loop using only a handful of frequencies?', *Astronomy and Astrophysics* **545**, A138.

Jain, R., Maurya, R. A. and Hindman, B. W. (2015), 'Fundamental-modes oscillations of two coronal loops within a solar magnetic arcade', *The Astrophysical Journal* **804**(1), L19.

Jain, R. and Roberts, B. (1993), 'Effects of non-parallel propagation on p- and f-modes', *Astronomy and Astrophysics* **286**, 243–253.

Jiang, Y., Zheng, R., Yang, J., Hong, J., Yi, B. and Yang, D. (2012), 'Rapid sunspot rotation associated with the X2.2 flare on 2011 February 15', *The Astrophysical Journal* **744**(1), 50.

Komm, R., González Hernández, I., Howe, R. and Hill, F. (2015), 'Solar-Cycle Variation of Subsurface Meridional Flow Derived with Ring-Diagram Analysis', *Solar Physics* **290**(11), 3113–3136.

Komm, R., Howe, R., González Hernández, I. and Hill, F. (2014), 'Solar-Cycle Variation of Subsurface Zonal Flow', *Solar Physics* **289**(9), 3435–3455.

Komm, R., Howe, R. and Hill, F. (2011), 'Subsurface Velocity of Emerging and Decaying Active Regions', *Solar Physics* **268**(2), 407–428.

Komm, R., Howe, R. and Hill, F. (2017), 'Solar-Cycle Variation of Subsurface-Flow Divergence: A Proxy of Magnetic Activity?', *Solar Physics* **292**(9), 122.

Komm, R., Howe, R., Hill, F., Gonzalez Hernandez, I. and Toner, C. (2005), 'Kinetic Helicity Density in Solar Subsurface Layers and Flare Activity of Active Regions', *The Astrophysical Journal* **630**(2), 1184–1193.

Leighton, R. B., Noyes, R. W. and Simon, G. W. (1962), 'Velocity Fields in the Solar Atmosphere. I. Preliminary Report.', *The Astrophysical Journal* **135**, 474.

Lekshmi, B., Nandy, D. and Antia, H. M. (2018), 'Asymmetry in Solar Torsional Oscillation and the Sunspot Cycle', *The Astrophysical Journal* **861**(2), 121.

Li, H., Liu, Y. and Tam, K. V. (2017), 'Fundamental and Harmonic Oscillations in Neighboring Coronal Loops', *The Astrophysical Journal* **842**(2), 99.

Melrose, D. B. (1980), *Plasma Astrophysics*, Gordon and Breach, Science Publishers.

Moffatt, H. K. and Tsinober, A. (1992), 'Helicity in Laminar and Turbulent Flow', *Annual Review of Fluid Mechanics* **24**(1), 281–312.

Montmerle, T., Augereau, J.-C., Chaussidon, M., Gounelle, M., Marty, B. and Morbidelli, A. (2006), '3. Solar System Formation and Early Evolution: the First 100 Million Years', *Earth, Moon, and Planets* **98**(1-4), 39–95.

Nakano, T. (1970), 'Origin of the Solar System', *Progress of Theoretical Physics* **44**(1), 77–98.

Nakariakov, V. M. (1999), 'TRACE Observation of Damped Coronal Loop Oscillations: Implications for Coronal Heating', *Science* **285**(5429), 862–864.

Nakariakov, V. M. and Ofman, L. (2001), 'Determination of the coronal magnetic field by coronal loop oscillations', *Astronomy and Astrophysics* **372**(3), L53–L56.

Nakariakov, V. M., Pilipenko, V., Heilig, B., Jelínek, P., Karlický, M., Klimushkin, D. Y., Kolotkov, D. Y., Lee, D. H., Nisticò, G., Van Doorsselaere, T., Verth, G. and Zimovets, I. V. (2016), 'Magnetohydrodynamic Oscillations in the Solar Corona and Earth's Magnetosphere: Towards Consolidated Understanding', *Space Science Reviews* **200**(1-4), 75–203.

Ofman, L., Parisi, M. and Srivastava, A. K. (2015), 'Three-dimensional MHD modeling of vertical kink oscillations in an active region plasma curtain', *Astronomy and Astrophysics* **582**, A75.

Oliver, R., Ballester, J. L., Hood, A. W. and Priest, E. R. (1993), 'Magnetohydrodynamic waves in a potential coronal arcade', *Astronomy and Astrophysics* **273**, 647–658.

Olver, F. W. J., Lozier, D. W., Boisvert, R. F. and Clark, C. W. (2010), *NIST Handbook of Mathematics Functions*, Cambridge University Press.

Pascoe, D. J., Goddard, C. R., Nisticò, G., Anfinogentov, S. and Nakariakov, V. M. (2016), 'Coronal loop seismology using damping of standing kink oscillations by mode coupling', *Astronomy and Astrophysics* **589**, A136.

Peterson, L. E. and Winckler, J. R. (1959), 'Gamma-ray burst from a solar flare', *Journal of Geophysical Research* **64**(7), 697–707.

Priest, E. (2013), *Magnetohydrodynamics of the Sun*, number May, Cambridge University Press, Cambridge.

Reinard, A. A., Henthorn, J., Komm, R. and Hill, F. (2010), 'Evidence that temporal changes in solar subsurface helicity precede active region flaring', *The Astrophysical Journal* **710**(2), L121–L125.

Roberts, B. (1981), 'Wave propagation in a magnetically structured atmosphere - II: Waves in a magnetic slab', *Solar Physics* **69**(1), 39–56.

Roberts, B., Edwin, P. M. and Benz, a. O. (1984), 'On coronal oscillations', *The Astrophysical Journal* **279**, 857.

Ruderman, M. S. and Roberts, B. (2002), 'The Damping of Coronal Loop Oscillations', *The Astrophysical Journal* **577**(1), 475–486.

Schou, J., Antia, H. M., Basu, S., Bogart, R. S., Bush, R. I., Chitre, S. M., Christensen-Dalsgaard, J., Di Mauro, M. P., Dziembowski, W. A., Eff-Darwich, A., Gough, D. O., Haber, D. A., Hoeksema, J. T., Howe, R., Korzennik, S. G., Kosovichev, A. G., Larsen, R. M., Pijpers, F. P., Scherrer, P. H., Sekii, T., Tarbell, T. D., Title, A. M., Thompson, M. J. and Toomre, J. (1998), 'Helioseismic Studies of Differential Rotation in the Solar Envelope by the Solar Oscillations Investigation Using the Michelson Doppler Imager', *The Astrophysical Journal* **505**(1), 390–417.

Tarr, L. A. (2017), 'On Excited Frequencies for Alfvén Waves in a Coronal Arcade', *The Astrophysical Journal* **847**(1), 1.

Terradas, J., Oliver, R. and Ballester, J. L. (2005), 'On the excitation of trapped and leaky modes in coronal slabs', *Astronomy and Astrophysics* **441**(1), 371–378.

Thompson, B. J., Plunkett, S. P., Gurman, J. B., Newmark, J. S., St Cyr, O. C. and Michels, D. J. (1998), 'SOHO/EIT observations of an Earth-directed coronal mass ejection on May 12, 1997', *Geophysical Research Letters* **25**(14), 2465–2468.

Thompson, M. J. (2004), 'Helioseismology and the Sun's interior', *Astronomy and Geophysics* **45**(4), 4.21–4.25.

Van Doorsselaere, T., Verwichte, E. and Terradas, J. (2009), 'The Effect of Loop Curvature on Coronal Loop Kink Oscillations', *Space Science Reviews* **149**(1-4), 299–324.

Verth, G. and Erdélyi, R. (2008), 'Effect of longitudinal magnetic and density inhomogeneity on transversal coronal loop oscillations', *Astronomy and Astrophysics* **486**(3), 1015–1022.

Verwichte, E., Foullon, C. and Nakariakov, V. M. (2006), 'Fast magnetoacoustic waves in curved coronal loops', *Astronomy and Astrophysics* **446**(3), 1139–1149.

Williams, J. P. (2010), 'The astrophysical environment of the solar birthplace', *Contemporary Physics* **51**(5), 381–396.

Zaatri, A., Komm, R., González Hernández, I., Howe, R. and Corbard, T. (2006), 'B_0-angle effect on zonal and meridional flow determinations from 3 years Ring Diagram Analysis of GONG++ data', *European Space Agency, (Special Publication) ESA SP* **624E**.